



UNIVERSIDADE ESTADUAL DE CAMPINAS
Faculdade de Engenharia Mecânica

WALTER ARIAS RAMIREZ

*Noise Generation in Airfoils with
Blunt Trailing Edges Including
Suction and Blowing Effects*

*Geração de Ruído em Aerofólios
com
Bordos de Fuga Espessos Incluindo
Efeitos de Sucção e Assopramento*

CAMPINAS
2016

Walter Arias Ramirez

*Noise Generation in Airfoils with
Blunt Trailing Edges Including
Suction and Blowing Effects*


*Geração de Ruído em Aerofólios
com
Bordos de Fuga Espessos Incluindo
Efeitos de Sucção e Assopramento*

Dissertation presented to the School of Mechanical Engineering of the University of Campinas in partial fulfillment of the requirements for the degree of Master in Mechanical Engineering, in the area of Thermal and Fluids.

Dissertação apresentada à Faculdade de Engenharia Mecânica da Universidade Estadual de Campinas como parte dos requisitos exigidos para a obtenção do título de Mestre em Engenharia Mecânica, na Área de Térmicas e Fluidos.

Adviser: Prof. Dr. William Roberto Wolf

ESTE EXEMPLAR CORRESPONDE À VERSÃO FINAL DA DISSERTAÇÃO DEFENDIDA PELO ALUNO WALTER ARIAS RAMIREZ, ORIENTADO PELO PROF. DR. WILLIAM ROBERTO WOLF.


.....
ASSINATURA DO ORIENTADOR.

CAMPINAS
2016

Agência(s) de fomento e nº(s) de processo(s): FAPESP, 2014/10166-6; CAPES

Ficha catalográfica
Universidade Estadual de Campinas
Biblioteca da Área de Engenharia e Arquitetura
Elizangela Aparecida dos Santos Souza - CRB 8/8098

Ar41n Arias Ramirez, Walter, 1989-
 Noise generation in airfoils with blunt trailing edges including suction and
 blowing effects / Walter Arias Ramírez. – Campinas, SP : [s.n.], 2016.

 Orientador: William Roberto Wolf.
 Dissertação (mestrado) – Universidade Estadual de Campinas, Faculdade
 de Engenharia Mecânica.

 1. Aerodinâmica. 2. Acústica. 3. Fluidodinamica computacional (CFD). 4.
 Mecânica de fluídos. 5. Escoamento instavel (Aerodinâmica). I. Wolf, William
 Roberto, 1980-. II. Universidade Estadual de Campinas. Faculdade de
 Engenharia Mecânica. III. Título.

Informações para Biblioteca Digital

Título em outro idioma: Geração de ruído em aerofólios com bordos de fuga espessos incluindo efeitos de sucção e assopramento

Palavras-chave em inglês:

Aerodynamics

Acoustics

Computational Fluid Dynamics (CFD)

Fluid Mechanics

Unstable flow

Área de concentração: Térmica e Fluídos

Titulação: Mestre em Engenharia Mecânica

Banca examinadora:

William Roberto Wolf [Orientador]

Carlos Eduardo Keutenedjian Mady

Sami Yamouni

Data de defesa: 25-01-2016

Programa de Pós-Graduação: Engenharia Mecânica

UNIVERSIDADE ESTADUAL DE CAMPINAS
FACULDADE DE ENGENHARIA MECÂNICA
COMISSÃO DE PÓS-GRADUAÇÃO EM ENGENHARIA
MECÂNICA
DEPARTAMENTO DE ENERGIA

DISSERTAÇÃO DE MESTRADO ACADÊMICO

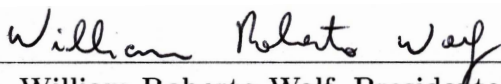
*Noise Generation in Airfoils with
Blunt Trailing Edges Including
Suction and Blowing Effects*

*Geração de Ruído em Aerofólios
com
Bordos de Fuga Espessos Incluindo
Efeitos de Sucção e Assopramento*

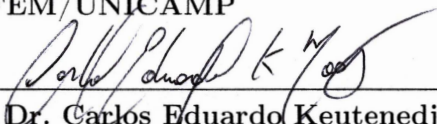
Autor: Walter Arias Ramirez

Orientador: Prof. Dr. William Roberto Wolf

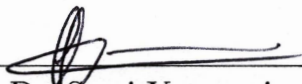
A Banca Examinadora composta pelos membros abaixo aprovou esta Dissertação:



Prof. Dr. William Roberto Wolf, Presidente
DE/FEM/UNICAMP



Prof. Dr. Carlos Eduardo Keutenedjian Mady
DE/FEM/UNICAMP



Prof. Dr. Sami Yamouni
ITA/DCTA

Campinas, January 25th of 2016.

In loving memory of my father
Alvaro de Jesús Arias Pacheco

Acknowledgements

First, I would like to thank the financial support received from Fundação de Amparo à Pesquisa do Estado de São Paulo, FAPESP, under grants No. 2014/10166-6, No. 2014/24043-3 and No. 2013/03413-4, and the financial support received from Conselho Nacional de Desenvolvimento Científico e Tecnológico, CNPq, under Grant No. 470695/2013-7 and Coordenação de Aperfeiçoamento de Pessoal de Nível Superior, CAPES, for providing me a MSc. scholarship during my first year. I also thank to Centro Nacional de Processamento de Alto Desempenho em São Paulo, CENAPAD-SP, for providing the computer resources for the numerical simulations under project 551.

I will always be grateful to my advisor, William Roberto Wolf, for his time and dedication to science. Always willing to take of his time to discuss new ideas and support me during this time in Brazil, William has been a truly guide and mentor. He gave me back the passion for science and research again. I was fortunate enough to had him as my advisor and friend.

I thank the members of my thesis committe, Prof. Dr. Carlos Eduardo Keutenedjian Mady and Dr. Sami Yamouni for their time and insight regarding this work.

I am also grateful to Eliana Alejandra Mejía for her constant support despite of the distance. Thanks to her inconditionality and indispensable help during my time in Equador and Medellín, I decided to take the risk to come here to Brazil. Her company during my first year was essential to me and gave me the strenght to continue.

I would like to give an special thank to Jaime Penadillo and Sergio Quispe for his value support during my first semester, I am indebted to them for their friendship and kindness. Also, despite of the short time we shared, I thank to Lucas Cóser for his comprehension and help during that time, only the people who had lived abroad can understand its hardships.

I am grateful with my colleagues and friends from CFD lab, Luiz Schiavo, Renato Miotto, Bruno Backes, Tulio Ricciardi, Cristiano Pimenta, Jean Marques, Paulo Azevedo (Rajesh), always willing to offer me a helping hand in difficult times. Along with them, we did the lab a familiar place, where we even worked. I also thank the colleagues I made here at Unicamp, Fabio Santiago, Max Reis, Karina Anaya, Renato Picelli, Jhon Jairo Perez, Mohammad Shaterzadeh, Rene Quispe, Kevin Nakabashi, Richard Huaman, and Tainan Khalil. I also thank to Edguitar, Carlos (el ebanista), Juan (countless nicknames), Jhon (pams), Harold (tony), Felipe (pitla) and Andres (smurfi).

I would like to thank my mentor during my intership at LLNL, Dr. Britton Olson for his patience and invaluable support. I am also grateful with Maria and David Dawson, for welcoming me at their home during my time in California, Livermore was so much better with their company. I also thank the colleagues and friend I made there, specially to Brian Weston, Daisy Ray, and Justin White.

I thank to family, my brother Alvaro José Arias Ramirez, my sister Carolina Arias Ramirez, my nephew Camilo Matajira Arias, my aunts Edith Corina Arias and Magaly Arias for their love and support.

Every single day I will thank to my father Alvaro de Jesús Arias Pacheco. He was my role-model, always willing to teach me through his example, that despite of hardships of life, he encouraged me to study, providing me with the best academic resources his low income could afford. He taught me that the best way to overcome poverty was through hard work and education. Dad, I dedicate this thesis to you.

“Walter, ¿Cómo hace usted para meterse todo eso en la cabeza?”

–My Mom

Abstract

Arias Ramirez, Walter. Noise Generation in Airfoils with Blunt Trailing Edges Including Suction and Blowing Effects. Master's Dissertation, 2016. School of Mechanical Engineering, University of Campinas, Campinas.

A numerical investigation is performed to assess the effects of trailing edge bluntness and trailing edge suction & blowing on airfoil self-noise generation and propagation. A suite of direct numerical simulations (DNS) are carried out for a NACA 0012 airfoil at different free-stream Mach numbers ($M_\infty = 0.1$ to 0.3), angles of incidence ($\text{AoA} = 0$ and 3°), and Reynolds numbers based on the airfoil chord ($Re_c = 5000, 10000, 50000$ and 100000). Two-dimensional simulations are performed for a NACA 0012 airfoil profile with two modified blunt trailing edges. The effects of suction and blowing on airfoil self-noise generation are also examined for the flow configurations above. A hybrid methodology that employs DNS for near-field source computations and the Ffowcs Williams–Hawkings equation as an acoustic analogy formulation is applied to quantify the individual contributions of the dipole and quadrupole sources to the total noise. Results for the low Reynolds number flows studied show that the airfoil emits a single “narrow-band” tone, and that a thicker trailing edge produces higher noise levels than a thinner one due to an increase in the intensity and proximity of quadrupole sources to the airfoil surface. On the other hand, results for the moderate Reynolds number flows analyzed reveal that the airfoil emits multiple “narrow-band” tones superimposed on a broadband hump depending on the flow configuration. These results indicate the existence of an acoustic feedback loop as discussed in literature. It is shown that the presence of the secondary tones is very dependent on compressibility effects, angle of incidence and trailing edge bluntness. For those cases where a broadband hump with multiple tones are observed, trailing edge blowing and suction considerably modifies the near-field hydrodynamic region responsible for noise generation and, for some of the flow configurations investigated, blowing can completely eliminate the tonal peaks. This work also shows in appendix A further details of novel numerical techniques which can be applied for the study of airfoil noise. This chapter is an outcome of a 6-month internship performed at Lawrence Livermore National Laboratory by the present author.

Keywords: airfoil noise, trailing edge bluntness, trailing edge suction and blowing, acoustic scattering, tonal noise, acoustic feedback loop.

Resumo

Arias Ramirez, Walter. Geração de Ruído em Aerofólios com Bordos de Fuga Espessos Incluindo Efeitos de Sucção e Assopramento. Dissertação de Mestrado, 2016. Faculdade de Engenharia Mecânica, Universidade Estadual de Campinas, Campinas.

Um estudo numérico é realizado para se avaliar os efeitos de espessura, sucção e assopramento em bordos de fuga nos processos de geração e propagação de ruído de aerofólios. Simulações numéricas diretas, *DNS*, (do inglês *Direct Numerical Simulations*) são realizadas para um aerofólio NACA 0012 em diversas condições de escoamentos com números de Mach ($M_\infty = 0.1$ até 0.3), ângulos de incidência ($AoA = 0$ e 3 deg.), e números de Reynolds baseados na corda do aerofólio ($Re_c = 5000, 10000, 50000$ e 100000). Simulações bi-dimensionais são realizadas para um perfil NACA 0012 com modificações nos bordos de fuga espessos. Os efeitos de sucção e assopramento são avaliados no processo de geração de ruído para as condições de escoamento acima. Uma metodologia híbrida que emprega DNS para o cálculo das fontes acústicas e a formulação de analogia acústica de Ffowcs Williams–Hawkings é utilizada para quantificar as contribuições das fontes sonoras do tipo dipolo e quadrupolo no ruído total. Resultados para escoamentos em baixos números de Reynolds mostram que o aerofólio emite um único componente tonal e que um bordo de fuga mais espesso produz um nível de ruído maior comparado com um bordo de fuga mais fino uma vez que os valores das fontes quadrupolo são maiores e se encontram mais próximas da superfície do aerofólio. No entanto, resultados para os escoamentos com números de Reynolds moderados revelam que o aerofólio pode emitir múltiplos tons sobrepostos num espectro de banda larga, dependendo da configuração do escoamento. Esses resultados indicam a existência de um mecanismo de retroalimentação acústico conforme discutido na literatura. A presença dos tons secundários é muito dependente dos efeitos de compressibilidade, ângulo de incidência e espessura de bordo de fuga. Para baixos números de Reynolds, assopramento no bordo de fuga reduz o nível de ruído gerado. Para os casos em que o ruído de banda larga com múltiplos tons são observados, sucção e assopramento modificam consideravelmente a região hidrodinâmica responsável pela geração de ruído e, para alguns dos casos analisados, o assopramento pode eliminar completamente os picos tonais. Este trabalho também apresenta no apêndice A um estudo sobre novas técnicas de simulação numérica que podem ser aplicadas no estudo de ruído de aerofólios. Esse estudo é resultado de um estágio de 6 meses no Lawrence Livermore National Laboratory realizado pelo autor.

Palavras-chave: ruído de aerofólio, espessura de bordo de fuga, sucção e assopramento em bordos de fuga, espalhamento acústico, ruído tonal, mecanismo de retroalimentação acústico.

List of Figures

1.1	Practical problems with trailing edge noise generation.	23
1.2	Sketch of flow past a NACA 0012 including its noise radiation.	28
1.3	Trailing edge profiles of the configurations analyzed.	28
1.4	Examples of suction and blowing along airfoil surface.	30
2.1	Mesh configuration for the studied cases.	36
2.2	Sketch with notation used in the Ffowcs Williams-Hawkings equation. . . .	41
3.1	Mean flow streamlines at trailing edge region for surface 1, AoA = 3 deg, and $Re_c = 5000$	45
3.2	Mean flow streamlines at trailing edge region for surface 1, $Re_c = 10000$ and $M_\infty = 0.3$	45
3.3	Snapshots showing contours of vorticity magnitude over the range over the range $ \omega = 0$ to 5, obtained for NACA 0012 with trailing edge surface 1. . .	46
3.4	Near-field pressure spectra obtained for surface 1 with (a) AoA = 3 deg, and (b) $Re_c = 10000$	47
3.5	Comparison of acoustic pressure contours at vortex shedding frequency over the range $ p' = \pm 5 \times 10^{-5}$ for surface 1 AoA = 3 deg, $Re_c = 10000$ and (a) $M_\infty = 0.1$, and (b) $M_\infty = 0.3$	48
3.6	Directivities of acoustic pressure, $ p' $, for an observer location at 5 chords from the airfoil. Results shown for the vortex shedding frequency.	48
3.7	Dipole and quadrupole source contributions to total noise for an observer location at 5 chords from the airfoil, at vortex shedding frequency for (a) AoA = 3 deg, $Re_c = 5000$ and $M_\infty = 0.3$ and (b) AoA = 3 deg, $Re_c = 10000$ and $M_\infty = 0.3$	50
3.8	Comparison of (a) pressure fluctuations, $ p' $, along airfoil surface and (b) far-field sound of incident quadrupolar field. Results are presented for sur- face 1 and $M_\infty = 0.3$ at vortex shedding frequency.	51
3.9	Mean flow streamlines along trailing edge region for AoA = 3 deg, $Re_c =$ 10000, and $M_\infty = 0.3$	51
3.10	Snapshots showing contours of vorticity magnitude over the range $ \omega = 0$ to 10, obtained for AoA = 3 deg, $Re_c = 10000$, and $M_\infty = 0.3$	52
3.11	Comparison of acoustic predictions for surfaces 1 (thinner TE) and 2 (thicker TE) for AoA = 3 deg, and $Re_c = 10000$	53
3.12	Comparison of acoustic pressure contours at vortex shedding frequency over the range $ p' = \pm 5 \times 10^{-4}$ for AoA = 3 deg, $Re_c = 10000$, $M_\infty = 0.3$ and (a) surface 1, and (b) surface 2.	53

3.13	Dipole and quadrupole source contributions to total noise at $5c$ distant from the airfoil, at vortex shedding frequency for $\text{AoA} = 3^\circ$, $Re_c = 10000$, $M_\infty = 0.3$ and (a) surface 1 and (b) surface 2.	54
3.14	Contours of magnitude of quadrupole sources for $\text{AoA} = 3^\circ$, $Re_c = 5000$, and $M_\infty = 0.2$. Contours go over the following ranges $\hat{T}_{11}=0$ to 0.005 , $\hat{T}_{12}=0$ to 0.004 and $\hat{T}_{22}=0$ to 0.0004	55
3.15	Comparison of (a) pressure fluctuations, $ p' $, along airfoil surface and (b) far-field sound of incident quadrupolar field. Results are presented for $\text{AoA} = 3^\circ$, $Re_c = 10000$, and $M_\infty = 0.3$, at vortex shedding frequency.	56
3.16	Comparison of the effects of suction and blowing on acoustic pressure spectrum for NACA 0012 at $\text{AoA} = 3^\circ$, $Re_c = 5000$ and $M_\infty = 0.3$	57
3.17	Comparison of blowing effects on mean flow streamlines at trailing edge region for $\text{AoA} = 3^\circ$, $Re_c = 5000$ and $M_\infty = 0.3$	58
3.18	Snapshots showing contours of vorticity magnitude over the range over the range $ \omega =0$ to 5 , obtained for NACA 0012 with trailing edge surface 2 for $\text{AoA} = 3^\circ$, $Re_c = 5000$ and $M_\infty = 0.3$	58
3.19	Comparison of acoustic pressure contours at vortex shedding frequency over the range $ p' = \pm 5 \times 10^{-5}$ for surface 2 $\text{AoA} = 3^\circ$, $Re_c = 5000$, $M_\infty = 0.3$ and (a) baseline configuration (no blowing), and (b) with blowing.	59
3.20	Dipole and quadrupole source contributions to total noise at $5c$ distant from the airfoil, at vortex shedding frequency for surface 2 $\text{AoA} = 3^\circ$, $Re_c = 5000$, $M_\infty = 0.3$ and (a) Baseline configuration (no blowing), and (b) with blowing 10%.	59
3.21	Magnitude of quadrupole sources over the range of $\hat{T}_{11}= 0$ to 0.016 , for surface 1 and $\text{AoA} = 3^\circ$, $Re_c = 5000$ and $M_\infty = 0.3$. Results shown for vortex shedding frequency.	60
3.22	Comparison of the effects of blowing on pressure fluctuations along airfoil and far-field sound for surface 1. Results are presented for $\text{AoA} = 3^\circ$, $Re_c = 5000$ and $M_\infty = 0.3$ at vortex shedding frequency.	60
3.23	Magnitude of quadrupole sources over the range of $\hat{T}_{11}= 0$ to 0.01 , for surface 2 and $\text{AoA} = 3^\circ$, $Re_c = 5000$ and $M_\infty = 0.3$. Results shown for vortex shedding frequency.	61
3.24	Comparison of the effects of blowing on pressure fluctuations along airfoil and far-field sound for surface 2. Results are presented for $\text{AoA} = 3^\circ$, $Re_c = 5000$ and $M_\infty = 0.3$ at vortex shedding frequency.	62
4.1	Mean flow streamlines at trailing edge region for surface 1, $\text{AoA} = 0^\circ$. and $Re_c = 50000$	64
4.2	Mean flow streamlines at trailing edge region for surface 1, $\text{AoA} = 0^\circ$. $Re_c = 100000$	64

4.3	Snapshots of flow streamlines (left) and iso-contours of instantaneous vorticity over the range $\omega = \pm 35$ (right) along the trailing edge for surface 1 AoA = 0 deg. $Re_c = 100000$ and $M_\infty = 0.3$.	65
4.4	Mean flow streamlines at trailing edge region for surface 1, AoA = 0 deg. $Re_c = 100000$ and $M_\infty = 0.2$.	66
4.5	Snapshots of flow streamlines at trailing edge region for surface 1 AoA = 0 deg, $Re_c = 100000$ and $M_\infty = 0.2$.	67
4.6	Iso-contours of instantaneous vorticity over the range $\omega = \pm 20$ at trailing edge region for surface 1 AoA = 0 deg, $Re_c = 100000$ and $M_\infty = 0.2$.	68
4.7	(a) Near-field pressure spectra, and (b) Directivity of acoustic pressure, $ p' $, for an observer location at 5 chords from the airfoil at vortex shedding, of surface 1 AoA = 0 deg, $Re_c = 50000$ and $M_\infty = 0.1 - 0.3$.	69
4.8	Near-field pressure spectra obtained for surface 1 with AoA = 0 deg. and $Re_c = 100000$.	70
4.9	Comparison of (a) pressure fluctuations $ p' $, along airfoil surface and (b) directivities of acoustic pressure, $ p' $, for an observer location at 5 chords from the airfoil, for surface 1 AoA = 0 deg. and $Re_c = 100000$.	71
4.10	Spatial distribution of the quadrupole sources over the range of $\hat{T}_{11} = 0$ to 0.01, at main peak frequency, for surface 1 AoA = 0 deg. and $Re_c = 100000$.	72
4.11	Snapshots of flow streamlines (left) and Iso-contours of instantaneous vorticity over the range $\omega = \pm 9$ (right) of surface 1 AoA = 3 deg, $Re_c = 50000$ and $M_\infty = 0.1$.	73
4.12	Snapshots of flow streamlines (left) and iso-contours of instantaneous vorticity over the range $\omega = \pm 12$ (right) of surface 1 AoA=3 deg. $Re_c = 100000$ and $M_\infty = 0.1$.	74
4.13	Near-field pressure spectra obtained for surface 1 AoA = 3 deg. and $Re_c = 50000$.	76
4.14	Near-field pressure spectra obtained for surface 1 AoA = 3 deg. and $Re_c = 100000$.	77
4.15	Effects of angle of attack on noise scattered for surface 1 AoA = 0 and AoA = 3 deg, $Re_c = 100000$, $M_\infty = 0.1$ (left) and $M_\infty = 0.3$ (right).	78
4.16	Mean flow streamlines along trailing edge for surface 1 (top) and surface 2 (bottom), and AoA = 0 deg, $Re_c = 50000$ (left), $Re_c = 100000$ (right), and $M_\infty = 0.3$.	79
4.17	Snapshots of flow streamlines (left) and iso-contours of vorticity (right) over the range $\omega = \pm 14$ along trailing edge for surface 2 AoA = 3 deg, $Re_c = 100000$ and $M_\infty = 0.1$.	80
4.18	Near-field pressure spectra for surface 2.	81

4.19	Comparison of blowing and suction effects on mean flow streamlines at trailing edge region for AoA = 0 deg, $Re_c = 100000$ and $M_\infty = 0.1$	82
4.20	Effects of suction and blowing on pressure spectra of surface 1 AoA = 0 deg. $Re_c = 100000$ and $M_\infty = 0.1$. Comparison of baseline case, with blowing 5% and suction 5% cases.	83
4.21	Acoustic pressure spectra of surface 1 AoA = 0 deg, $Re_c = 100000$ and $M_\infty = 0.3$, comparison of baseline case with suction and blowing 5% cases. (a) log×log scale, (b) linear×log scale.	84
4.22	(a) Suction & (b) blowing effects on acoustic pressure spectra of surface 1 AoA = 3 deg, $Re_c = 100000$ and $M_\infty = 0.3$	84
4.23	Blowing effects on pressure spectra of surface 2 for (a) AoA = 0 deg. and (b) AoA = 3 deg., and $Re_c = 100000$ and $M_\infty = 0.1$	85
4.24	Blowing effects on mean flow streamlines at trailing edge region for surface 2, AoA = 0 deg., $Re_c = 100000$ and $M_\infty = 0.3$	85
4.25	Spatial distribution of the quadrupole sources over the range of $\hat{T}_{11}=0$ to 0.05, at main peak frequency, for surface 2 AoA = 0 deg. $Re_c = 100000$ and $M_\infty = 0.3$ and (a) baseline case and (b) blowing 10% case.	86
5.1	Tonal peak amplitude behavior as a function of Helmholtz number $kc=2\pi fc$ for the suite of studied cases.	88
5.2	Cases where secondary tones are found. Filled triangle symbol ► means surface 1 with no secondary tones, empty triangle symbol ▷ means surface 1 with secondary tones, filled circle symbol ● means surface 2 with no secondary tones, empty circle symbol ○ means surface 2 with secondary tones. Large symbols represent cases with angle of attack 3 deg, and small symbols represent cases with angle of attack 0 deg.	89
A.1	Schematic of a cylinder immersed in a Cartesian grid.	99
A.2	“PiSTL” results.	101
A.3	(a) Transfer of forcing \mathbf{F} from Lagrangian boundary point to surrounding fluid nodes. (b) Distribution functions employed in various studies, (MITTAL AND IACCARINO, 2005).	103
A.4	Schematic of ghost cell method(SEO AND MITTAL, 2011).	105
A.5	(a) Schematic representation of the acoustic wave reflection. (b) pressure vs. time plot.	107
A.6	Acoustic wave reflection results for (a) continuous forcing approach with different thickness (b) discrete forcing approach IBM, for a pulse of PPW=16, $\lambda=0.04\text{cm}$	108
A.7	Relative error behavior for acoustic wave reflection results.	108
A.8	(a)Schematic representation of 1–D shock wave. (b) pressure vs. time plot.	109

A.9	Shock wave reflection results for Mach number $M_{shock} = 2.0$ using the continuous forcing approach. Each line represents a different case studied: the black and solid-line: hard wall without IBM, Red and dash-dot-line: hard wall with IBM-thickness of 1, blue and long-dash-line: hard wall with IBM-thickness of 3, green and dash-dot-dot-line: hard wall with IBM-thickness of 5.	110
A.10	Shock wave reflection results for Mach number $M_{shock} = 2.0$ using the discrete forcing approach. The black and solid-line represents the case of a hard wall without IBM and the red dash-dot-line represents the case with the discrete IBM.	110
A.11	Error behaviour in shock wave reflection results.	111
A.12	Schematic representation of acoustic scattering on a cylinder.	111
A.13	cases analysed.	112
A.14	Directivity plot comparison for continuous forcing approach. The black line represents the analytical results and the blue points represent the numerical results.	113
A.15	Error L2Norm contour plot of all cases studied.	114
A.16	Comparison of results between the continuous approach (using IBM-thickness = 1.0 and 2.0), the discrete approach and the analytical solution.	114
A.17	Transonic flow past different airfoil shapes.	115

List of Tables

1.1	Details of the configurations analyzed.	28
1.2	Features of studied baseline cases.	29
1.3	Features of cases studied using suction & blowing.	31
2.1	Characteristics of meshes employed in the simulations.	35
3.1	Studied cases for low Reynolds number flows.	44
3.2	Overall sound pressure level for low Reynolds number cases.	62
4.1	Studied cases for moderate Reynolds number flows.	63
4.2	Near-field spectra data for surface 1 AoA = 0 deg. and $Re_c = 50000$	70
4.3	Near-field spectra data for surface 1 AoA = 0 deg. and $Re_c = 100000$. . .	71
4.4	Near-field spectra data for surface 1 AoA = 3 deg. and $Re_c = 50000$	75
4.5	Near-field spectra data for surface 1 AoA = 3 deg. and $Re_c = 100000$. . .	75
4.6	Near-field spectra data for surface 2 AoA = 0 deg. and $Re_c = 50000$	82
4.7	Near-field spectra data for surface 2 AoA = 0 deg. and $Re_c = 100000$	82
4.8	Near-field spectra data for surface 2 AoA = 3 deg. and $Re_c = 50000$	83
4.9	Near-field spectra data for surface 2 AoA = 3 deg. and $Re_c = 100000$	83
4.10	Overall sound pressure level for moderate Reynolds number cases.	86

Nomenclature

c_∞	free-stream speed of sound
c	Airfoil chord
E	Total energy
f	FW-H surface
F_i	Dipole source
G	Green's function
g_{ij}	covariant metric tensors
g^{ij}	contravariant metric tensors
H	Heaviside function
$H_0^{(2)}$	Hankel function of the second kind and order zero
i	Imaginary unit
M_∞	free-stream Mach number
q_j	Heat flux
p	Pressure
Pr	Prandtl number
Q	Monopole source
Re_c	Reynolds number based on airfoil chord c
t	Time
T	Temperature
T_{ij}	Quadrupole source (Lighthill stress tensor)
u_i	Fluid velocity
u^i	Contravariant velocity components
U_i	Mean flow velocity
\vec{x}	Observer position
\vec{y}	Source position
γ	Ratio of specific heats
δ_{ij}	Kronecker delta
ρ	Density
τ_{ij}	Viscous stress tensor
ω	Angular frequency
κ	Thermal conductivity
μ	Dynamic viscosity coefficient
ν	Kinematic viscosity coefficient

Subscripts

- 0 Mean value
- ∞ Free-stream quantity

Superscripts

- ' Perturbation value
- $\hat{}$ Fourier transformed quantity

Contents

List of Figures	x
List of Tables	xv
Nomenclature	xviii
Contents	xvii
1 INTRODUCTION	21
1.1 Motivation	21
1.1.1 Aeronautical Industry	21
1.1.2 Wind Power Generation	22
1.1.3 Other Applications	23
1.2 Objectives	24
1.3 Literature Review	24
1.3.1 Airfoil Self-Noise and Acoustic Feedback Loop	24
1.3.2 Summary	26
1.4 Overview and Summary of Contributions	27
1.5 Outline of the Current study	31
2 THEORETICAL AND NUMERICAL FORMULATION	33
2.1 Introduction	33
2.2 Flow Simulations	33
2.3 Spatial Discretization	36
2.4 Time Integration	37
2.5 Boundary Conditions	38
2.6 Acoustic Analogy Formulation and Noise Predictions	40
2.7 Summary	43
3 AIRFOIL NOISE PREDICTIONS AT LOW REYNOLDS NUMBERS	44
3.1 Introduction	44
3.2 Effects of Compressibility on Noise Generation	44
3.3 Effects of Trailing Edge Bluntness on Noise Generation	50
3.4 Effects of Trailing Edge Suction & Blowing on Noise Generation	55

4	AIRFOIL NOISE PREDICTIONS AT MODERATE REYNOLDS NUMBERS	63
4.1	Introduction	63
4.2	Effects of Compressibility on Noise Generation	63
4.3	Effects of Angle of Attack on Noise Generation	72
4.4	Effects of Trailing Edge Bluntness on Noise Generation	78
4.5	Effects of Suction & Blowing at Trailing Edge on Noise Generation	82
5	CONCLUSIONS	87
5.1	Summary	87
5.2	Future Work	90
	References	91
	APPENDIX	97
A	— COMPRESSIBLE FLOW SIMULATIONS OF WAVE SCATTERING PROBLEMS USING THE IMMERSSED BOUNDARY METHOD	97
A.1	Note of Clarification	97
A.2	Introduction	98
A.3	Theoretical Background	98
A.3.1	Point in STL - “PiSTL”	99
A.3.2	Immersed Boundary Method	100
Continuous Forcing Approach	102
Discrete Forcing Approach	104
A.3.3	The Miranda code	105
A.4	Methodology	106
A.5	Results	106
A.5.1	Plane-wave hitting a hard wall	107
A.5.2	Shock-wave hitting a hard wall (shock-tube)	109
A.5.3	Acoustic Scattering on a Cylinder	110
A.5.4	Transonic Flow	112

1 INTRODUCTION

1.1 Motivation

Aeroacoustics is a topic which combines fluid mechanics and acoustics, and that encompasses problems related to flow-induced sound. Although it may seem a very particular field, it has important applications in physics and engineering. The noise that arises from aerodynamic flows plays a main role in several engineering applications, being undesirable in most of these. The study of aeroacoustics finds applications in the design of aircraft and individual components, automobiles, high-speed trains, rockets, wind turbines and home utensils. Due to the non-linearity of the flow processes which govern noise generation, the investigation of problems of aeroacoustics may be difficult and the noise prediction can be cumbersome.

1.1.1 Aeronautical Industry

In the previous decades, researchers determined that airframe noise was of secondary importance in aeronautical problems since jet noise was a dominant source. However, since the 1970s and continuing to date, due to the introduction of turbofan engines with larger bypass ratios, the aircraft propulsive noise has been reduced. As a result, the sound generation by the interaction of the unsteady flows around the airframe has become of paramount importance, and marginally lower than the propulsion noise in conditions of approaching and landing when landing gears and high-lift devices are deployed. Indeed, in some modern airplanes, the engine noise is less intense than that generated by the airframe during approach (LELE AND NICHOLS, 2014). Thus, any further reduction of aircraft noise on those conditions can only be achieved when both engine and airframe noise are reduced.

Currently, the impact of aircraft noise is an issue of public interest due to the ongoing growth in air traffic and its subsequent need for new airports or the expansion of current ones (DOBRZYNSKI, 2010). In consequence, noise regulations have become incrementally more stringent, and this trend is expected to continue into the foreseeable future. As aviation continues to grow, its unwelcome noise impacts a larger community which drives even more stringent regulations. One of the aviation goals for future is to reduce the aircraft noise footprints outside the airport perimeter. Industry envisions the design of the silent aircraft whose noise levels outside the airport perimeter should not be louder

than the city ambient noise. For instance, NASA's long-term goal is to reduce aircraft noise in 20 dB and its short-term goal is to obtain a reduction of 10 dB. These goals are scientifically demanding since they correspond to reducing the acoustic power emission by 90 percent (LOCKARD AND LILLEY, 2004).

If the entire noise associated with the high-lift and landing gear systems were eliminated (*clean* airplane configuration), the total noise reduction during landing would be about 7 dB. Experimental and theoretical evidence suggests that the noise of a clean airplane arises from turbulent eddies which are convected past trailing edges of wings and control surfaces. In this case, hydrodynamic energy from the flow is transformed into acoustic energy which radiates as sound. This process occurs when boundary layers and wakes interact with solid surfaces in the airplane.

As the primary sources of airframe noise are eliminated, other noise sources will become the next limiting factor in noise reduction. The technologies that are currently being developed should provide substantial noise reduction for the high-lift system and landing gears. However, research still needs to be conducted to develop innovative methodologies for the reduction of other noise sources. The trailing edge scattering mechanism is a major source of airframe noise that may become dominant with projected reductions in the noise from the high-lift system (LOCKARD AND LILLEY, 2004). Therefore, understanding the physics of trailing edge noise generation and propagation is an important research topic in aeroacoustics.

1.1.2 Wind Power Generation

Flow-induced sound plays a main role in engineering applications such as turbomachinery. For instance, an important factor for wind turbine design is the level of noise that a turbine radiates. This issue is becoming increasingly important as more turbines are placed closer to population centers with even more restrictive noise restriction. Oerlemans and Mendez (2005), performed measurements on a full scale wind turbine with the aim to characterize the noise sources and to verify whether aerodynamic noise from the blades is dominant. Their results (see fig 1.1 (a)) show that virtually all noise radiated to the ground is produced during the downward movement of the blades. Moreover, it turned out that the noise is produced by the outer part of the blades and that the main noise source mechanism is the trailing edge rather than the inflow turbulence noise.



(a) Main sources of wind turbine noise.



(b) Cross bar section.

Figure 1.1: Practical problems with trailing edge noise generation.

1.1.3 Other Applications

In the automotive industry, drivers and passengers currently complain about the annoying noise that arises from the crossbar sections installed at roof rack in the top of their cars. These bars commonly have transverse airfoil sections with truncated trailing edges (see fig 1.1 (b)). Hence, the noise mechanism is associated with vortex shedding generated by the blunt trailing edge. Other examples of aeroacoustic noise are those from the cabin noise in automobiles associated with external flow past side mirrors, air-conditioning ventilation and vacuum cleaners. Flow-induced sound also plays an important role in biomechanics. Human speech and animal vocalization is enabled by the generation of flow-induced sound in the larynx.

In summary, due to the more stringent noise regulations and, since air traffic and wind power generation have increased, the understanding of the fundamental mechanisms of airframe noise generation, and their control, is an overriding concern for the design of low-noise aerodynamic configurations including wings and high-lift components, as well as wind turbine blades, propellers and fans. In this context, the study of trailing edge noise is a research topic of paramount importance.

1.2 Objectives

The objectives of this work are:

- to analyze the behavior of fundamental mechanisms of trailing edge noise such as “laminar boundary-layer–vortex-shedding (LBL-VS) noise”, “trailing edge bluntness–vortex-shedding (TEB-VS) noise”, and “boundary layer separation noise” for different flow conditions and trailing edge profiles.
- to investigate the effects of trailing edge bluntness on noise generation and propagation at low to moderate Reynolds numbers, for low to moderate Mach numbers.
- to assess the effects of suction and blowing on trailing edge noise reduction.
- to develop novel numerical techniques that allow the study of flows past complex geometries and that can be applied for the study of airfoil noise.

1.3 Literature Review

1.3.1 Airfoil Self-Noise and Acoustic Feedback Loop

Several pioneering studies of airfoil noise were conducted in the 1970s in order to examine airfoil tonal noise generation. These investigations showed that discrete tones are emitted from isolated airfoils or helicopter rotors at specific flow conditions (SMITH *et al.*; CLARK; HERSH AND HAYDEN; LONGHOUSE, 1970; 1971; 1971; 1977). These findings triggered some of the first systematic, detailed and well known studies of airframe noise (PATERSON *et al.*; TAM; FINK; FINK *et al.*; ARBEY AND BATAILLE, 1973; 1974; 1975; 1976; 1983). Paterson *et al.* (1973) performed noise measurements from symmetric NACA airfoils with a Reynolds number range between 10^5 and 10^6 with various angles of attack; their results showed the existence of discrete and multiple tones in a ladder-like structure pattern in terms of frequency and free-stream velocity. They also proposed an average evolution of the dominant frequency in function of free-stream velocity, U_∞ , as follows: $f=0.01U_\infty^{3/2}/(c\nu)^{1/2}$. In this equation, c is the airfoil chord and ν is the coefficient of kinematic viscosity. Furthermore, they measured span-wise surface pressure correlations on the airfoils and found strong correlations over a considerable extent along the airfoil surface. This indicated that the flow phenomenon associated with airfoil tonal noise generation can be considered as two dimensional.

Another theory for the power law observed by Paterson was proposed by Fink (1975). He assumed that the discrete frequencies were linked to the laminar boundary-layer of the airfoil pressure surface. Arbey and Bataille (1983) repeated the experimental studies from Paterson in an open wind tunnel for three different NACA airfoils and showed that the tonal peak was a superposition of broadband contribution centered on a main frequency f_s and a set of regularly spaced discrete frequency tones f_n . The dominant frequency, f_s , was in agreement with Paterson's formula showed above. These authors also found the ladder-like structure from Paterson's original work but other results were in disagreement, for example, the higher magnitudes of the discrete tones and the different tone distribution.

Tam (1974) suggested that the ladder-like structure of frequency as a function of flow velocity was due to a self-excited feedback loop between the trailing edge and the noise source in the near wake. Nash *et al.* (1999) performed experimental studies of airfoil tonal noise generation for a NACA 0012 profile with a Reynolds number of 1.45×10^6 and several angles of attack. A closed-working-section wind tunnel, with and without an acoustic-absorbing lining on its walls, was used in the experiments. The results from the hard-wall tunnel (without lining) revealed multiple frequency peaks, in agreement with the overall $U_\infty^{3/2}$ law for the dominant tones and with the local dependence $U_\infty^{0.8}$ for the secondary tones, as proposed by Paterson. However, the authors argued that these tonal frequency peaks were correlated to the resonant frequencies of the wind tunnel. Thus, they carried out measurements with lined walls simulating anechoic conditions. Under these conditions, it was found that a single dominant tonal frequency was observed with the power law $U_\infty^{0.8}$ instead of several peaks. Furthermore, no ladder-like structure of tonal frequency was observed, in disagreement with the previous studies of Paterson *et al.* (1973), Fink, (1975) and Arbey and Bataille (1983). Nash *et al.* (1999) argued that the previous researchers may have been misled by spurious feedback loops which had arisen from the facilities, even in open jet studies.

Brooks *et al.* (1989) identified vortex shedding due to laminar boundary layer instabilities and from blunt trailing edges as sources of airfoil self-noise. Wolf *et al.* (2012a; 2013; 2012b) performed numerical investigations of airfoil self-noise generation for turbulent flows past a NACA 0012 and a DU96 airfoil. They showed that tonal noise may appear in far-field acoustic predictions for blunt trailing edges even in the presence of fully turbulent boundary layers. The presence of tonal noise would then depend on both the trailing edge thickness and the boundary layer displacement thickness.

Desquesnes *et al.* (2007) performed 2D direct numerical simulations (DNS) for a flow past a NACA 0012 airfoil for Reynolds numbers 1×10^5 and 2×10^5 , and angles of attack of 2 and 5 degs; their results showed the multiple tonal peaks consistent with the experimen-

tal observations from Arbey and Bataille (1983). Kurotaki *et al.* (2008) and Plogmann *et al.* (2013) also found multiple tones in their experimental results and the so-called ladder-like structure pattern. Chong and Joseph (2009) carried out an experimental study of tonal noise mechanism on a NACA 0012 airfoil. However, they placed the airfoil inside the nozzle of an open wind tunnel and, hence, their data may have been influenced by the duct modes. Meanwhile, Tam and Ju (2011) conducted direct numerical simulations (DNS) on a NACA 0012 airfoil for three different trailing edge thicknesses in the Reynolds number range of 2×10^5 to 5×10^5 at zero angle of attack. Under these conditions, their numerical results showed only one airfoil tone for each simulation, in agreement with the measurements of Nash *et al.* (1999) and supporting the argument that the ladder-like structure pattern of isolated tones is not genuine. In addition, Tam and Ju (2011) suggested that an airfoil with a thicker trailing edge would have a lower tonal frequency for the same flow velocity. Hutcheson and Brooks (2004) carried out detailed experimental measurements of a cambered NACA 63-215 varying the angle of attack, velocity and trailing edge bluntness. They concluded that, for increased air speed, the trailing edge increases noise levels and shifts noise to higher frequencies. Moreover, it was found that, for increased bluntness, the spectral peak increases in level and shifts to lower frequencies, in agreement with Tam and Ju (2011). Concerning flow control, Corcoran (1992) and Naumann (1992) performed one of the first experimental studies using trailing edge blowing. They examined its effectiveness in decreasing the wake deficit caused by the fan blades, thereby reducing rotor wake-stator interaction noise. Later, more realistic studies like (BROOKFIELD AND WAITZ, 2000) and (ENGHARDT *et al.*, 2015) were performed using trailing edge blowing with the aim of reducing the noise generated in the rotor-stator interaction.

1.3.2 Summary

It is clear that since the 1970s, great efforts have been carried out to improve the understanding of the airfoil tonal noise phenomenon. However, there are still several issues and disagreements in literature. There is a lack of detailed and systematic studies regarding the effects of trailing edge bluntness on airfoil tonal noise generation. Most previous work regarding flow control relies on experiments or flow simulations which employ turbulent models. To the knowledge of the present author, this is the first study of blowing effects on airfoil self-noise generation which applies high-fidelity numerical simulations. A detailed study of trailing edge blowing effects on a compressible fully resolved flow is needed in order to understand the changes in the hydrodynamic and aeroacoustic quantities involved in airfoil self-noise generation.

Despite of the widely known advantages of DNS, it is well known that direct simulation of noise remains prohibitively expensive for engineering problems due to mesh resolution requirements. Therefore, hybrid approaches that consist of predicting near-field flow quantities by a suitable computational fluid dynamics (CFD) simulation and far-field sound radiation by an acoustic analogy formulation are more attractive. The flow physics associated with sound generation must be accurately captured in the CFD calculations in order to be used in this context. In the present work, the Ffowcs Williams and Hawkings (1969) acoustic analogy formulation (FWH) is applied together with the DNS results. In the FWH formulation, the acoustic pressure fluctuations are predicted by solving an inhomogeneous wave equation with surface monopole, dipole and volume quadrupole source terms. Quadrupole sources are often neglected in sound calculations for low Mach number flows, since monopole and dipole sound contributions are dominant. In the present work, an assessment of the effects of quadrupole sources is performed in order to evaluate its impact in far-field noise radiation.

1.4 Overview and Summary of Contributions

The present work examines in details the effects of trailing edge bluntness and trailing edge suction and blowing over airfoil self-noise generation and propagation processes. By means of a suite of direct numerical simulations (DNS) of a canonical case of a flow past a NACA 0012 airfoil (see fig. 1.2) with different flow parameters along with an acoustic prediction approach, we analyze the behavior of fundamental trailing edge sources like “laminar-boundary-layer-vortex-shedding (LBL-VS) noise”, “trailing edge bluntness-vortex-shedding (TEB-VS) noise”, and “boundary layer separation noise” for the different flow conditions. Compressible two-dimensional DNS are conducted for different rounded trailing edges of a NACA 0012 airfoil as shown in fig. 1.3 and Table 1.1. Flow configurations with different free-stream Mach numbers ($M_\infty = 0.1$ to 0.3), angles of incidence ($\text{AoA} = 0$ and 3 deg.), and Reynolds numbers based on the airfoil chord ($Re_c = 5000, 10000, 50000$ and 100000) are analyzed. The flow parameters for the cases studied without suction & blowing are summarized in table 1.2 and the cases studied using suction & blowing are summarized in table 1.3. In addition, a hybrid approach that uses direct calculation for near-field flow quantities and the Ffowcs Williams–Hawkings acoustic analogy to compute the far-field sound radiation is used. The acoustic prediction considers the effects of Mach number and non-linear quadrupole sources on sound propagation, and it allows the analysis of the radiation associated with the dipole and quadrupole sources separately.

Figure 1.4 shows a schematic representation where steady blowing and suction are

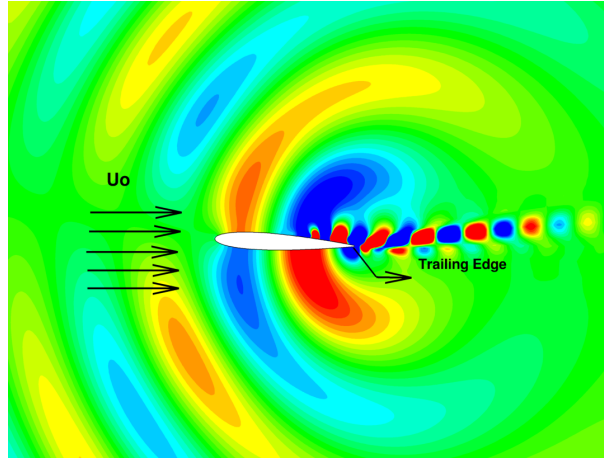


Figure 1.2: Sketch of flow past a NACA 0012 including its noise radiation.

applied along the airfoil surface. Different configurations of suction and blowing are tested in the present work, including variations in blowing/suction velocity and location. In Figs. 1.4 (a) and (b), blowing is applied at the airfoil trailing edge for surfaces 1 and 2, respectively. When the steady blowing is applied, a streamwise flow is set to come out of the surface over the region $0.97 \leq x \leq 0.98$ for surface 1 and $0.79 \leq x \leq 0.80$ for surface 2. When suction is applied, an opposite streamwise flow is set to enter the surface over the same region. Figure 1.4 (c) shows a case where suction is applied at the airfoil trailing edge for surface 1, and Fig. 1.4 (d) shows a simulation where suction is applied over the region $0.3 \leq x \leq 0.98$ along the airfoil upper surface. In the next sections, results are presented only for suction and blowing applied in the airfoil trailing edge. When suction is applied along the suction side of the airfoil, the boundary layer is stabilized and the vortical structures which are convected towards the trailing edge disappear.

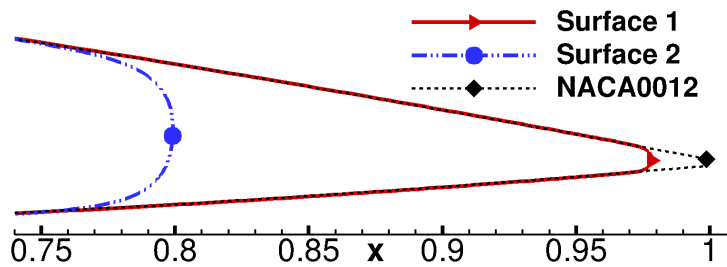


Figure 1.3: Trailing edge profiles of the configurations analyzed.

Table 1.1: Details of the configurations analyzed.

Airfoil	Chord (c)	TE radius (r)	% r/c
Surface 1 (thinner trailing edge surface)	0.98	0.0040	0.408
Surface 2 (thicker trailing edge surface)	0.80	0.0250	3.125

The main contributions of this work are:

- New physical insights to the “trailing edge bluntness–vortex-shedding (TEB-VS)

Table 1.2: Features of studied baseline cases.

Airfoil	AoA	Reynolds Re_c	Mach number M_∞
Surface 1	3 deg.	5000	0.1, 0.2 and 0.3
Surface 2	3 deg.	5000	0.1, 0.2 and 0.3
Surface 1	0 and 3 deg.	10000	0.1, 0.2 and 0.3
Surface 2	0 and 3 deg.	10000	0.1, 0.2 and 0.3
Surface 1	0 and 3 deg.	50000	0.1, 0.2 and 0.3
Surface 2	0 and 3 deg.	50000	0.1, 0.2 and 0.3
Surface 1	0 and 3 deg.	100000	0.1, 0.2 and 0.3
Surface 2	0 and 3 deg.	100000	0.1, 0.2 and 0.3

noise”:

The effects of trailing edge bluntness on noise generation and propagation over a NACA 0012 airfoil with four different blunt trailing edge geometries were investigated for low to moderate Mach numbers and low Reynolds numbers. Results show that, for increased Mach number, the dominant tonal peak increases in amplitude and shifts to higher frequencies. For increased trailing edge bluntness, the dominant tonal peak increases in amplitude and shifts to lower frequencies. Furthermore, it is found that, a blunter trailing edge surface emits more noise than a thinner one due to an increase in the magnitudes of quadrupole sources near the trailing edge region. It is also found that the peak values of the quadrupole sources get closer to the airfoil surface for blunter trailing edges, which also increases noise scattering. The present results also show that the dominant tonal noise frequencies follow Pater-son’s power law equation for the thinner trailing edges investigated but not for the blunter ones. The outcomes of these contributions led to a publication in the *Journal of the Brazilian Society of Mechanical Science and Engineering* (ARIAS-RAMIREZ AND WOLF, 2015b).

- Airfoil may emit multiple “narrow-band” tones superimposed on a broadband hump, depending on the flow configuration:

Numerical results for the low Reynolds number flows studied show that the airfoil emits a single “narrow-band” tone due to vortex shedding at the trailing edge. Results for the moderate Reynolds number flows analyzed show that the airfoil may emit multiple “narrow-band” tones superimposed on a broadband hump, depending on the flow configuration. Compressibility effects play a major role in the tonal noise generation process when the airfoil with the thinner trailing edge is at zero angle of attack. For $M_\infty = 0.1$, the flow is symmetric and the presence of secondary tones due to an acoustic feedback loop is questionable. When the freestream Mach number is increased to $M_\infty = 0.3$, the flow becomes non-symmetric and secondary tones are clearly visible superimposed on a broadband hump. When the airfoil with a thinner

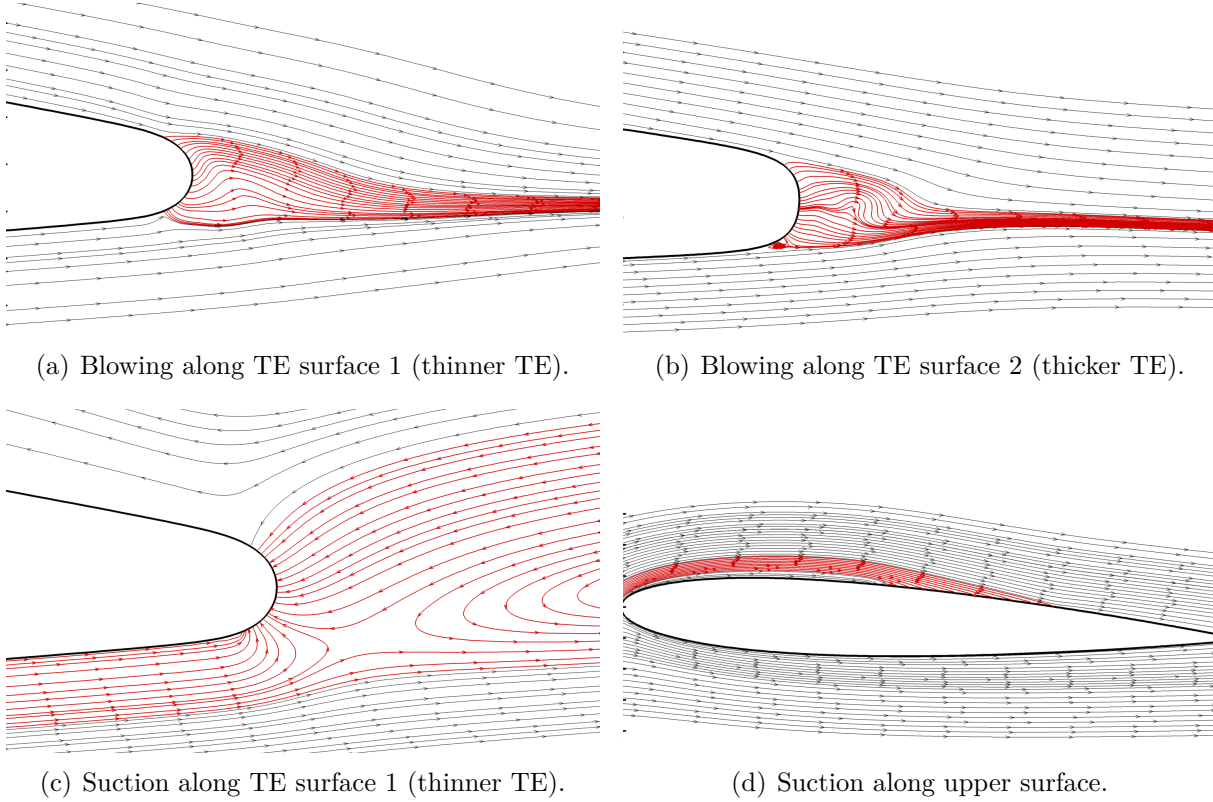


Figure 1.4: Examples of suction and blowing along airfoil surface.

trailing edge is at an angle of incidence, it exhibits a spectrum with secondary tones and the acoustic feedback loop is present. Compressibility effects do not play a major role for these cases.

- Blowing is shown to reduce trailing edge noise generation for low Reynolds numbers flows, and it can eliminate the secondary tones for some of the moderate Reynolds number flow configurations:

Blowing is shown to reduce trailing edge noise generation by moving the quadrupolar incident field away from the airfoil surface and, hence, reducing the scattered field. Suction, on the other hand, shows the opposite effect. Meanwhile, for moderate Reynolds number regimes and $M_\infty = 0.1$, suction and blowing increases far field noise at the main tonal frequency and secondary tones appear when blowing is applied. For $M_\infty = 0.3$, suction and blowing reduce the amplitudes of the tonal peaks which occur at lower frequencies. For the blunter trailing edge, at $AoA = 0^\circ$, the tonal noise mechanism is similar to that of the low Reynolds number flows. Thus, blowing reduces the acoustic scattering in a similar fashion as for the low Reynolds number case. The outcomes of these contributions led to a publication in the *21st AIAA/CEAS Aeroacoustics Conference* (ARIAS-RAMIREZ AND WOLF, 2015a).

- Appearance of shear layer vortices and vortex merging phenomena along the boundary layer: Numerical results for some cases of moderate Reynolds numbers show the

Table 1.3: Features of cases studied using suction & blowing.

Airfoil	AoA	Re_c	M_∞	% Suction	% Blowing
Surface 1	3 deg.	5000	0.1	5% and 10% of M_∞	–
Surface 1	3 deg.	5000	0.3	5% and 10% of M_∞	–
Surface 2	3 deg.	5000	0.1	5% and 10% of M_∞	–
Surface 2	3 deg.	5000	0.3	5% and 10% of M_∞	–
Surface 1	3 deg.	5000	0.1	–	5% and 10% of M_∞
Surface 1	3 deg.	5000	0.3	–	5% and 10% of M_∞
Surface 2	3 deg.	5000	0.1	–	5% and 10% of M_∞
Surface 2	3 deg.	5000	0.3	–	5% and 10% of M_∞
Surface 1	0deg.	100000	0.1	5% of M_∞	–
Surface 1	3deg.	100000	0.1	5% of M_∞	–
Surface 1	0deg.	100000	0.3	5% of M_∞	–
Surface 1	3deg.	100000	0.3	5% of M_∞	–
Surface 1	0deg.	100000	0.1	–	5% of M_∞
Surface 1	3deg.	100000	0.1	–	5% of M_∞
Surface 1	0deg.	100000	0.3	–	5% of M_∞
Surface 1	3deg.	100000	0.3	–	5% of M_∞
Surface 2	0deg.	100000	0.1	–	10% of M_∞
Surface 2	3deg.	100000	0.1	–	10% of M_∞
Surface 2	0deg.	100000	0.3	–	10% of M_∞
Surface 2	3deg.	100000	0.3	–	10% of M_∞

appearance of vortices along the shear layer as well as vortex merging.

- Created a two-dimensional *DNS* database for airfoil self-noise generation and propagation:

High-fidelity computations of compressible flows with different parameters past a NACA 0012 are performed. Through these sets of simulations, several trends are shown to improve the understanding of the fundamental physics involved in airfoil noise generation mechanisms.

1.5 Outline of the Current study

Chapter 2 presents the theoretical and numerical formulations employed in this work. In this chapter, the numerical techniques of the CFD tool and acoustic analogy implemented are explained in details. Chapter 3 presents results for low Reynolds number flows. Chapter 4 explains the findings for moderate Reynolds numbers flows. In both chapters the effects of compressibility, trailing edge bluntness and effects of suction & blowing are presented. Appendix A presents further details of novel numerical techniques which can be applied for the study of airfoil noise. In this appendix, results are shown for several canonical

problems involving wave diffraction. These results are an outcome of a 6-month internship at Lawrence Livermore National Laboratory performed by the present author.

2 THEORETICAL AND NUMERICAL FORMULATION

2.1 Introduction

The combined direct numerical simulation of both noise generation, and its subsequent propagation to the far field, is prohibitively expensive due to mesh resolution requirements. Therefore, hybrid methods are typically employed, in which computational fluid dynamics (CFD) tools are used to calculate the near flowfield quantities responsible for the sound generation, which are then used as an input to a propagation formulation that computes the far field noise radiation. The flow physics associated with sound generation must be accurately captured in the CFD calculation in order to be used in this context.

The flow regimes analyzed in the present work give rise to noise sources at different ranges of frequencies and spatial scales. Thus, since our intention is to perform high-fidelity simulations to capture the energetic scales associated with noise generation, compressible direct numerical simulation (DNS) is chosen as the numerical method for the flow simulations.

In this chapter, the equations governing the compressible flows responsible for sound generation and those equations that govern the acoustic propagation are introduced. Section 2.2 presents the general curvilinear form of the compressible Navier Stokes equations, section 2.3 summarizes the numerical methods used in the spatial discretization; the time marching schemes are given in section 2.4 and the boundary conditions used for the whole set of simulations are described in section 2.6. Finally, section 2.7 shows the acoustic analogy formulation of Ffowcs Williams and Hawkings (1969) which is applied along the work for the acoustic predictions.

2.2 Flow Simulations

The present direct numerical simulations solve the non-dimensional compressible Navier Stokes equations in their covariant form on a general curvilinear system. The equations provided by Nagarajan (2004) are written in conservation form as

$$\frac{\partial \rho}{\partial t} + \frac{\partial(\rho u^i)}{\partial x_i} = 0, \quad (2.1)$$

$$\frac{\partial(\rho u^i)}{\partial t} + \frac{\partial(\rho u^i u^j + g^{ij} p - \tau_{ij})}{\partial x_j} = 0, \quad (2.2)$$

$$\frac{\partial E}{\partial t} + \frac{\partial[(E + p)u^j - \tau_{ij} g_{ik} u^k + q_j]}{\partial x_j} = 0, \quad (2.3)$$

where u^i , ρ , and p are the contravariant velocity components, density and pressure, respectively. The total energy, E , the viscous stress tensor, τ_{ij} , and the heat flux for a fluid obeying Fourier's law, q_j , are given by

$$E = \frac{p}{\gamma - 1} + \frac{1}{2} \rho g_{ik} u^i u^k, \quad (2.4)$$

$$\tau_{ij} = \frac{\mu}{Re} \left(g^{jk} \frac{\partial u^i}{\partial x_k} + g^{ik} \frac{\partial u^j}{\partial x_k} - \frac{2}{3} g^{ij} \frac{\partial u^k}{\partial x_k} \right), \quad (2.5)$$

$$q_j = -\frac{\mu}{Re Pr} g^{ij} \frac{\partial T}{\partial x_i}, \quad (2.6)$$

respectively. Assuming the medium to be a perfect gas, the set of equations is closed by the following equation of state

$$p = \frac{\gamma - 1}{\gamma} \rho T. \quad (2.7)$$

In the equations above, g_{ij} , and g^{ij} are the covariant and contravariant metric tensors, respectively. Considering the general curvilinear system of coordinates (x_1, x_2) , and the associated Cartesian system (ξ_1, ξ_2) , the covariant metric tensor, g_{ij} , is defined as $g_{ij} = \sum_{k=1}^2 \frac{\partial \xi_k}{\partial x_i} \frac{\partial \xi_k}{\partial x_j}$, and the contravariant metric tensor, g^{ij} is the inverse of g_{ij} . These metric terms are calculated in a pre-processing step using a sixth-order compact scheme with the usual appropriate modifications near the boundaries (LELE, 1992). In order to obtain smooth metric terms, the grid is filtered using a high-wavenumber compact filter. The equations are solved in non-dimensional form where length, velocity components, density, pressure and temperature are non-dimensionalized by the chord length, c , free-stream speed of sound, c_∞ , free-stream density, ρ_∞ , $\rho_\infty c_\infty^2$ and $(\gamma - 1)T_\infty$, respectively. Here, T is the temperature, γ is the ratio of specific heats, Re_c is the Reynolds number based on the airfoil chord, defined as $Re_c = \rho_\infty U_\infty c / \mu_\infty$. Here, U_∞ is the magnitude of the free-stream velocity and Pr is the Prandtl number defined as $Pr = \mu_\infty C_p / \kappa_\infty$ where C_p is the heat capacity at constant pressure, μ_∞ is the dynamic viscosity coefficient and κ is the thermal conductivity coefficient.

The numerical scheme for spatial discretization is a sixth-order-accurate compact scheme implemented on a staggered grid (NAGARAJAN *et. al*, 2003). Compact finite-difference schemes are non-dissipative and numerical instabilities arising from insufficient grid resolution, mesh non-uniformities, approximate boundary conditions and interpola-

tion at grid interfaces have to be filtered to preserve stability. The compact filter proposed by Lele (1992) is applied to the computed solution at prescribed time intervals in order to control numerical instabilities. This filter is only applied in flow regions far away from boundary layers. The time integration of the fluid equations is carried out by the fully implicit second-order scheme of Beam and Warming (1978) in the near-wall region (see red mesh in Fig. 2.1 (b)) in order to overcome the time step restriction which appears in explicit schemes. A third-order Runge-Kutta scheme is used for time advancement of the equations in flow regions far away from solid boundaries. No-slip adiabatic wall boundary conditions are applied along the solid surfaces.

Two **O**-type meshes are used in the simulations (see Fig. 2.1 (a)). The first has 400×700 points in the azimuthal and normal directions, respectively, and it is employed for simulations with $Re_c = 5000$ and $Re_c = 10000$. The second mesh has 400×900 points and it is used for the $Re_c = 50000$ and $Re_c = 100000$ cases. One should notice that the last point of the mesh appearing in Fig. 2.1 is not shown in order to visualize the **O**-mesh cut where periodical boundary conditions are enforced. It should be clear that, in the numerical calculations, the mesh is “closed” and the last point in the azimuthal direction is the same as the first point. The domain extends 45 chords from the airfoil in each direction and characteristic plus sponge boundary conditions are applied in the far-field locations to minimize acoustic wave reflections. A mesh refinement study was previously performed and only converged results are presented in the present work. The explicit and implicit meshes shown in Figs. 2.1 (a) and (b) have 400×550 and 400×150 points, respectively, and 400×650 and 400×250 points. The former and latter meshes are employed for the calculations at low Reynolds number flows and moderate Reynolds number flows, respectively. The large number of grid points and relatively small domain size ensures that the acoustic waves generated by the airfoil remain well resolved as one moves away from the solid surface. Furthermore, the boundary layers are also accurately resolved along the airfoil surface. Information about the two **O**-type meshes employed in the calculations is summarized in table 2.1.

Table 2.1: Characteristics of meshes employed in the simulations.

Re_c	AoA	Implicit Mesh	Total Mesh	$dz0$	$dz1$
5000 & 10000	0 and 3 deg.	400×150	400×700	5×10^{-4}	0.3
50000 & 100000	0 and 3 deg.	400×250	400×900	2×10^{-4}	0.3

Here, $dz0$ and $dz1$ are the wall and far field mesh resolutions in the wall normal direction. The **O**-mesh domain extends 45 chords from the airfoil in each direction.

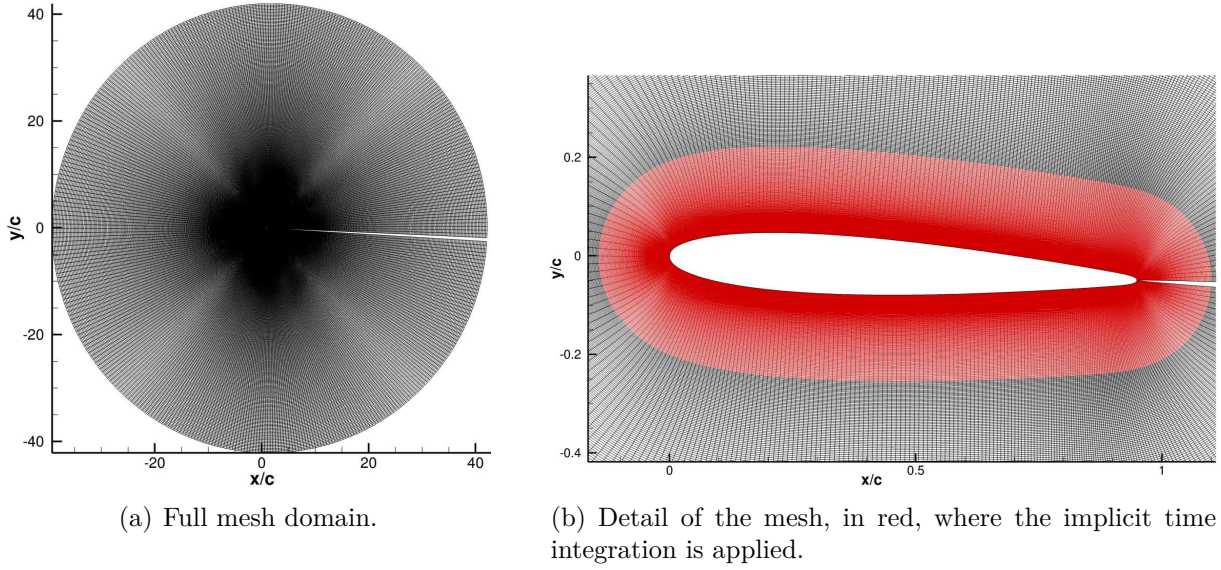


Figure 2.1: Mesh configuration for the studied cases.

2.3 Spatial Discretization

The numerical scheme for spatial discretization is a sixth-order accurate compact scheme (NAGARAJAN *et. al*, 2003) implemented on a staggered grid. In a general curvilinear coordinate system, the staggered first derivative, f' , of a function f at interior nodes is computed as

$$\alpha f'_{j-1} + f'_j + \alpha f'_{j+1} = b \frac{f_{j+3/2} - f_{j-3/2}}{3\Delta x} + a \frac{f_{j+1/2} - f_{j-1/2}}{\Delta x}, \quad (2.8)$$

where $\alpha = 9/62$, $a = 3/8(3 - 2\alpha)$ and $b = 1/8(-1 + 22\alpha)$. The use of a staggered variable arrangement requires a mid-point interpolation formula. The implemented sixth-order accurate formula is given by

$$\alpha f^I_{j-1} + f^I_j + \alpha f^I_{j+1} = b \frac{f_{j+3/2} - f_{j-3/2}}{2} + a \frac{f_{j+1/2} - f_{j-1/2}}{2}, \quad (2.9)$$

where $\alpha = 3/10$, $a = 1/8(9 + 10\alpha)$ and $b = 1/8(-1 + 6\alpha)$. The boundary and near-boundary nodes require one side derivative and interpolation formulas that can be found in (NAGARAJAN, 2004).

Compact finite-difference schemes are non-dissipative and numerical instabilities arising from insufficient grid resolution, mesh non-uniformities, approximate boundary conditions and interpolation at grid interfaces have to be filtered to preserve stability of the numerical schemes. The high wavenumber compact filter presented by Lele (1992), is applied to the computed solution at prescribed time intervals in order to control numerical

instabilities. A one parameter family of sixth-order filters is constructed using

$$\alpha \tilde{f}_{j-1} + \tilde{f}_j + \alpha \tilde{f}_{j+1} = af_j + b \frac{f_{j+1} + f_{j-1}}{2} + c \frac{f_{j+2} + f_{j-2}}{2} + d \frac{f_{j+3} + f_{j-3}}{2}, \quad (2.10)$$

where \tilde{f}_j is the filtered solution, $a = 1/16(11+10\alpha)$, $b = 1/32(15+34\alpha)$, $c = 1/16(-3+6\alpha)$ and $d = 1/32(1-2\alpha)$. The spectral response of the filter is adjusted by the filter coefficient α that ranges from $-0.5 \leq \alpha \leq 0.5$. Higher values of α provide less dissipation and values of $\alpha \geq 0.48$ are used in the present computations. The boundary nodes use different filtering formulas that can be found in (BHASKARAN AND LELE, 2010).

2.4 Time Integration

Far away from the solid boundaries, the governing equations are integrated using an explicit third-order compact storage Runge-Kutta scheme. After the spatial discretization, the set of partial differential equations become a set of ordinary differential equations that can be expressed in the form

$$\frac{dQ}{dt} = f(Q, t). \quad (2.11)$$

This set of ordinary differential equations can be integrated from t^n to t^{n+1} using the following third-order Runge-Kutta scheme

$$\begin{aligned} Q^{n+1/3} &= Q^n + \frac{8}{15} \Delta t f(Q^n, t^n) \\ Q^{n+2/3} &= Q^n + \frac{1}{4} \Delta t f(Q^n, t^n) + \frac{5}{12} \Delta t f(Q^{n+1/3}, t^{n+1/3}) \\ Q^{n+1} &= Q^n + \frac{1}{4} \Delta t f(Q^n, t^n) + \frac{3}{4} \Delta t f(Q^{n+2/3}, t^{n+2/3}), \end{aligned} \quad (2.12)$$

where the intermediate time levels are $t^{n+1/3} = t^n + 8/15 \Delta t$ and $t^{n+2/3} = t^n + 2/3 \Delta t$. The time integration of the fluid equations is carried out by a fully implicit second-order Beam-Warming scheme (BEAM AND WARMING, 1978) in the near-wall region in order to overcome the time step restriction, typical of explicit time marching schemes. The second-order implicit method is given by

$$\frac{3Q^{n+1} - 4Q^n + Q^{n-1}}{2\Delta} = f(Q^{n+1}, t^{n+1}). \quad (2.13)$$

The right hand side is solved through approximate factorization followed by diagonalization of the implicit matrix in the x and z directions. Details about the approximate factorization are presented by Nagarajan in (NAGARAJAN, 2004).

2.5 Boundary Conditions

Sponge layers and characteristic boundary conditions based on Riemann invariants are applied at inflow and outflow boundaries. For a subsonic inflow boundary, four incoming quantities must be specified along with one outgoing quantity computed from the interior domain. In the current study, the entropy, tangential velocities and incoming Riemann invariant are constrained. The outgoing Riemann invariant is computed by extrapolation from the interior nodes neighboring the inflow boundary. For a subsonic outflow boundary, one incoming quantity must be specified along with four outgoing quantities computed from the interior domain. Here, the incoming Riemann invariant is imposed and the entropy, tangential and outgoing Riemann invariant are computed by extrapolation from the interior nodes neighboring the outflow boundary.

Assuming an inflow boundary located at a x plane normal to the inflow, the locally one-dimensional Riemann invariants are defined in the normal direction as

$$R_1 = u - \frac{2c}{\gamma - 1} \quad (2.14)$$

and

$$R_2 = u + \frac{2c}{\gamma - 1}, \quad (2.15)$$

where u is the velocity in the x Cartesian direction normal to the inflow and c is the local speed of sound. Hence, at the inflow boundary, the following constraints are applied $v = v_{inflow}$, $s = s_{inflow}$, $R_1 = R_{1_{incoming}}$ and $R_2 = R_{2_{outgoing}}$. The outgoing Riemann invariant, R_2 , is computed using zero-th order extrapolation from the plane immediately neighboring the inflow plane. The primitive variables can be constructed from the constraints as

$$u = \frac{1}{2}(R_{1_{incoming}} + R_{2_{outgoing}}), \quad (2.16)$$

$$c = \frac{\gamma - 1}{4}(R_{2_{outgoing}} - R_{1_{incoming}}), \quad (2.17)$$

$$\rho = \left(\frac{c^2}{\gamma s_{inflow}} \right)^{\frac{1}{\gamma - 1}} \quad (2.18)$$

and

$$T = \frac{c^2}{\gamma - 1}. \quad (2.19)$$

The same methodology applies to an outflow boundary condition. However, only the incoming Riemann invariant is imposed and the other constraints are obtained by zero-th order extrapolation from the interior plane immediately neighboring the outflow plane.

In the current simulations, both inflow and outflow boundary conditions are applied on the background mesh, where an explicit time marching scheme is used. At each time step the solutions in the inflow and outflow planes are updated with those obtained from the application of the inflow and outflow boundary conditions, respectively. The boundary conditions are applied after transformation to a Cartesian coordinate system along a normal to the boundary plane. The velocity components are first evaluated at the density nodes and then interpolated to their respective staggered locations.

A damping sponge layer is also applied along the inflow and outflow boundaries to minimize reflections of disturbances (NAGARAJAN; BHASKARAN AND LELE, 2004; 2010). In the sponge layers, the following relaxation term is added to the governing equations

$$- \sigma(Q - Q_{ref}), \quad (2.20)$$

where σ is the sponge strength specified as

$$\sigma = A \left(\frac{x - x_{sponge}}{L - x_{sponge}} \right)^n. \quad (2.21)$$

Here, x_{sponge} is the starting sponge location and L is the full length of the sponge layer. The sponge effect vanishes at the starting location and gradually grows in the strength as the maximum size of the sponge is reached. The sponge reference solution, Q_{ref} , is specified as the freestream condition. The constants A and n used in the present computations are $A = 20$ and $n = 4$. These values are found by numerical experimentation and provide good results for the present grid and flow configurations.

Adiabatic, no-slip boundary conditions are applied at the solid boundaries. The wall density is obtained by the solution of the continuity equation

$$\frac{\partial \rho}{\partial t} + \frac{\partial(\rho u_i)}{\partial x_i} = 0. \quad (2.22)$$

The momentum and energy equations are replaced by the following constraints on the velocity

$$\rho u_i = 0 \quad (2.23)$$

and temperature

$$\frac{\partial T}{\partial n} = 0, \quad (2.24)$$

where the term $\partial(\cdot)/\partial n$ represents a derivative in the wall-normal direction.

2.6 Acoustic Analogy Formulation and Noise Predictions

The near flow-field provides the required data for an acoustic analogy prediction of far-field noise, which can then be compared to results provided by the direct numerical simulation. In this work, the Ffowcs Williams-Hawkings (1969) (FWH) acoustic analogy formulation is used to predict the acoustic fields radiated by the unsteady flow simulations. It is applicable to bodies in arbitrary motion, however, in the present work, noise sources and observer locations are assumed to be in steady uniform motion in a stagnant medium. Therefore, following the development of Lockard (2000), we apply a Galilean transformation to the FWH equation to write a formulation for steady uniform motion. Considering a mean flow in the x_1 Cartesian direction and writing the surface velocity vector $v_i = (-U_1, 0, 0)^t$, the FWH formulation can be written as

$$\left(\frac{\partial}{\partial t} + U_1 \frac{\partial}{\partial x_1} \right)^2 [\rho' H(f)] - c_\infty^2 \frac{\partial^2 [\rho' H(f)]}{\partial x_j \partial x_j} = \frac{\partial [Q \delta(f)]}{\partial t} - \frac{\partial [F_i \delta(f)]}{\partial x_i} + \frac{\partial^2 [T_{ij} H(f)]}{\partial x_i \partial x_j}, \quad (2.25)$$

where ρ' stands for the acoustic density, c_0 is the freestream speed of sound and U_1 is the mean flow velocity in the x_1 Cartesian direction.

The monopole and dipole source terms are

$$Q = [\rho(u_i + U_i) - \rho_0 U_i] \partial f / \partial x_i \quad (2.26)$$

and

$$F_i = [p \delta_{ij} - \tau_{ij} + \rho(u_i - U_i)(u_j + U_j) + \rho_0 U_i U_j] \partial f / \partial x_j, \quad (2.27)$$

respectively, and T_{ij} is the Lighthill stress tensor or quadrupole source term given by

$$T_{ij} = \rho u_i u_j + (p' - c_0^2 \rho') \delta_{ij} - \tau_{ij}. \quad (2.28)$$

Here, u_i is the fluid velocity vector, p is the pressure, ρ_0 is the freestream density, p' is the acoustic pressure, δ_{ij} is the Kronecker delta and τ_{ij} is the viscous stress tensor, whose effects are considered negligible for the acoustic problems analyzed in the present work. The term $f = 0$ represents the FWH surface and $H(f)$ is the Heaviside function defined as $H(f) = 1$ for $f > 0$ and $H(f) = 0$ for $f < 0$. Figure 2.2 shows a sketch where the FWH surface is located along the solid wall of an airfoil.

The solution of the FWH formulation in the time domain presents advantages and drawbacks that are application dependent. While time domain formulations are the natural choice for problems with non-periodic sound generation (LYRINTZIS, 2003), frequency

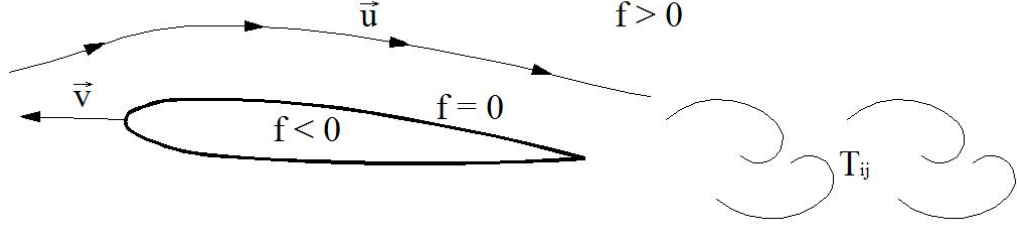


Figure 2.2: Sketch with notation used in the Ffowcs Williams-Hawkins equation.

domain formulations require simpler implementation and can provide sound data for specific frequencies of interest. Besides these differences, Lockard (2002) shows that frequency domain methods present lower computational cost compared to time domain methods even when multiple frequencies are analyzed and that time domain formulations can have stability issues regarding frequency of data sampling. Therefore, the frequency domain method is applied in the present work. Applying a Fourier transform to Eq. 2.25, it can be written in the frequency domain as

$$\left[(1 - M_\infty^2) \frac{\partial^2}{\partial x_1^2} + \frac{\partial^2}{\partial x_2^2} + \frac{\partial^2}{\partial x_3^2} + k^2 + i2kM_\infty \frac{\partial}{\partial x_1} \right] [\hat{p}'H(f)] = \quad (2.29)$$

$$- [i\omega \hat{Q}\delta(f)] - \frac{\partial [\hat{F}_i\delta(f)]}{\partial x_i} + \frac{\partial^2 [\hat{T}_{ij}H(f)]}{\partial x_i \partial x_j},$$

where M_∞ is the freestream Mach number defined as $M \equiv U_1/c_0$, \hat{p}' , \hat{Q} , \hat{F}_i and \hat{T}_{ij} are the frequency domain acoustic pressure, monopole, dipole, and Lighthill stress terms, respectively, and $k = \omega/c_\infty$ is the wavenumber. Equation 2.29 can be rewritten as the Helmholtz equation after a Prandtl-Glauert transformation and, then, the 2D convective Green's function can be obtained as shown by Lockard (LOCKARD, 2000) as

$$G_c(\vec{x}, \vec{y}) = \frac{ie^{iM \frac{k}{(1-M^2)}(x_1-y_1)}}{4\sqrt{1-M^2}} H_0^{(2)} \left(\frac{k}{(1-M^2)} \sqrt{(x_1-y_1)^2 + (1-M^2)(x_2-y_2)^2} \right). \quad (2.30)$$

In Eq.2.30, \vec{x} is an observer location, \vec{y} is a source location and $H_0^{(2)}$ is the Hankel function of the second kind and order zero. After some manipulations of Eq. (2.26) (see (LOCKARD, 2000) for details), one can write the following integral equation for the acoustic pressure field solution

$$[\hat{p}'H(f)] = - \int_{f=0} \left[i\omega \hat{Q}(\vec{y}) G_c(\vec{x}, \vec{y}) + \hat{F}_i(\vec{y}) \frac{\partial G_c(\vec{x}, \vec{y})}{\partial y_i} \right] dS - \quad (2.31)$$

$$\int_{f>0} \hat{T}_{ij} H(f) \frac{\partial^2 G_c(\vec{x}, \vec{y})}{\partial y_i \partial y_j} dV.$$

In the present work, the surface integrations appearing in Eq.2.31 are computed along the scattering body surfaces. Therefore, $u_i = -U_i$ for the monopole and dipole source terms, which are then given by $Q = -\rho_0 U_i \partial f / \partial y_i$ and $F_i = [p \delta_{ij} + \rho_0 U_i U_j] \partial f / \partial y_j$, respectively. Furthermore, one can observe that the monopole source terms, Q , and the second component of the dipole source terms, $\rho_0 U_i U_j$, are steady in time and do not appear in the frequency domain formulation. The volume integrations in Eq. (2.31) are computed along the entire computational domain.

To obtain the dipole and quadrupole terms of equation 2.31, the derivatives of the 2D convective Green's Function (equation 2.30) are required. Equations 2.32 and 2.33 provide the first derivatives of the Green's function with respect to the source locations y_1 and y_2 , respectively. To simplify the equations, the argument of the Hankel function is assumed as a variable z , where z is given in Eq. 2.34.

$$\frac{\partial G_c(\vec{x}, \vec{y})}{\partial y_1} = \frac{i M k^2 e^{i(\frac{M k(x_1 - y_1)}{(1 - M^2)})}}{4(1 - M^2)^{5/2}} \left[\frac{H_1^{(2)}(z)}{\sqrt{(x_1 - y_1)^2 + (1 - M^2)(x_2 - y_2)^2}} - \frac{M H_0^{(2)}(z)}{(x_1 - y_1)} \right]. \quad (2.32)$$

$$\frac{\partial G_c(\vec{x}, \vec{y})}{\partial y_2} = \frac{i M k^2 (x_1 - y_1)}{4(1 - M^2)^{3/2}} \frac{(x_2 - y_2) e^{i(\frac{M k(x_1 - y_1)}{(1 - M^2)})} H_1^{(2)}(z)}{\sqrt{(x_1 - y_1)^2 + (1 - M^2)(x_2 - y_2)^2}}. \quad (2.33)$$

$$z = \frac{k}{(1 - M^2)} \sqrt{(x_1 - y_1)^2 + (1 - M^2)(x_2 - y_2)^2} \quad (2.34)$$

Equations 2.35 and 2.36 present recurrence relations for the derivatives of the Hankel function and which are used in the computation of the derivatives of the current Green's function. The Hankel function of the second kind and order α is defined as $H_\alpha^{(2)}(z) = J_\alpha(z) - iY_\alpha(z)$, where J is the Bessel function of order α and Y is the Neumann function of order α .

$$\left(\frac{1}{z} \frac{d}{dz} \right)^m \left[\frac{H_\alpha^{(2)}(z)}{z^\alpha} \right] = (-1)^m \frac{H_{\alpha+m}^{(2)}(z)}{z^{\alpha+m}} \quad (2.35)$$

$$\frac{dH_\alpha^{(2)}(z)}{dz} = \frac{H_{\alpha-1}^{(2)}(z) - H_{\alpha+1}^{(2)}(z)}{2}. \quad (2.36)$$

Equations 2.37 and 2.38 give the second derivatives of the Green's function with respect to y_1 and y_2 , respectively. Finally, Eq. 2.39 presents the formula obtained for the mixed

second derivative with respect to both y_1 and y_2 .

$$\begin{aligned} \frac{\partial^2 G_c(\vec{x}, \vec{y})}{\partial y_1^2} = & \frac{e^{i(\frac{Mk(x_1-y_1)}{(1-M^2)})}}{4\sqrt{1-M^2}} \left[\frac{M^2 k^2 H_0^{(2)}(z)}{(1-M^2)^2} - \frac{i2Mk^2(x_1-y_1)H_1^{(2)}(z)}{(1-M^2)^2 \sqrt{(x_1-y_1)^2 + (1-M^2)(x_2-y_2)^2}} + \right. \\ & - \frac{k(x_1-y_1)H_1^{(2)}(z)}{2\beta^2((x_1-y_1)^2 + (1-M^2)(x_2-y_2)^2)^{3/2}} - \frac{kH_1^{(2)}(z)}{2(1-M^2)\sqrt{(x_1-y_1)^2 + (1-M^2)(x_2-y_2)^2}} + \\ & \left. - \frac{k^2(x_1-y_1)^2}{(1-M^2)^2((x_1-y_1)^2 + (1-M^2)(x_2-y_2)^2)} \left(\frac{H_0^{(2)}(z) - H_2^{(2)}(z)}{2} \right) \right]. \end{aligned} \quad (2.37)$$

$$\begin{aligned} \frac{\partial^2 G_c(\vec{x}, \vec{y})}{\partial y_2^2} = & \frac{e^{i(\frac{Mk(x_1-y_1)}{(1-M^2)})}}{4\sqrt{1-M^2}} \left[-\frac{kH_1^{(2)}(z)}{\sqrt{(x_1-y_1)^2 + (1-M^2)(x_2-y_2)^2}} + \right. \\ & \left. \frac{k(1-M^2)(x_2-y_2)^2 H_1^{(2)}(z)}{((x_1-y_1)^2 + (1-M^2)(x_2-y_2)^2)^{3/2}} - \frac{k^2(x_2-y_2)^2}{(x_1-y_1)^2 + (1-M^2)(x_2-y_2)^2} \left(\frac{H_0^{(2)}(z) - H_2^{(2)}(z)}{2} \right) \right]. \end{aligned} \quad (2.38)$$

$$\begin{aligned} \frac{\partial^2 G_c(\vec{x}, \vec{y})}{\partial y_1 \partial y_2} = & \frac{e^{i(\frac{Mk(x_1-y_1)}{(1-M^2)})}}{4\sqrt{1-M^2}} \left[-\frac{iMk^2(x_2-y_2)H_1^{(2)}(z)}{(1-M^2)\sqrt{(x_1-y_1)^2 + (1-M^2)(x_2-y_2)^2}} + \right. \\ & \left. - \frac{k(x_1-y_1)(x_2-y_2)H_1^{(2)}(z)}{((x_1-y_1)^2 + (1-M^2)(x_2-y_2)^2)^{3/2}} - \frac{k^2(x_1-y_1)(x_2-y_2)}{(x_1-y_1)^2 + (1-M^2)(x_2-y_2)^2} \left(\frac{H_0^{(2)}(z) - H_2^{(2)}(z)}{2} \right) \right]. \end{aligned} \quad (2.39)$$

2.7 Summary

The equations governing the flow simulations and acoustic predictions were presented in this chapter. The flow simulations are discretized and solved numerically using a sixth-order accurate compact scheme implemented on a staggered grid. Two time integration schemes are used to solve the governing equations. Sponge layers and characteristic boundary conditions based on Riemann invariants are applied at inflow and outflow boundaries. Adiabatic, no-slip boundary conditions are applied at the solid boundaries. The FWH equation is solved numerically as a boundary integral equation. In this case, Gaussian quadrature is employed to solve the kernels composed of the convective Green's function and its derivatives.

3 AIRFOIL NOISE PREDICTIONS AT LOW REYNOLDS NUMBERS

3.1 Introduction

This section discusses results obtained by direct numerical simulations and acoustic analogy for low Reynolds number flows past a NACA 0012 airfoil. The flow configurations investigated are described in table 3.1. Here, to display the trends and findings, results are separated in three sections including the effects of compressibility, trailing edge bluntness and trailing edge suction & blowing. Within each section, the Reynolds number based on airfoil chord is varied between $Re_c = 5000$ and 10000 and the angles of incidence of the airfoil with respect to the freestream flow are $AoA = 0$ and 3 degrees. Therefore, the effects of these parameters are also investigated with respect to noise generation and propagation.

Table 3.1: Studied cases for low Reynolds number flows.

Airfoil	AoA	Re_c	M_∞	Suction	Blowing
Surface 1	3 deg.	5000	0.1, 0.2 and 0.3	—	—
Surface 2	3 deg.	5000	0.1, 0.2 and 0.3	—	—
Surface 1	0 deg.	10000	0.1, 0.2 and 0.3	—	—
Surface 1	3 deg.	10000	0.1, 0.2 and 0.3	—	—
Surface 2	0 deg.	10000	0.1, 0.2 and 0.3	—	—
Surface 2	3 deg.	10000	0.1, 0.2 and 0.3	—	—
Surface 1	3 deg.	5000	0.1 and 0.3	5% and 10% of M_∞	—
Surface 2	3 deg.	5000	0.1 and 0.3	5% and 10% of M_∞	—
Surface 1	3 deg.	5000	0.1 and 0.3	—	5% and 10% of M_∞
Surface 2	3 deg.	5000	0.1 and 0.3	—	5% and 10% of M_∞

3.2 Effects of Compressibility on Noise Generation

To examine the effects of compressibility on noise generation and propagation, hydrodynamic and acoustic properties are analyzed and compared. Figure 3.1 shows an enlarged view of the mean flow streamlines at the trailing edge region for surface 1, $AoA = 3$ deg, and $Re_c = 5000$, showing the development of recirculation bubbles for different freestream Mach numbers. Figures 3.1 (a) and (b) present results obtained for freestream Mach numbers $M_\infty = 0.1$ and 0.3 , respectively. One can notice that flow separation occurs further upstream for a flow with higher freestream Mach number and, therefore, the recirculation bubbles become slightly thicker and more elongated.

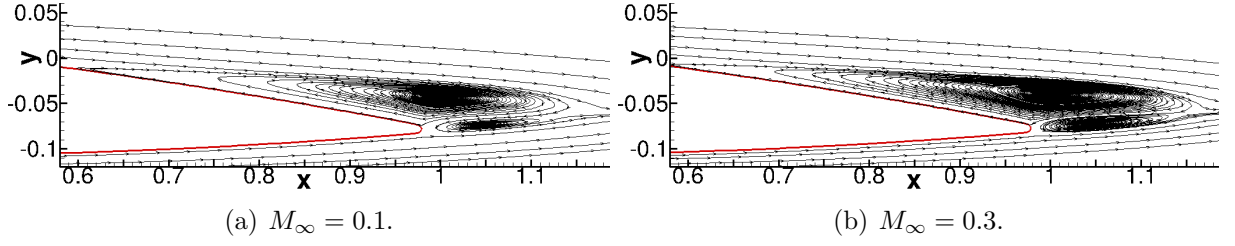


Figure 3.1: Mean flow streamlines at trailing edge region for surface 1, AoA = 3 deg, and $Re_c = 5000$.

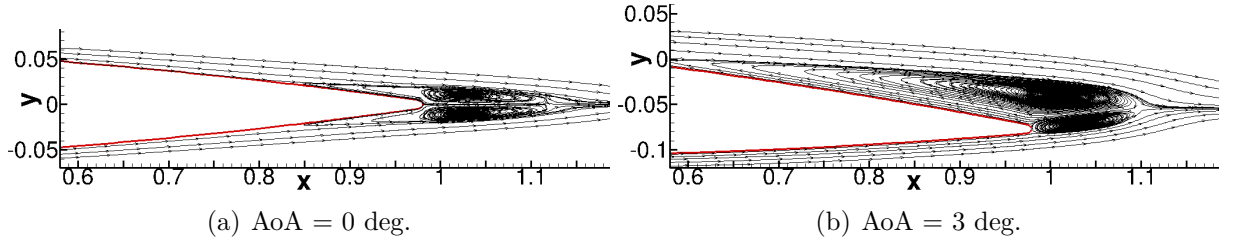


Figure 3.2: Mean flow streamlines at trailing edge region for surface 1, $Re_c = 10000$ and $M_\infty = 0.3$.

Figure 3.2 shows a comparison of the effects of angle of attack on separation which occurs at the trailing edge region. This figure presents mean flow streamlines at the trailing edge region for surface 1, $M_\infty = 0.3$ and $Re_c = 10000$. Similar trends are observed for $M_\infty = 0.1$ and $Re_c = 5000$. From figure 3.2, one can see that a more intense flow separation is caused by the angle of incidence. In this case, the flow fails to remain attached exhibiting a separation bubble along the suction surface of the airfoil caused by a stronger adverse pressure gradient. Along the pressure side, the favorable pressure gradient keeps the laminar boundary layer attached. Meanwhile, for the case with zero incidence (figure 3.2 (b)), only a small symmetric recirculation bubble is observed close to the trailing edge. This separation bubble appears due to the finite thickness of the trailing edge. One should remind that the same Reynolds and Mach used are used for both configurations.

Figures 3.3 (a) - (d) present snapshot plots of vorticity magnitude to characterize the vortical structures shed by the NACA 0012 airfoil with surface 1 (thinner trailing edge) for four different flow configurations. Here, freestream Mach numbers, angles of attack, and Reynolds numbers are varied to compare their effects on vortex shedding. All plots are shown using the same contour levels and, from Figs. 3.3 (a) and (b), one can observe that a larger freestream Mach number leads to vortex shedding with higher vorticity magnitudes. The vorticity levels along the shear layers just downstream of the trailing edge region are also stronger for the higher Mach number case. This effect is expected since velocity variations are higher for higher Mach number flows. Despite these differences in vorticity magnitude, the size and frequency of vortical structures are similar for both

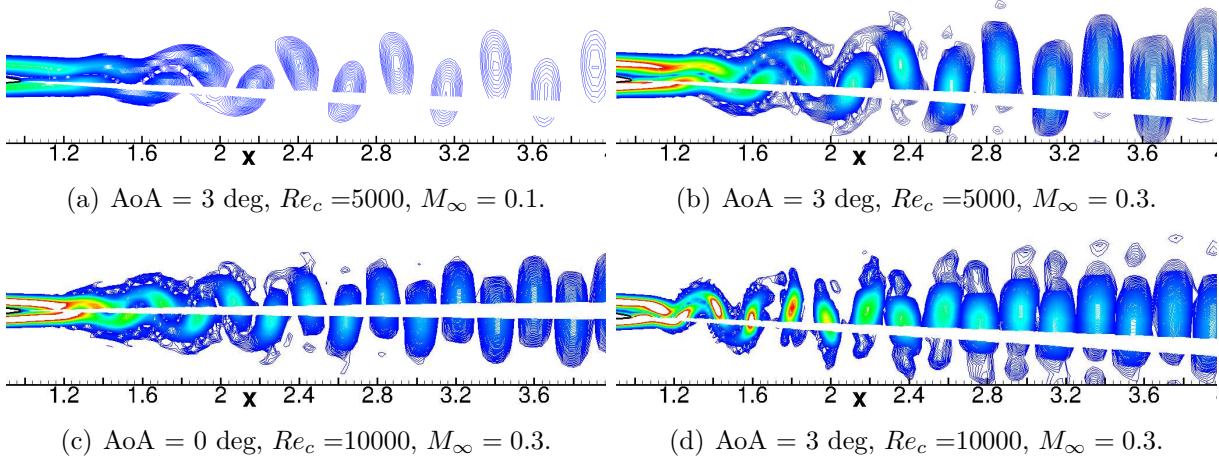


Figure 3.3: Snapshots showing contours of vorticity magnitude over the range $|\omega|=0$ to 5, obtained for NACA 0012 with trailing edge surface 1.

Mach numbers analyzed.

Figures 3.3 (b) and (d) present a comparison of results in terms of Reynolds number ($Re_c = 5000$ and $Re_c = 10000$) while keeping angle of attack and Mach numbers identical. Observing both figures, one can see that vortex shedding is more sensitive with respect to variations in the Reynolds number since vorticity magnitudes and frequency of vortex shedding increase with Reynolds number. For the higher Reynolds number case, vortical structures become closer and show a smaller diffusion effect along the wake. In Figs. 3.3 (c) and (d), one can see a comparison of the effects of angle of incidence in vortex shedding. In this case, Reynolds and Mach numbers are kept the same. The flow configuration at higher angle of attack sheds stronger vortical structures. One can observe a smaller spacing between shed vortices for the case with incidence. This effect occurs due to the stronger separation followed by a larger recirculation bubble observed in figure 3.2 for the mean flow streamlines.

Results demonstrated that compressibility, angle of incidence and Reynolds number effects cause a significant impact in terms of hydrodynamic quantities. It is expected that these flow variations have a further impact on acoustic quantities. Figure 3.4 presents plots of near-field acoustic pressure spectra for different flow configurations with the aim of identifying the effects of Mach number, angle of incidence and Reynolds number on acoustic radiation. These spectra were measured at $1/4$ of chord perpendicular to the trailing edge. These plots present spectra of non-dimensional acoustic pressure as a function of Helmholtz number $kc=2\pi fc$, where k is the acoustic wavenumber, f is the non-dimensional frequency and c is the non-dimensional airfoil chord. Non-dimensional

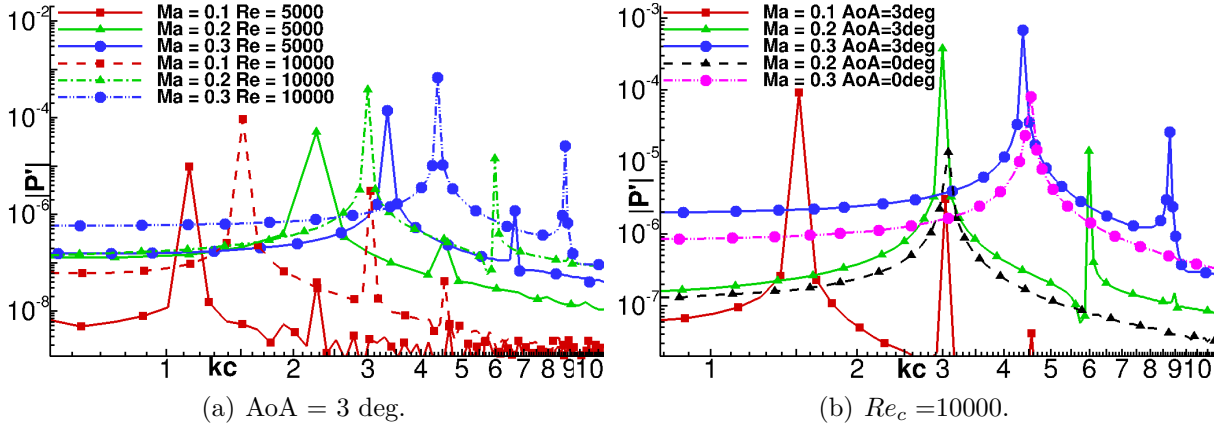


Figure 3.4: Near-field pressure spectra obtained for surface 1 with (a) $AoA = 3$ deg, and (b) $Re_c = 10000$.

quantities are obtained in the same way discussed in Chapter 2. The Helmholtz number is an important parameter which is chosen as a non-dimensional frequency and it provides a measure of the compactness of a source. If the Helmholtz number is larger than 2π , the characteristic length (airfoil chord) is larger the acoustic wavelength and, therefore, the source is non-compact. On the other hand, if the source length is smaller than the acoustic wavelength, the source is considered to be compact. This characterization is of paramount importance in the context of acoustics and it will be discussed along with the results in this document.

One can observe a common pattern for the acoustic pressure spectra shown in figure 3.4. For all flow configurations analyzed, it is possible to observe the presence of a main tonal peak and its harmonics. For low Reynolds number flows, the main noise generation mechanism is the vortex shedding. In this case, the main tonal peaks observed in figure 3.4 occur at the vortex shedding frequency and hydrodynamic variations in the flows are responsible for the modifications observed in the plots of spectra. Figure 3.4 (a) shows a comparison of near-field acoustic pressure for different Reynolds and freestream Mach numbers. Here, the angle of incidence is fixed as $AoA = 3$ deg. One can see that, for larger Mach numbers, the acoustic pressure of the main tonal peak increases in level (clearly observed in fig 3.5) and shifts to higher frequencies. Furthermore, as it can be observed in the same plot, an increase in Reynolds number while keeping the Mach number constant also leads to higher tonal peak amplitudes and frequencies. These remarks are in agreement with what is found in the hydrodynamic results from figure 3.3, supporting the idea that vortex shedding is the main noise generation mechanism for the present low Reynolds number flows as documented by Brooks *et. al.* (BROOKS *et. al.*, 1989). In this case, the coherent vortical structures generate hydrodynamic pressure fluctuations which are scattered by the solid surface of the airfoil. In this process, flow energy of evanescent waves are converted to acoustic energy which radiates as sound.

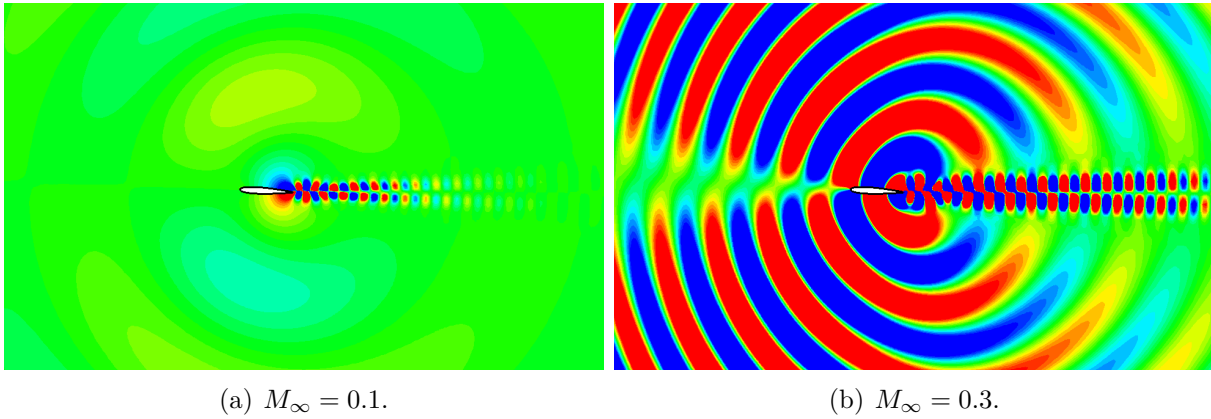


Figure 3.5: Comparison of acoustic pressure contours at vortex shedding frequency over the range $|p'| = \pm 5 \times 10^{-5}$ for surface 1 $\text{AoA} = 3^\circ$, $Re_c = 10000$ and (a) $M_\infty = 0.1$, and (b) $M_\infty = 0.3$.

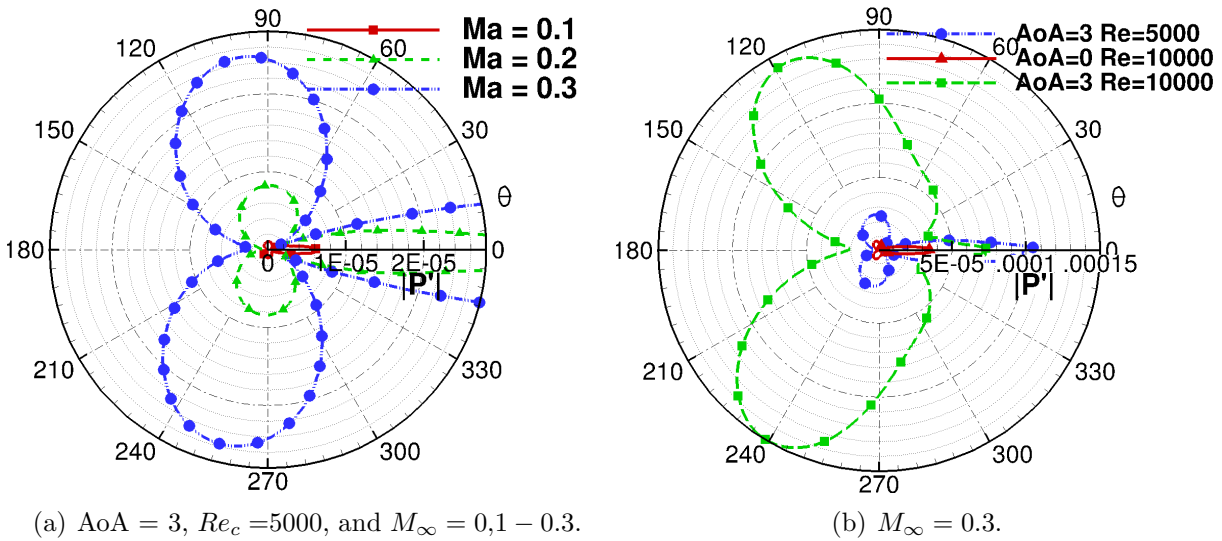


Figure 3.6: Directivities of acoustic pressure, $|p'|$, for an observer location at 5 chords from the airfoil. Results shown for the vortex shedding frequency.

In figure 3.4 (b), one can observe the effects of angle of attack and compressibility on near-field pressure. Here, results are obtained for $\text{AoA} = 3^\circ$, and $Re_c = 10000$. Magnitudes of the main tones are higher when the airfoil is at incidence and frequencies are slightly lower compared against the zero-incidence cases. When the airfoil is at incidence, the boundary layer separation in the suction side is the driver mechanism for the vortex shedding and, the higher the angle of attack, the "blunter" is the airfoil with respect to the flow. This should lead to a thicker boundary layer, larger vortical structures and lower shedding frequencies. Similar results are observed by Wolf and Lele (2011; 2012a).

Figure 3.6 presents results in terms of directivity plots for an observer located 5 chords distant perpendicular to the airfoil trailing edge. In these directivities, magnitude of acoustic pressure is shown at the vortex shedding frequency for different flow configurations.

From figure 3.6 (a), one can observe that far-field noise increases with freestream Mach number. In this case, the angle of attack and the Reynolds number are set as $AoA = 3$ deg, and $Re_c = 5000$, respectively. The directivities in the figure have a dipolar pattern for all Mach numbers presented. This dipolar pattern is typical of sound generation at low frequencies, for compact sources (CURLE, 1955) and, analyzing the FWH equation, it would be a result of unsteady loading along the solid surface of the airfoil. In this case, the unsteady loads would be calculated using the pressure fluctuation along the airfoil. The direction of the noise radiation is perpendicular to the airfoil chord due to the lift fluctuations. Similar observations are presented by Wolf and Lele (2010).

For higher frequencies of noise radiation, the Helmholtz number is increased and the airfoil may become a non-compact source. In this case, the directivity plot will start resembling a cardioid shape as discussed by Ffowcs Williams and Hall (1970). In this case, the main contribution of the noise radiation is directed towards the leading edge of the airfoil. At intermediate frequencies, combined directivity shapes are observed as shown in the green line of figure 3.6 (b) which shows a comparison of results for different Reynolds numbers and angles of incidence for Mach number $M_\infty = 0.3$. Following the same trends from the far-field pressure spectra, this figure shows that the higher Reynolds number flow radiates a more intense vortex shedding far-field noise for the same angle of incidence. A similar behavior is observed when the Reynolds number is set constant and the angle of attack is increased. Furthermore, the angle of incidence effect is stronger than that from the Reynolds number. A comparison in terms of far-field pressure fluctuation between the case at zero incidence and higher Reynolds number and that with incidence and lower Reynolds number confirms the current observation. The results discussed show not only the influence of the Reynolds number over the far-field noise, but also, the noise mechanism associated to the more pronounced boundary layer separation for the non-zero angle of attack case, which is a powerful source of noise.

Figure 3.7 presents the dipole and quadrupole source contributions to total noise for an observer location at 5 chords from the airfoil, at vortex shedding frequency for (a) $AoA = 3$ deg, $Re_c = 5000$ and $M_\infty = 0.3$ and (b) $AoA = 3$ deg, $Re_c = 10000$ and $M_\infty = 0.3$. One can observe the good agreement on the far-field noise, between the DNS and FWH acoustic analogy used in this study.

Arias-Ramirez and Wolf (2015b) show that an increase in Mach number leads to a higher magnitude of pressure fluctuations, $|p'|$, along the airfoil surface. Since these pressure fluctuations represent the intensity of the dipole sources in the noise scattering process along the airfoil surface, one should expect a higher sound generation for higher Mach number flows. In fact, the incident quadrupolar field due to the airfoil vortex shedding

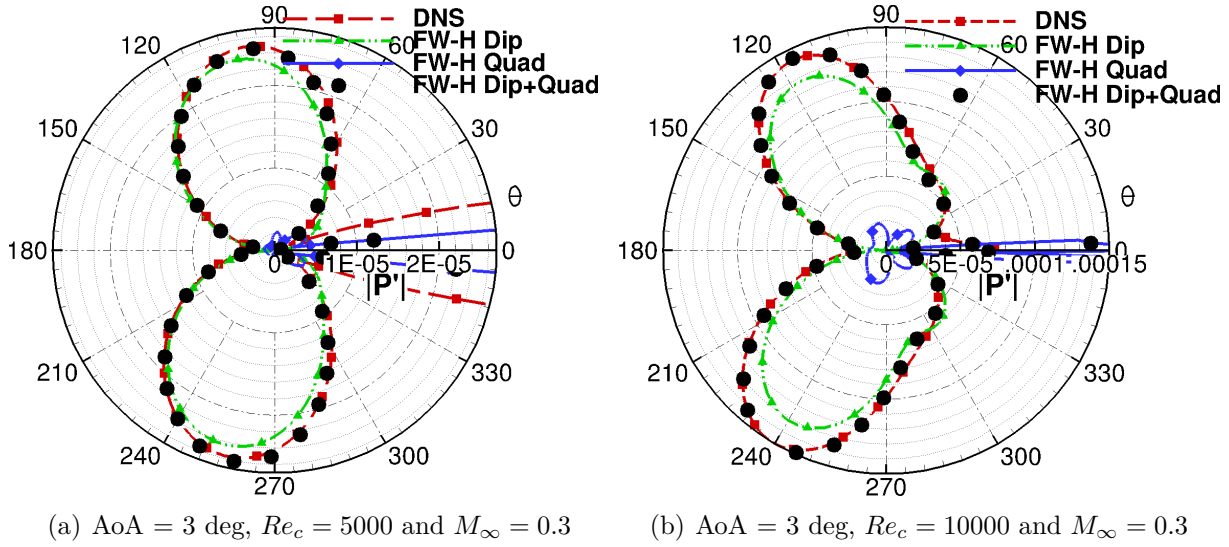


Figure 3.7: Dipole and quadrupole source contributions to total noise for an observer location at 5 chords from the airfoil, at vortex shedding frequency for (a) AoA = 3 deg, $Re_c = 5000$ and $M_\infty = 0.3$ and (b) AoA = 3 deg, $Re_c = 10000$ and $M_\infty = 0.3$.

increases as a function of the freestream Mach number. This incident field is given by the Lighthill stress terms, T_{ij} , and, for the present low Mach number flows, it can be computed by the flow Reynolds stresses. In the noise scattering process, the quadrupole field generates incident acoustic waves on the airfoil surface. The close proximity of these sources to the solid boundary generate a strong scattered field of dipolar nature along the airfoil trailing edge. This dipolar field radiates noise more efficiently than the incident quadrupolar field. Figures 3.8 (a) and (b) show a comparison in terms of magnitude of pressure fluctuations, $|p'|$, along the airfoil surface and far-field noise from the incident quadrupole sources at the vortex shedding frequency for $M_\infty = 0.3$, respectively. Here, a considerable increase in the pressure fluctuations along the surface can be observed for the higher Reynolds number flow at non-zero incidence. Similar trends are observed for the incident quadrupolar noise for the same flow configurations. In these figures, one can see that the highest values of pressure fluctuation appear close to the trailing edge. This effect occurs since the quadrupole sources are closer to this region and, therefore, the scattering mechanism is more pronounced.

3.3 Effects of Trailing Edge Bluntness on Noise Generation

To assess the influence of trailing edge bluntness on noise generation and propagation, hydrodynamic and acoustic properties are compared for two NACA 0012 airfoils with modified trailing edges. Surface 1 has a thinner trailing edge and surface 2 has a thicker trailing edge. In Figs. 3.9 (a) and (b), one can see mean flow streamlines for surfaces

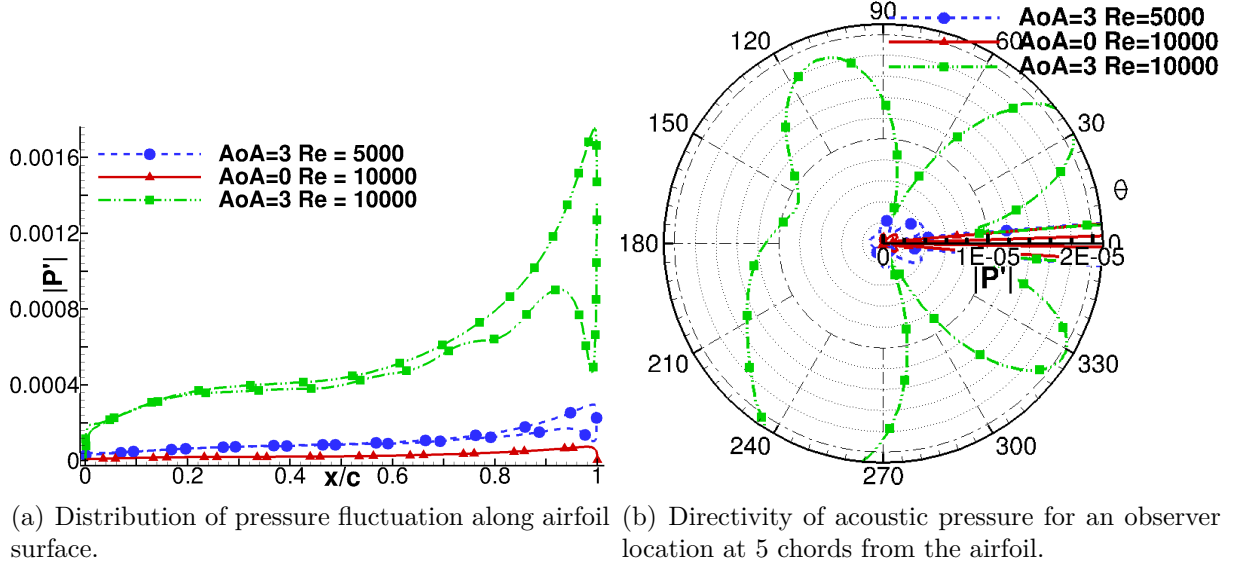


Figure 3.8: Comparison of (a) pressure fluctuations, $|p'|$, along airfoil surface and (b) far-field sound of incident quadrupolar field. Results are presented for surface 1 and $M_\infty = 0.3$ at vortex shedding frequency.

1 and 2, respectively, for $AoA = 3$ deg, $Re_c = 10000$ and $M_\infty = 0.3$. For the thinner trailing edge, a longer separation bubble is observed over the airfoil suction side while for the blunter trailing edge, a more compact separation bubble is observed behind the trailing edge, resembling that of a blunt body. Since different flow fields are observed for the trailing edge configurations analyzed, one should expect changes in the noise source distributions and, hence, in the acoustic far-field radiation.

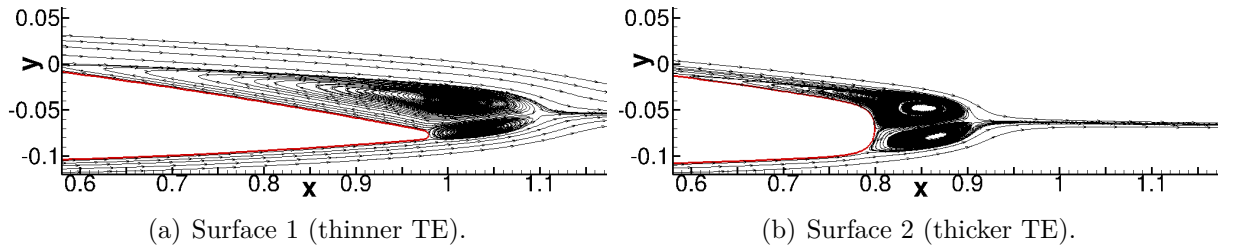


Figure 3.9: Mean flow streamlines along trailing edge region for $AoA = 3$ deg, $Re_c = 10000$, and $M_\infty = 0.3$.

Figure 3.10 presents snapshots showing contours of vorticity magnitude obtained for $AoA = 3$ deg, $Re_c = 10000$ and $M_\infty = 0.3$. In figure 3.10 (a), one can see vorticity for surface 1 and, in figure 3.10 (b), results are presented for surface 2. Here, one can observe that a thicker trailing edge leads to a higher vorticity intensity for similar Reynolds and freestream Mach numbers and angle of attack. It should be mentioned here that both figures are presented using the same levels of vorticity magnitude.

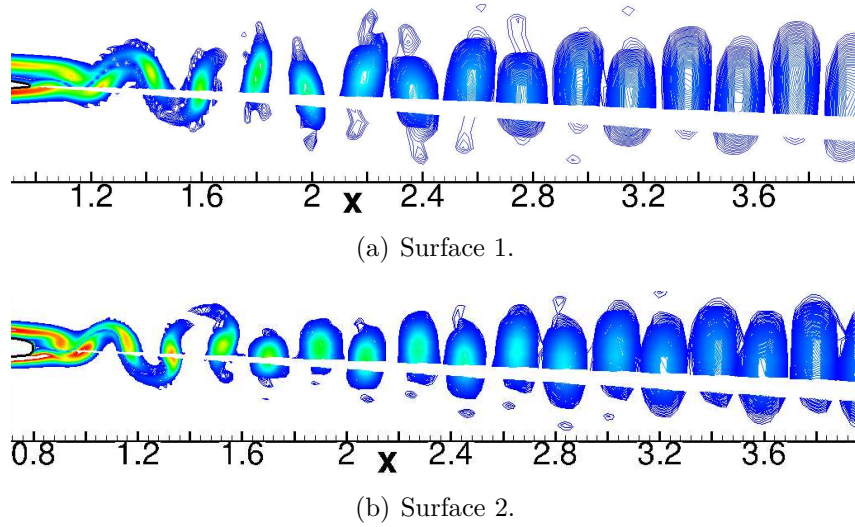


Figure 3.10: Snapshots showing contours of vorticity magnitude over the range $|\omega|=0$ to 10, obtained for $\text{AoA} = 3$ deg, $Re_c = 10000$, and $M_\infty = 0.3$.

Figure 3.11 (a) shows pressure spectra obtained for surfaces 1 and 2 for several freestream Mach numbers, $\text{AoA} = 3$ deg, and $Re_c = 10000$. As previously mentioned, for the present low Reynolds number, tonal noise occurs due to vortex shedding and, for each flow configuration, a main tone is observed followed by its harmonics. From this figure it is possible to see that pressure amplitudes of the individual tones are higher for the thicker trailing edge while the vortex shedding frequencies are higher for the thinner one. Similar results are reported in literature for experimental and numerical data (HUTCHESON AND BROOKS; TAM AND JU, 2004; 2011). Figure 3.11 (b) presents pressure directivities and figure 3.12 presents acoustic pressure contours for surfaces 1 and 2, at the vortex shedding frequency, the former, for observer locations at 5 chords from the airfoil for $\text{AoA} = 3$ deg, $Re_c = 10000$ and $M_\infty = 0.3$. One can observe that a blunter trailing edge generates higher noise levels for the current flow configuration. It is worth mentioning that these trends were found for all low Reynolds number cases studied, *i.e.*, the configurations with blunter trailing edges presented stronger noise radiation levels than the thinner ones, for similar flow configurations. This observation is a direct consequence of the stronger levels of vorticity magnitude observed in figure 3.10.

Figure 3.13 shows the dipole and quadrupole source contributions to far-field noise from surfaces 1 and 2, for $\text{AoA} = 3$ deg, $Re_c = 10000$ and $M_\infty = 0.3$, for observer locations at 5 chords from the airfoil. Here, dipole and quadrupole directivities resemble those of compact sources. However, one can observe a slightly stronger effect of quadrupole sources for surface 2. From this figure, one can also notice that directivities obtained by acoustic analogy are found to be in excellent agreement with DNS results.

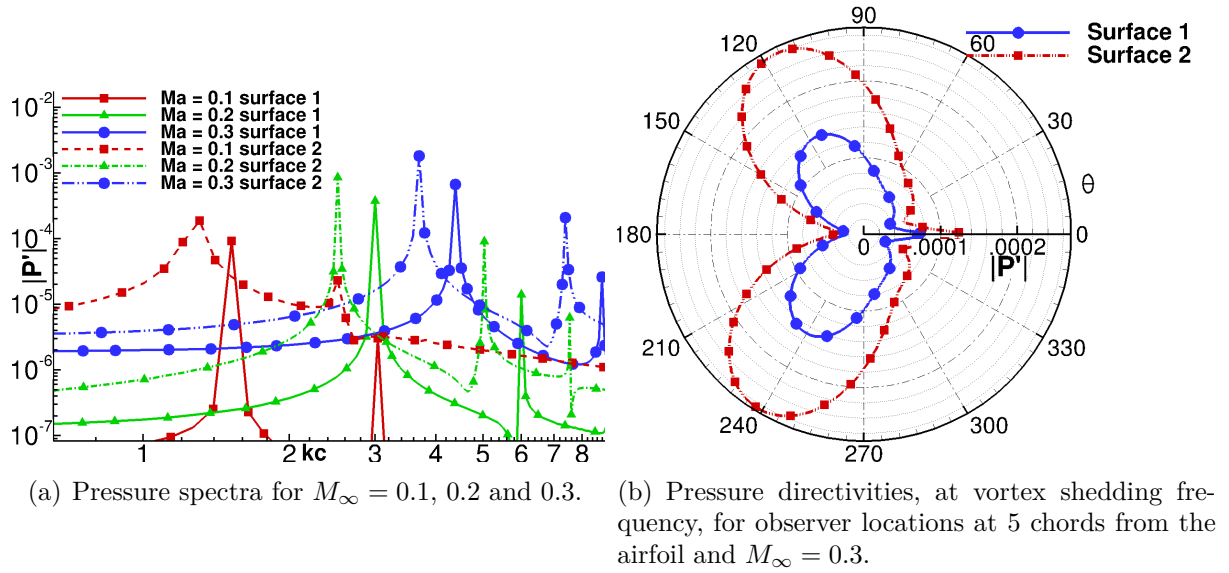


Figure 3.11: Comparison of acoustic predictions for surfaces 1 (thinner TE) and 2 (thicker TE) for $AoA = 3$ deg, and $Re_c = 10000$.

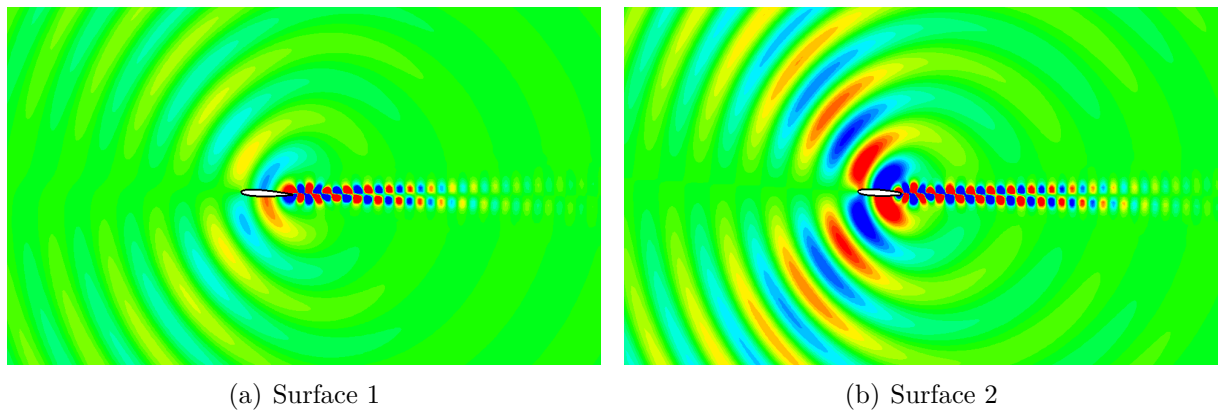


Figure 3.12: Comparison of acoustic pressure contours at vortex shedding frequency over the range $|p'| = \pm 5 \times 10^{-4}$ for $AoA = 3$ deg, $Re_c = 10000$, $M_\infty = 0.3$ and (a) surface 1, and (b) surface 2.

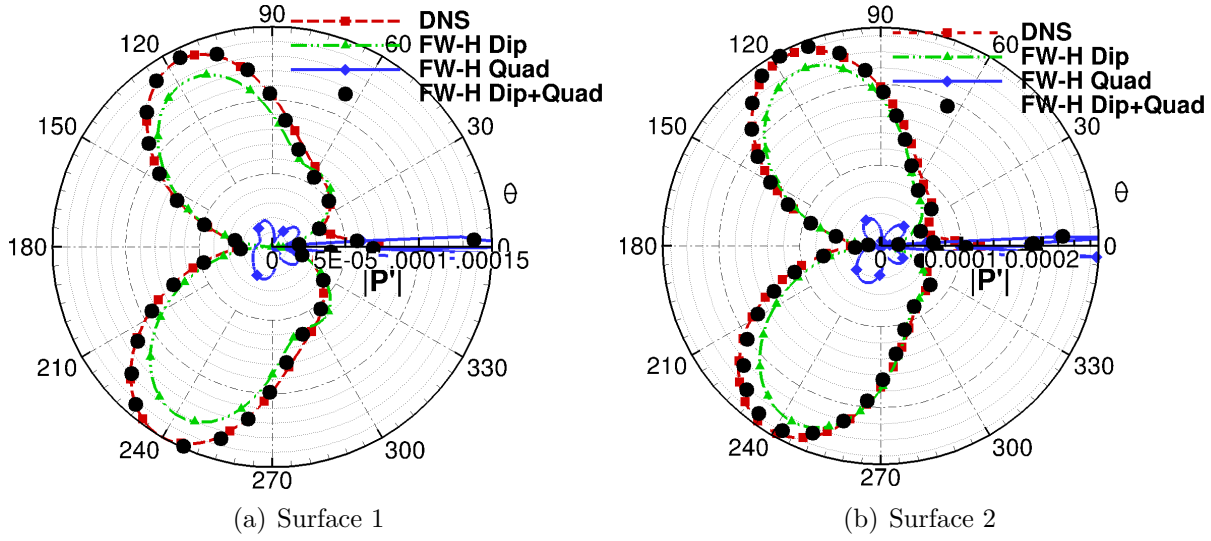


Figure 3.13: Dipole and quadrupole source contributions to total noise at $5c$ distant from the airfoil, at vortex shedding frequency for $\text{AoA} = 3^\circ$, $Re_c = 10000$, $M_\infty = 0.3$ and (a) surface 1 and (b) surface 2.

Since higher vorticity fluctuations occur for the blunter trailing edge configuration, we should expect higher levels in terms of Reynolds stresses along the airfoil wake. Figures 3.14 (a) to (f) present the spatial distributions of the quadrupole sources \hat{T}_{11} , \hat{T}_{12} , and \hat{T}_{22} , at the vortex shedding frequency, for $M_\infty = 0.2$. One should mention that, for the present flow configurations, the Lighthill stress terms T_{ij} are mainly composed of the Reynolds stress terms. Figures 3.14 (a) to (c) show results for the configuration with a thinner trailing edge (surface 1) and Figs. 3.14 (d) to (f) show results for the thicker trailing edge (surface 2). These plots are presented using the same contour levels and one can see that the magnitudes of the quadrupole sources are higher for the blunter trailing edge. Moreover, it is possible to visualize that the peak values of T_{ij} are closer to the airfoil surface for the surface with a thicker trailing edge. For low and moderate Mach numbers, the acoustic far-field should be dominated by a dipolar radiation pattern due to the scattering of the quadrupolar incident field along the airfoil trailing edge. Since the quadrupoles are closer to the solid surface for the blunter trailing edge, one should expect a stronger dipolar radiation for this configuration due to a more pronounced acoustic scattering.

In the present work, the FWH analogy is one of the techniques used to predict the far-field noise generated by the airfoils. This methodology allows a separation of the effects of the individual noise sources (dipoles and quadrupoles). Here, a solid FWH surface is applied and, therefore, the scattered field should be solely constructed using the pressure fluctuations along the airfoil surface. Thus, one can quantify the intensity of the scattered acoustic field by a measure of this quantity, which is shown in figure 3.15 (a) for the

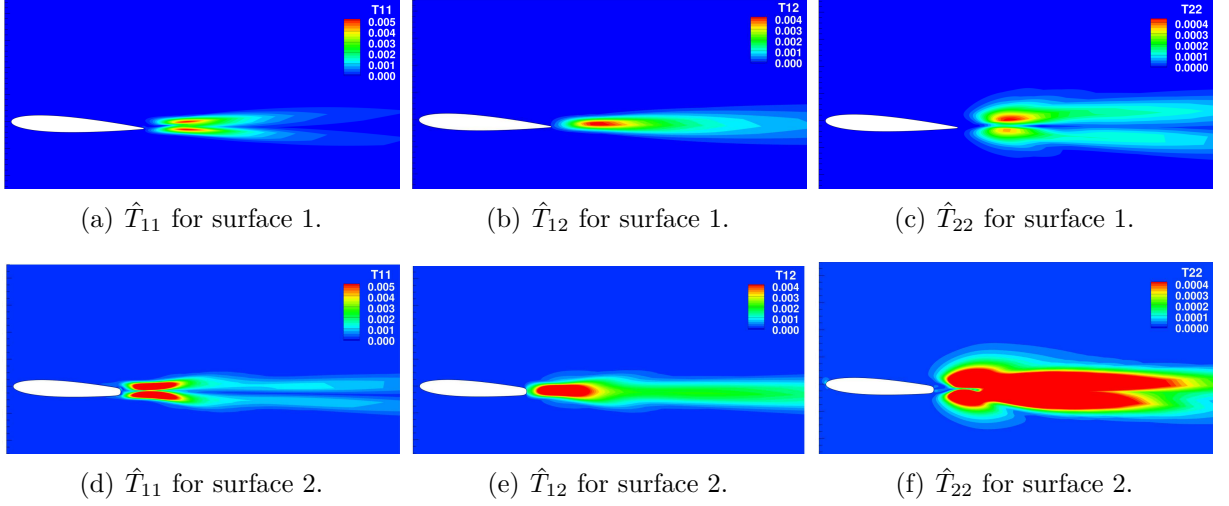


Figure 3.14: Contours of magnitude of quadrupole sources for $\text{AoA} = 3^\circ$, $Re_c = 5000$, and $M_\infty = 0.2$. Contours go over the following ranges $\hat{T}_{11}=0$ to 0.005, $\hat{T}_{12}=0$ to 0.004 and $\hat{T}_{22}=0$ to 0.0004

vortex shedding frequency. Firstly, it is possible to see that pressure values are larger at the trailing edge, confirming its efficiency as a noise generation mechanism. These values of acoustic pressure represent the intensity of the dipole sources along the airfoil and one can conclude that the trailing edge acts as a powerful sound source. As previously commented, if one considers the quadrupole sources as responsible by the incident sound field and the airfoil surface as the sound scatterer, it can be concluded that a closer proximity of the former will increase the noise scattering by the latter (with a $1/\sqrt{r^5}$ algebraic sense for a two-dimensional problem; in a three-dimensional field, the algebraic form should be $1/r^3$). Here, r is the distance between the quadrupole source and the solid surface.

Larger magnitudes of the incident quadrupolar field will also increase noise scattering. Figure 3.15 (b) presents the magnitude of acoustic radiation from the quadrupole sources only, for an observer location at $5c$ distant from the airfoil. These results are obtained solving the volume integral appearing in the FWH formulation for the vortex shedding frequency. As one can observe in this figure, the thick trailing edge airfoil generates a higher acoustic field for its quadrupole source compared with the thinner trailing edge airfoil.

3.4 Effects of Trailing Edge Suction & Blowing on Noise Generation

In order to investigate possibilities for noise reduction, steady suction and blowing are performed along the blunt trailing edges analyzed (see figure 1.4 for a visualization of the regions where suction and blowing are applied). Since, at low Reynolds numbers, trailing

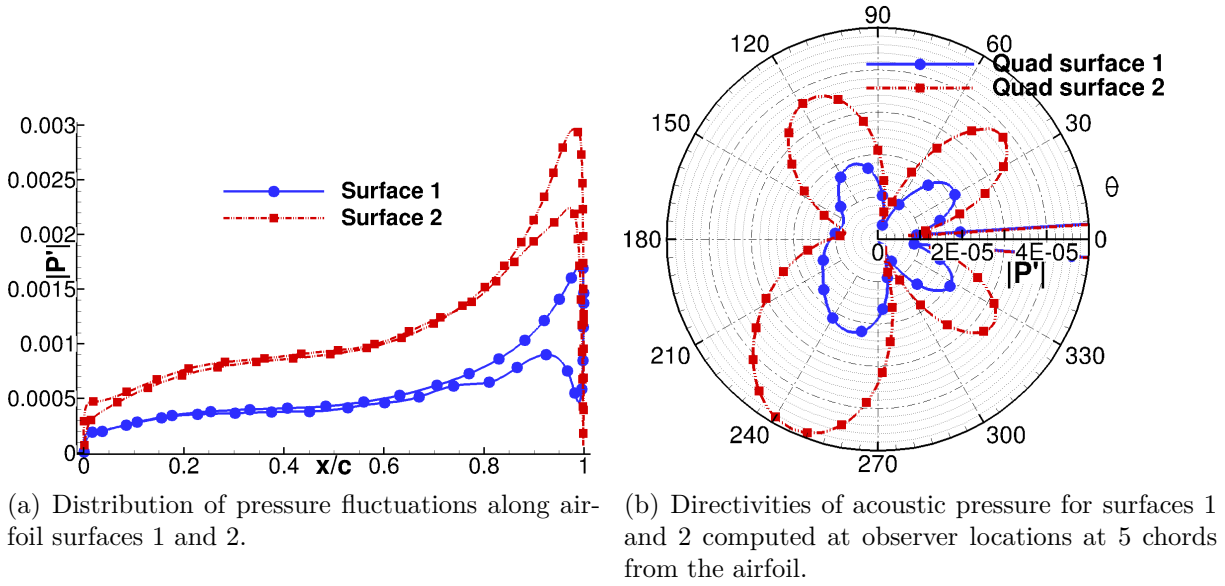


Figure 3.15: Comparison of (a) pressure fluctuations, $|p'|$, along airfoil surface and (b) far-field sound of incident quadrupolar field. Results are presented for $\text{AoA} = 3^\circ$, $Re_c = 10000$, and $M_\infty = 0.3$, at vortex shedding frequency.

edge noise occurs due to vortex shedding, it is expected that disturbing the flow near the trailing edge will impact the hydrodynamics of the shedding and, therefore, its subsequent noise generation. Blowing and suction are employed with no time variations since these would introduce an additional noise source.

Figure 3.16 presents plots of pressure spectra (in linear \times log scale) for surfaces 1 and 2 measured at $1/4$ of chord perpendicular to the trailing edge. In these plots, one can see comparisons of acoustic pressure for the baseline configuration and for the cases where suction and blowing is employed on the trailing edge. Results for which blowing is applied are presented in Figs. 3.16 (a) and (c) for $M_\infty = 0.3$ and surfaces 1 and 2, respectively. For both cases, blowing velocities are set as 5% and 10% of the freestream velocity. As one can observe, blowing considerably reduces the near and far-field noise (see figure 3.19), and this noise reduction depends on the blowing velocity and trailing edge bluntness. It is possible to see that a more effective noise reduction appears for the blunter trailing edge. On the other hand, Figs. 3.16 (b) and (d) present plots of pressure spectra for the cases where suction is applied along the trailing edges of surfaces 1 and 2, respectively. It turns out that suction has the opposite effect of blowing, increasing far-field noise radiation. Similar trends are observed for all freestream Mach numbers and Reynolds numbers investigated.

Figures 3.17 (a) and (b) show the mean flow streamlines for surface 1 ($\text{AoA} = 3^\circ$, $Re_c = 5000$, $M_\infty = 0.3$) for baseline configuration (no blowing) and for 10% of freestream Mach number blowing intensity, respectively. From this figure, it is possible to see that

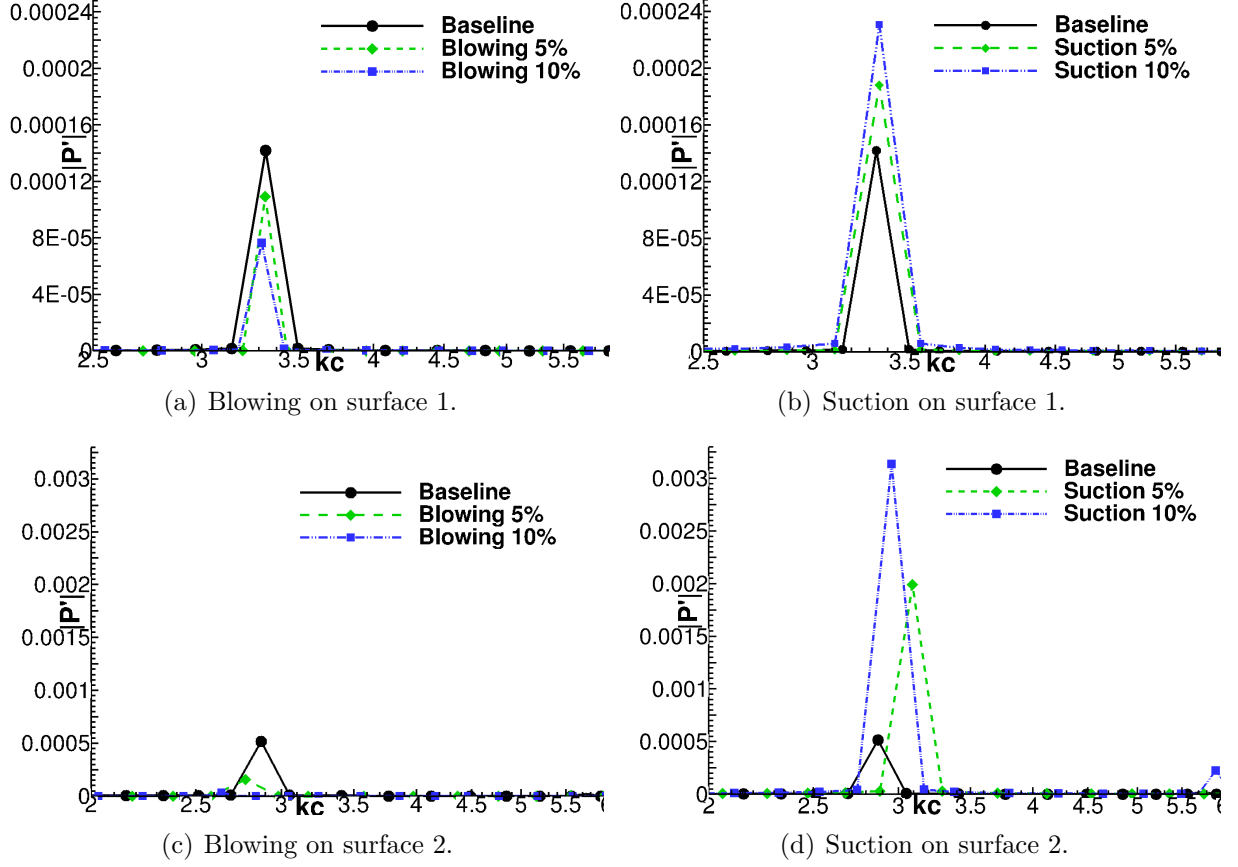


Figure 3.16: Comparison of the effects of suction and blowing on acoustic pressure spectrum for NACA 0012 at AoA = 3 deg, $Re_c = 5000$ and $M_\infty = 0.3$.

very slight modifications in the mean flowfield are observed. One should remind that blowing is applied only along the rounded region of the trailing edge which consists of a very tiny portion of surface 1. Figures 3.17 (c) and (d) present mean flow streamlines for surface 2, for the same flow conditions. Results are shown for the baseline case and for 10% blowing, respectively. Here, one can observe more prominent modifications in the mean flowfield. One can see that the recirculation bubble is moved downstream the trailing edge and its size is considerably reduced compared to the baseline configuration.

Figures 3.18 (a) and (b) present a comparison of the instantaneous airfoil vortex shedding structures, for surface 2, Baseline configuration (no blowing) and with 10% blowing, respectively. One can observe that when blowing is applied, vortex formation moves downstream. Moreover, blowing causes a reduction in the vorticity magnitude.

Figure 3.19 presents a comparison of the effects of trailing edge blowing on acoustic pressure. Contours of pressure fluctuations amplitude are plotted at vortex shedding frequency over the range $|p'| = \pm 5 \times 10^{-5}$ for surface 2 AoA = 3 deg, $Re_c = 5000$, $M_\infty = 0.3$ and (a) baseline configuration (no blowing), and (b) with blowing. Here, one can realize that although the wake remains almost the same in magnitude, the noise scattered into the far-field is virtually removed, being barely perceptible in figure 3.12 (b). Figure 3.20

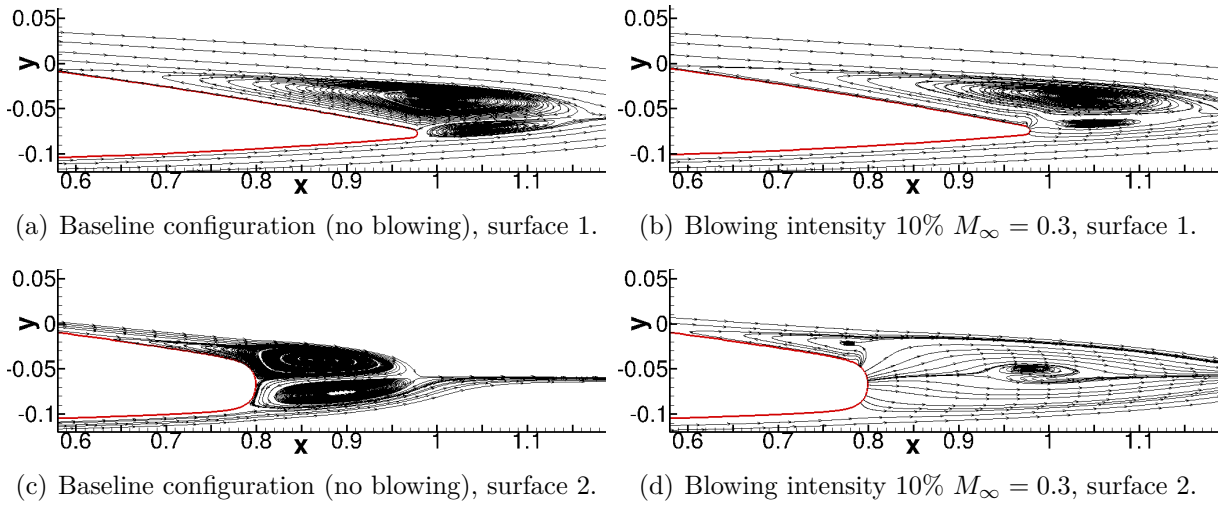


Figure 3.17: Comparison of blowing effects on mean flow streamlines at trailing edge region for $\text{AoA} = 3^\circ$, $Re_c = 5000$ and $M_\infty = 0.3$.

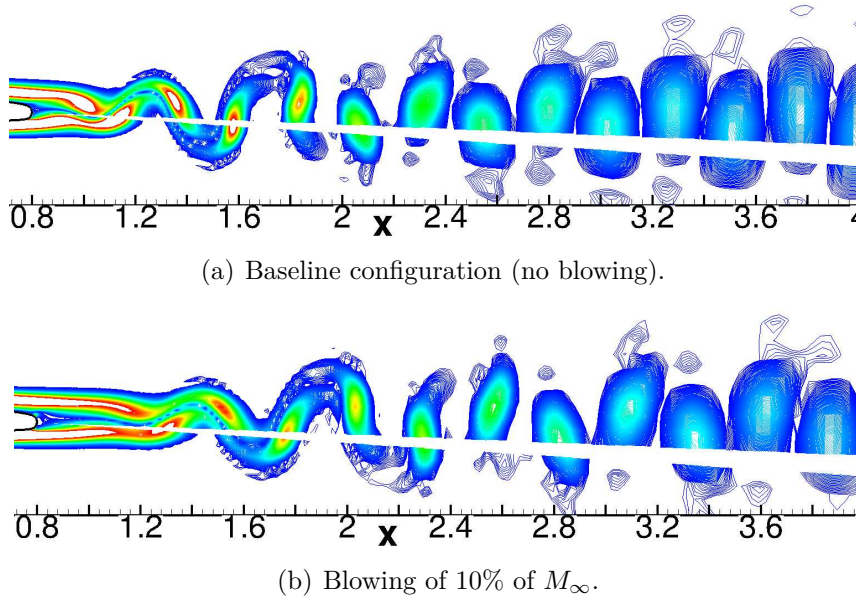


Figure 3.18: Snapshots showing contours of vorticity magnitude over the range $|\omega|=0$ to 5, obtained for NACA 0012 with trailing edge surface 2 for $\text{AoA} = 3^\circ$, $Re_c = 5000$ and $M_\infty = 0.3$.

shows the dipole and quadrupole source contributions to far-field noise from surface 2, for $\text{AoA} = 3^\circ$, $Re_c = 5000$, $M_\infty = 0.3$, and (a) baseline configuration (no blowing) and (b) with blowing 10%, for observer locations at 5 chords from the airfoil. Here, it is possible to see that the quadrupole noise for the blowing case is similar to the previous case baseline configuration (no blowing). However, the dipole noise is reduced to the same level as that of the quadrupole noise. The FWH analogy is also used here to verify the accuracy of the numerical procedure and one can see that DNS results show excellent agreement to acoustic analogy, validating the current implementation. In Figs. 3.21 (a) and (b), it is

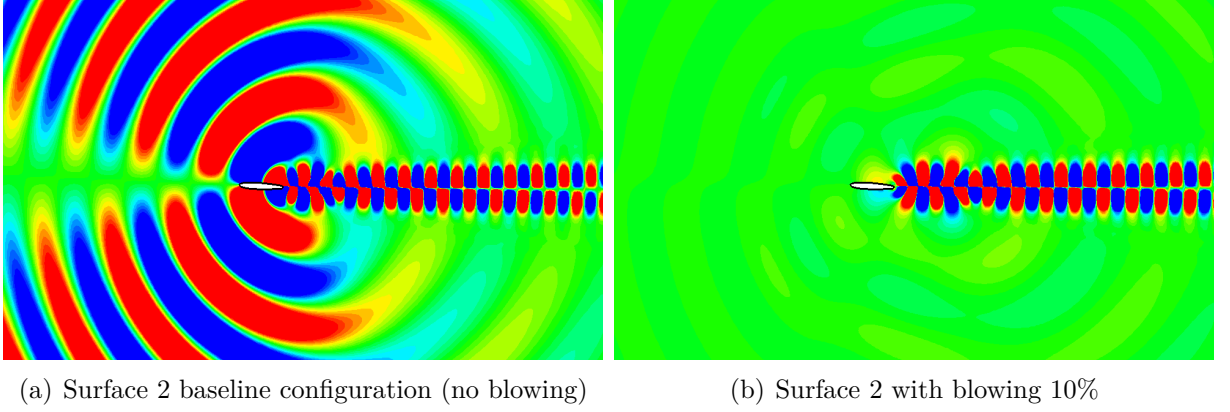


Figure 3.19: Comparison of acoustic pressure contours at vortex shedding frequency over the range $|p'| = \pm 5 \times 10^{-5}$ for surface 2 $\text{AoA} = 3^\circ$, $Re_c = 5000$, $M_\infty = 0.3$ and (a) baseline configuration (no blowing), and (b) with blowing.

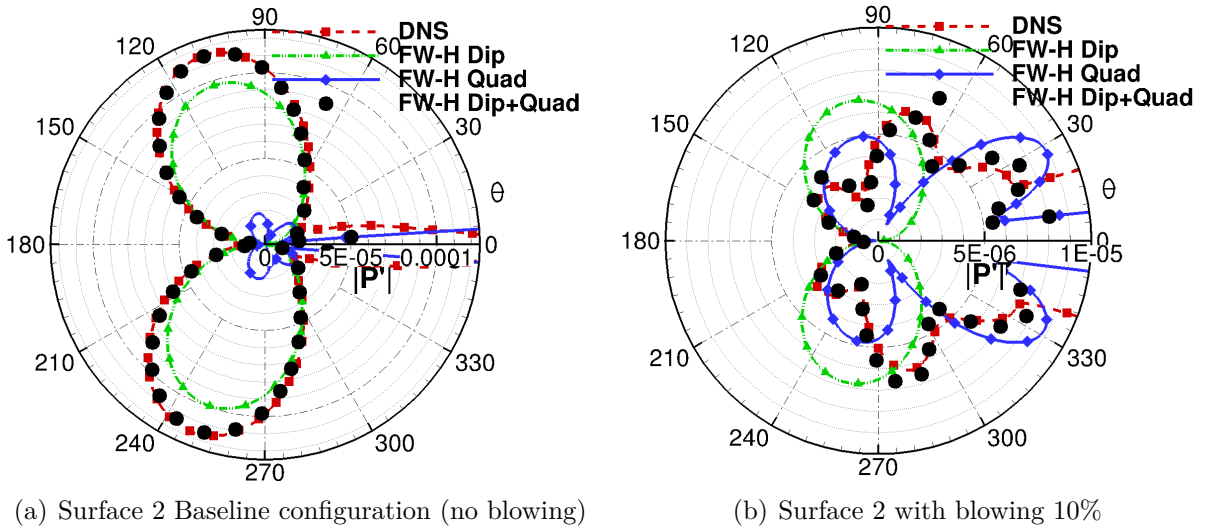


Figure 3.20: Dipole and quadrupole source contributions to total noise at $5c$ distant from the airfoil, at vortex shedding frequency for surface 2 $\text{AoA} = 3^\circ$, $Re_c = 5000$, $M_\infty = 0.3$ and (a) Baseline configuration (no blowing), and (b) with blowing 10%.

possible to see the effects of trailing edge blowing on the incident quadrupolar field for surface 1 at $\text{AoA} = 3^\circ$, $Re_c = 5000$ and $M_\infty = 0.3$. When blowing is applied, a small

reduction in the contour levels is observed and the peak values move downstream. A more significant change can be visualized in the plots of pressure fluctuations along the airfoil surface and in the pressure directivity plots shown in Figs 3.22 (a) and (b), for the vortex shedding frequency. As it can be seen, surface pressure fluctuations are reduced due to trailing edge blowing and, hence, far-field acoustic radiation also diminishes considerably. Figure 3.23 presents the effects of blowing applied on surface 2 for $\text{AoA} = 3^\circ$,

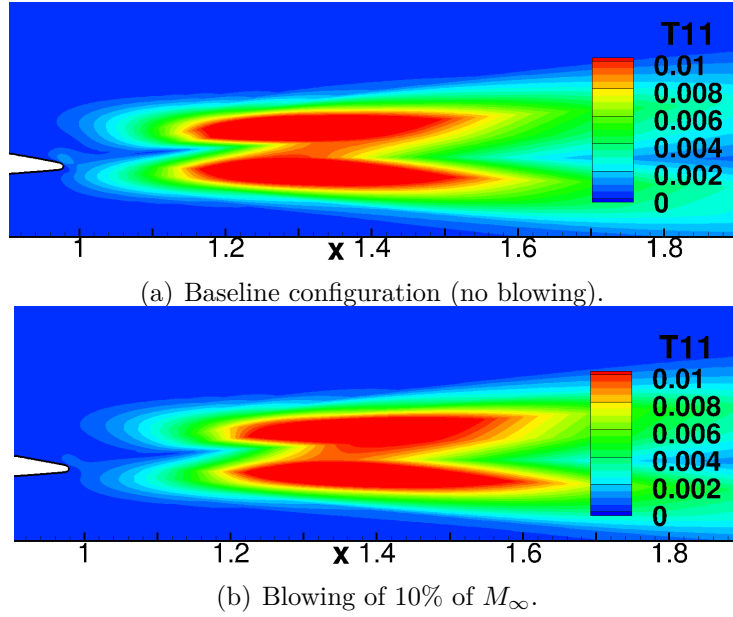


Figure 3.21: Magnitude of quadrupole sources over the range of $\hat{T}_{11} = 0$ to 0.016, for surface 1 and $\text{AoA} = 3^\circ$, $Re_c = 5000$ and $M_\infty = 0.3$. Results shown for vortex shedding frequency.

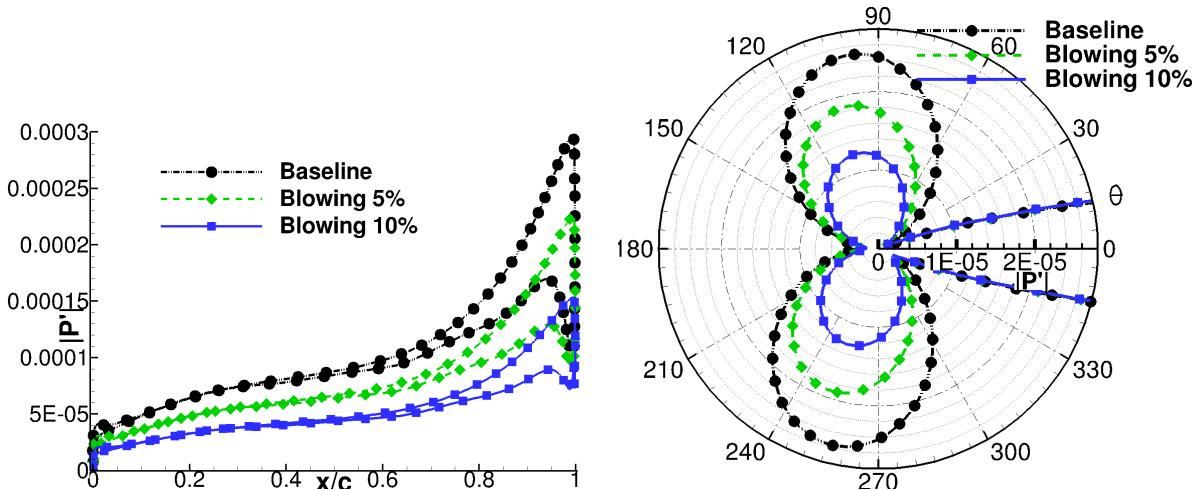


Figure 3.22: Comparison of the effects of blowing on pressure fluctuations along airfoil and far-field sound for surface 1. Results are presented for $\text{AoA} = 3^\circ$, $Re_c = 5000$ and $M_\infty = 0.3$ at vortex shedding frequency.

$Re_c = 5000$ and $M_\infty = 0.3$. It is possible to see that blowing has a stronger effect on the

quadrupolar field for a thicker trailing edge comparing figure 3.23 to 3.21. In the present case, peak values are significantly moved downstream when blowing is applied which is a result of the modified vortex shedding structure observed in figure 3.18. A dramatic change can be visualized in the plots of pressure fluctuations along the airfoil surface and in the directivity plots shown in Figs. 3.24 (a) and (b), for the vortex shedding frequency. Results presented in these figures are obtained for the same flow configuration as that from figure 3.23. One can observe that surface pressure fluctuations are considerably reduced due to trailing edge blowing and, hence, acoustic scattering diminishes at a similar rate. With this, one can conclude that steady trailing edge blowing can be implemented for noise reduction of airfoil vortex shedding tonal noise at low Reynolds number flows. In this case, blowing is more efficient in noise reduction for blunter trailing edges, such as those found in cross-bar sections installed in automobiles.

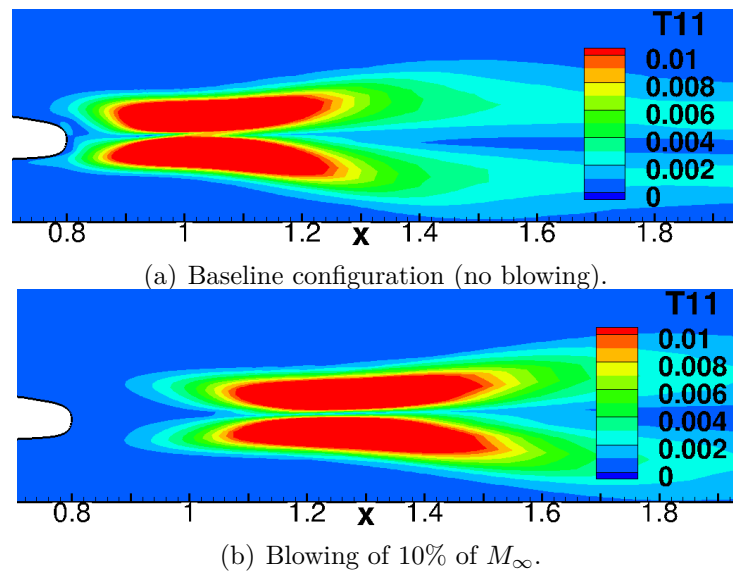


Figure 3.23: Magnitude of quadrupole sources over the range of $\hat{T}_{11} = 0$ to 0.01, for surface 2 and $AoA = 3$ deg, $Re_c = 5000$ and $M_\infty = 0.3$. Results shown for vortex shedding frequency.

Table 3.2 shows the effects of trailing edge bluntness, suction & blowing at trailing edge on the overall sound pressure level (OASPL) at low Reynolds numbers. In this table, results are shown in terms of $\Delta OASPL$ compared to a baseline case, which appears as case 1. The overall sound pressure level is the measured quantity which eventually would be the main concern in terms of noise generation for aircraft and wind energy companies, and regulating agencies (WOLF *et. al*, 2013). Regarding the effects of trailing edge bluntness, one can observe that the thicker trailing edge produces more noise than the thinner one. Likewise, when the suction intensity increases, an increasing in the OASPL is observed. The opposite effect is observed for blowing; as the blowing intensity increases, the noise produce is reduced. It is possible to observe that a more effective noise reduction appears

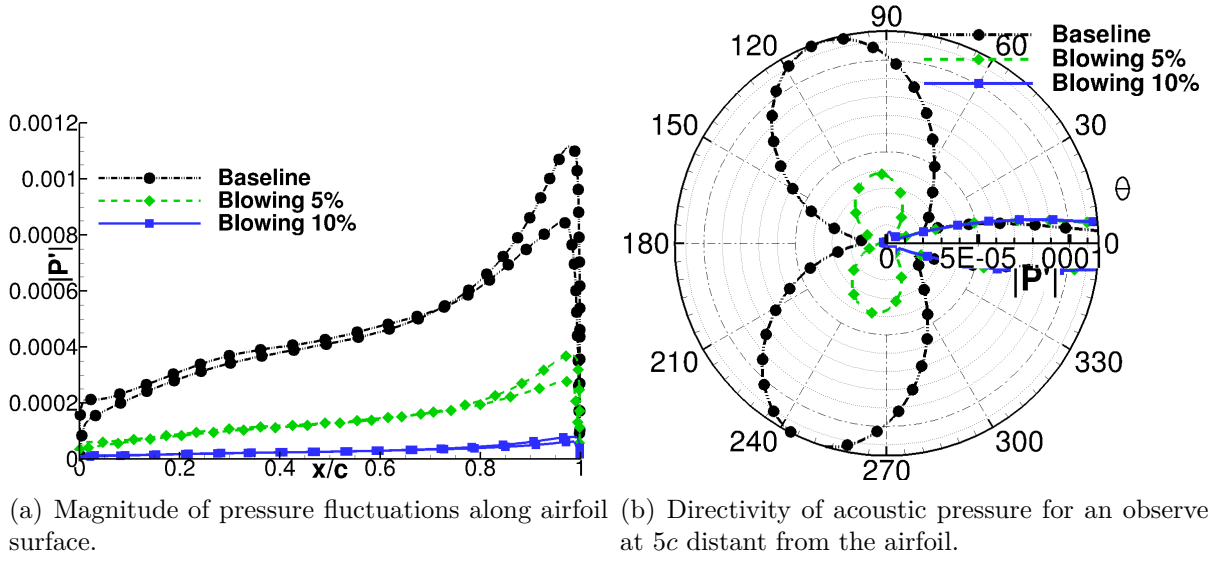


Figure 3.24: Comparison of the effects of blowing on pressure fluctuations along airfoil and far-field sound for surface 2. Results are presented for $\text{AoA} = 3^\circ$, $Re_c = 5000$ and $M_\infty = 0.3$ at vortex shedding frequency.

for the thicker trailing edge, when blowing is applied.

Table 3.2: Overall sound pressure level for low Reynolds number cases.

Case	Airfoil	AoA	Re_c	M_∞	Suction	Blowing	ΔOASPL (dB)
1	Surface 1	3 deg.	5000	0.3	—	—	0.00
2	Surface 1	3 deg.	5000	0.3	5% & 10%	—	+5.53 & +8.61
3	Surface 1	3 deg.	5000	0.3	—	5% & 10%	−6.96 & −10.65
4	Surface 2	3 deg.	5000	0.3	—	—	+19.68
5	Surface 2	3 deg.	5000	0.3	5% & 10%	—	+24.11 & +32.59
6	Surface 2	3 deg.	5000	0.3	—	5% & 10%	+7.03 & −21.44

4 AIRFOIL NOISE PREDICTIONS AT MODERATE REYNOLDS NUMBERS

4.1 Introduction

This section discusses results of direct numerical simulations and acoustic analogy for moderate Reynolds number flows past a NACA 0012 airfoil. The flow configurations studied are described in table 4.1. Here, as previously shown in chapter 3, to display the trends and findings, results are separated in several sections in order to evaluate the effect of compressibility, the effect of bluntness, and the effects of suction & blowing at trailing edge on noise generation and propagation processes. In addition, this chapter presents the effects of angle of incidence separately. Within each section, the Reynolds number based on airfoil chord is varied between $Re_c = 50000$ and 100000 with the aim to observe the influence of this parameter with respect to noise generation and propagation.

Table 4.1: Studied cases for moderate Reynolds number flows.

Airfoil	AoA	Re_c	M_∞	% Suction	% Blowing
Surface 1	0 deg.	50000	0.1, 0.2 and 0.3	–	–
Surface 2	0 deg.	50000	0.1, 0.2 and 0.3	–	–
Surface 1	3 deg.	50000	0.1, 0.2 and 0.3	–	–
Surface 2	3 deg.	50000	0.1, 0.2 and 0.3	–	–
Surface 1	0 deg.	100000	0.1, 0.2 and 0.3	–	–
Surface 2	0 deg.	100000	0.1, 0.2 and 0.3	–	–
Surface 1	3 deg.	100000	0.1, 0.2 and 0.3	–	–
Surface 2	3 deg.	100000	0.1, 0.2 and 0.3	–	–
Surface 1	0 deg.	100000	0.1 and 0.3	5% of M_∞	–
Surface 1	0 deg.	100000	0.1 and 0.3	–	5% of M_∞
Surface 1	3 deg.	100000	0.1 and 0.3	5% of M_∞	–
Surface 1	3 deg.	100000	0.1 and 0.3	–	5% of M_∞
Surface 2	0 deg.	100000	0.1 and 0.3	10% of M_∞	–
Surface 2	3 deg.	100000	0.1 and 0.3	10% of M_∞	–

4.2 Effects of Compressibility on Noise Generation

To detail the influence of compressibility on noise generation and propagation, hydrodynamic and acoustic properties for cases of surface 1 (thinner trailing edge airfoil) with zero angle of incidence and different freestream Mach number are analyzed and compared. Figures 4.1 (a) and (b) present an enlarged view of the time-averaged flow streamlines along the trailing edge region for surface 1 with $AoA = 0$ deg. and $Re_c = 50000$, show-

ing the development of recirculation bubbles for $M_\infty = 0.1$ and 0.3 , respectively. For both Mach numbers, only a small symmetric recirculation bubble is observed along the trailing edge. One can notice also, that flow separation occurs further upstream for the higher freestream Mach number and, therefore, the recirculation bubble becomes slightly thicker and more elongated. This separation bubble appears due to the finite thickness of the trailing edge and the behavior found for the referenced case is similar to that of the $Re_c = 10000$ and zero incidence in section 3.

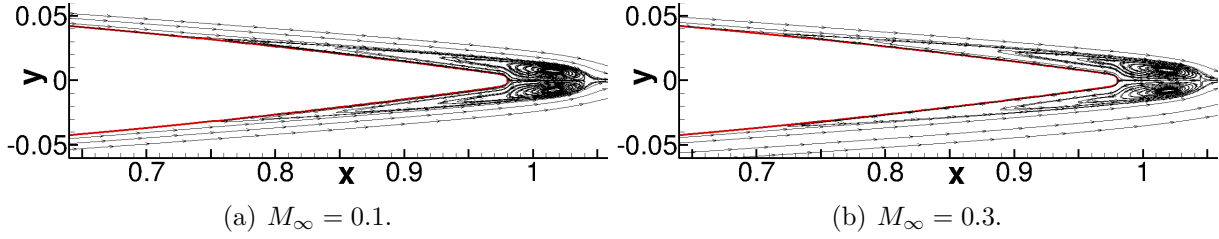


Figure 4.1: Mean flow streamlines at trailing edge region for surface 1, AoA = 0 deg. and $Re_c = 50000$.

When the Reynolds number based on airfoil chord is increased to $Re_c = 100000$, while keeping the zero incidence, a different behavior is observed as the Mach number is increased. Figure 4.2 shows an enlarged view of the mean flow streamlines at the trailing edge region for the surface 1 (thinner trailing edge airfoil) AoA = 0 deg, $Re_c = 100000$, $M_\infty = 0.1$ and 0.3 . For the former case, (see fig4.2 (a)), the mean flow is symmetric and only a small recirculation bubble is noticed close to the trailing edge. However, for the $M_\infty = 0.3$ case, stronger instabilities along the boundary layer are developed and the upper surface of the airfoil presents a separation bubble, causing the flow to be non-symmetric.

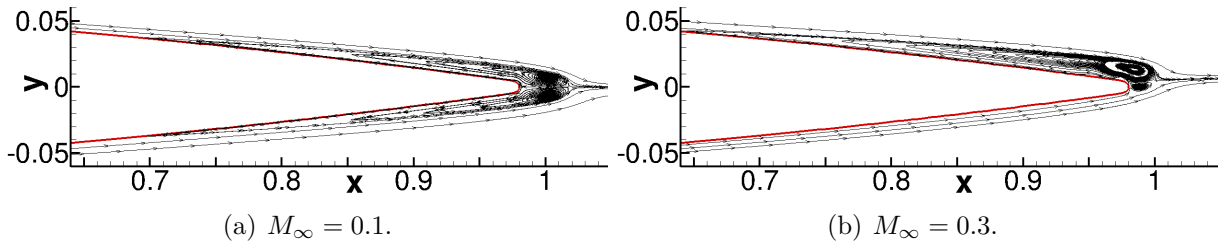


Figure 4.2: Mean flow streamlines at trailing edge region for surface 1, AoA = 0 deg. $Re_c = 100000$.

To further examine the latter behavior, snapshots showing flow streamlines, and contour of vorticity over the range $\omega = \pm 35$ for surface 1, with zero incidence, $Re_c = 100000$, and $M_\infty = 0.3$ are depicted in figures 4.3 (a) to (h). The sequences show that the boundary layer separation starts at $x/c = 0.60$ in suction side of airfoil, then the laminar separation bubble (LSB) rolls-up, developing a separated shear layer vortex. Following its

formation, this two-dimensional roller convects downstream and ultimately is shed just upstream the airfoil trailing edge. This structure observed along the trailing edge are a two-dimensional representation of the three dimensional spanwise “rollers” phenomenon found in experimental studies of (KIRK, 2014) and (PLOGMANN *et. al*, 2013), and similar to those found in two-dimensional numerical studies of (JONES AND SANDBERG, 2010) and (DESQUESNES *et. al*, 2007). Snapshots of flow streamlines in figure 4.3 show the development laminar separation bubbles in pressure side, however, these structures are smaller and more flattener than the ones found in the suction side.

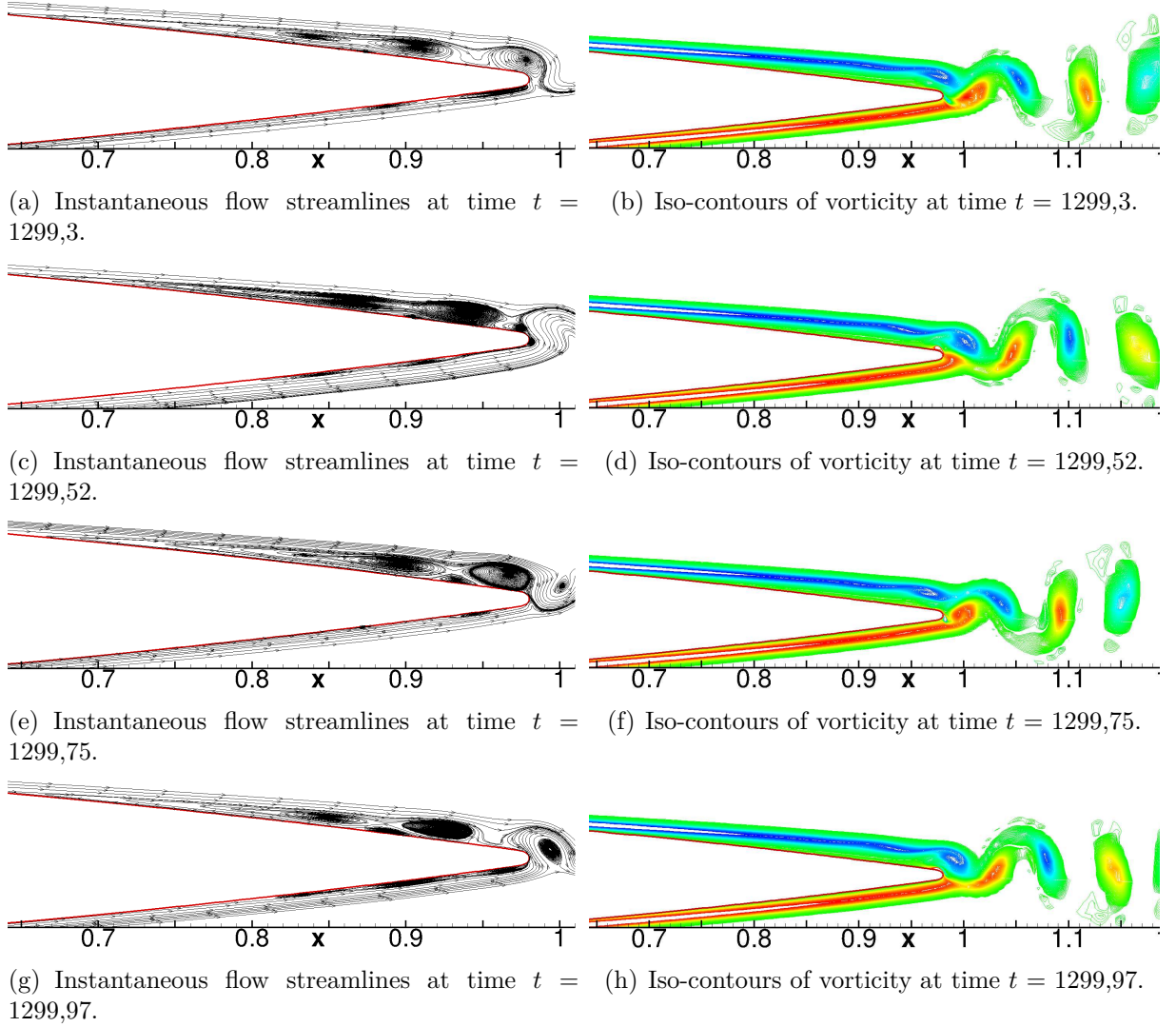


Figure 4.3: Snapshots of flow streamlines (left) and iso-contours of instantaneous vorticity over the range $\omega = \pm 35$ (right) along the trailing edge for surface 1 AoA = 0 deg. $Re_c = 100000$ and $M_\infty = 0.3$.

To examine the hydrodynamic behavior during the transition from $M_\infty = 0.1$ to $M_\infty = 0.3$, the effects of compressibility and disturbances over the boundary layer are evaluate at moderate Reynolds numbers. Two numerical simulations are conducted for the same flow configuration at AoA = 0 deg, $Re_c = 100000$ and an intermediate Mach number of

$M_\infty = 0.2$, with the exception that one of these includes a temporary disturbance. Here the boundary layers are tripped on both sides of the airfoil by blowing over the region $0.2 < x/c < 0.3$, with a magnitude of $10\%M_\infty$ during an instant in time. Figures 4.4 (a) and (b) present the time-averaged flow streamlines for the mentioned case without and with a temporary disturbance, respectively. One can clearly observe that, for this Mach number, without any external disturbance, the mean flow is still symmetric but unlike $M_\infty = 0.1$ case, one can observe recirculation regions downstream of the trailing edge and also slightly upstream. These regions could potentially amplify acoustic perturbations in the boundary layer which appear due to an acoustic feedback loop. When the temporary disturbance is applied, the flow becomes non-symmetric as shown in Fig. 4.4 (b), developing stronger and larger structures within the shear layer on the pressure side of airfoil.

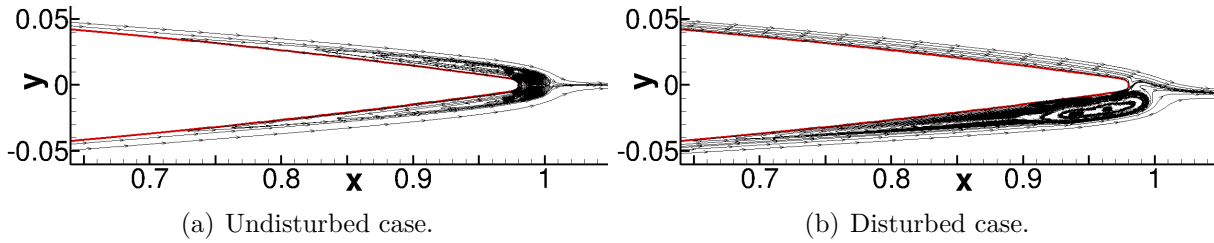


Figure 4.4: Mean flow streamlines at trailing edge region for surface 1, AoA = 0 deg. $Re_c = 100000$ and $M_\infty = 0.2$.

Figures 4.5 and 4.6 compare the undisturbed and disturbed cases, snapshots of flow streamlines and vorticity for the undisturbed and disturbed cases. The sequences for the case with no disturbance in fig. 4.5 and fig. 4.6 show here that boundary layer separation starts further downstream at $x/c = 0.73$, then the laminar separation bubble (LSB) rolls-up, developing a more flattened and elongated shear layer vortex on both sides of airfoil. Following, this two-dimensional roller convects downstream and ultimately is shed just upstream the airfoil trailing edge. The sequences of vorticity for the same case in fig 4.6 shows the symmetric vortex shedding structures just downstream the trailing edge.

A different behavior is found after the boundary layers are tripped on both sides of the airfoil by blowing. In figs. 4.5 and 4.6, the sequences of snapshots for the disturbed case show that the boundary layer separation starts further upstream at $x/c = 0.63$ on lower side, triggering the formation of stronger and larger separation bubbles, later, this laminar separation bubble rolls-up developing a more larger and stronger shear layer vortex just on the lower sides of airfoil. this vortex are then convected and shed right up the trailing edge as can be seen in figure 4.6 (f). Meanwhile the boundary layer detachment in upper side of airfoil is barely perceptible at some instances, and the vortex shedding occurs downstream the trailing edge.

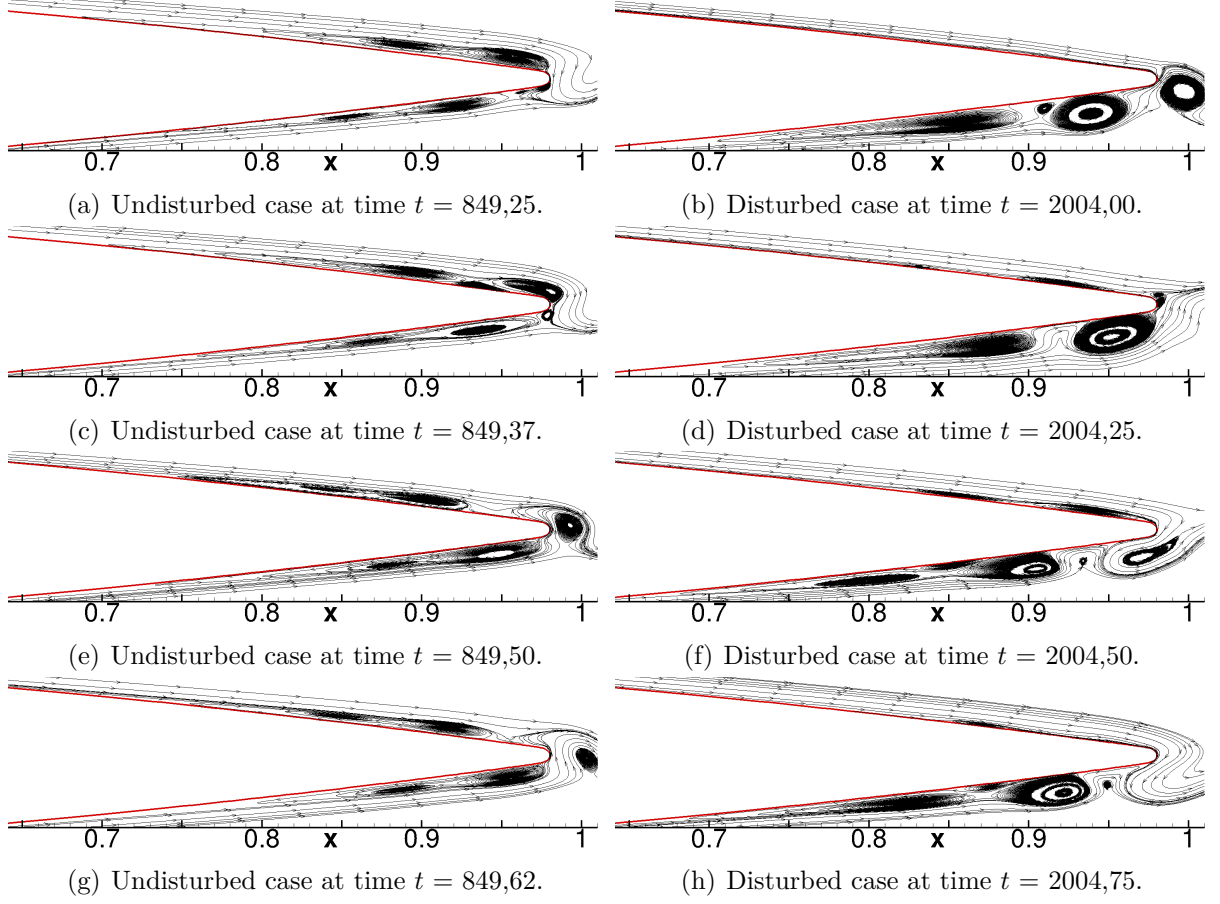


Figure 4.5: Snapshots of flow streamlines at trailing edge region for surface 1 AoA = 0 deg, $Re_c = 100000$ and $M_\infty = 0.2$.

As shown above, results demonstrated that compressibility, and Reynolds number effects cause a significant impact in terms of hydrodynamic properties. It is expected that these flow variations have a further impact on acoustic quantities. Figure 4.7 (a) depicts the near-field pressure spectra measured at a quarter of chord distant perpendicularly from the trailing edge for surface 1 AoA = 0 deg, and $Re_c = 50000$. As mentioned before, the spectra of non-dimensional acoustic pressure are presented as a function of Helmholtz number $kc=2\pi fc$, where k is the acoustic wavenumber, f is the non-dimensional frequency and c is the non-dimensional airfoil chord. Non-dimensional quantities are obtained in the same way discussed in Chapter 2. For the flow configurations analyzed, it is possible to observe the presence of a main tonal peak and its harmonics, being the vortex shedding the main noise generation mechanism. In this case, the main tonal peaks observed in Fig. 4.7 (a) occur at the vortex shedding frequency and hydrodynamic variations in the flows are responsible for the modifications observed in the plots of spectra. Table 4.2 details the main non-dimensional frequency $k_s c$ and the main non-dimensional acoustic amplitude $|p'_s|$ of the spectra shown in figure 4.7 (a). The main non-dimensional frequency is represented as a function of Helmholtz number $k_s c = 2\pi f_s c$, where f_s corresponds to the frequency of the dominant peak of the spectrum (having the highest acoustic amplitude). The main non-dimensional acoustic amplitude $|p'_s|$ corresponds to the amplitude of the

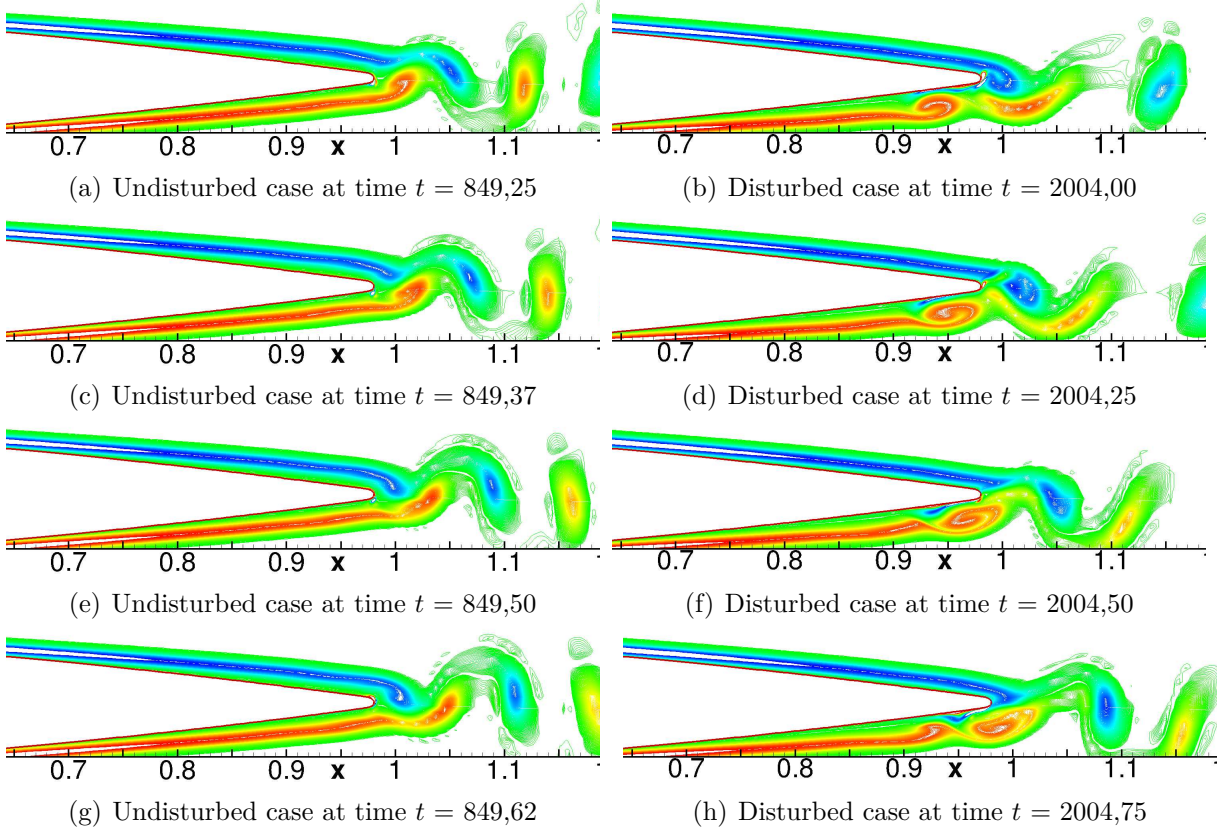


Figure 4.6: Iso-contours of instantaneous vorticity over the range $\omega = \pm 20$ at trailing edge region for surface 1 AoA = 0 deg, $Re_c = 100000$ and $M_\infty = 0.2$.

dominant peak of the spectrum.

In Fig. 4.7 (b), one can observe the effects of compressibility on far-field pressure, in this figure a comparison of $|p'|$ for an observer location at 5 chords distant from the airfoil, at vortex shedding frequency is performed for the three Mach number studied. It was found that the higher the Mach number the higher the noise radiate into the farfield. The above results follows the trend found for low Reynolds in section 3.

Figure 4.8 presents the near-field pressure spectra measured at a quarter chord distant perpendicularly from the trailing edge for surface 1 AoA = 0 deg. $Re_c = 100000$. In fig. 4.8 (a), it can be observed that hydrodynamics changes due to compressibility affects strongly the noise spectra structure. One can see that compressibility effects play an important role in the appearance of the secondary tones. For the lower Mach number flow analyzed, the main tonal peak is easily observed with a non-dimensional frequency of $k_s c = 3.577$ and amplitude of $|p'_s| = 3.86 \times 10^{-4}$, but the presence of secondary tones is questionable, and along with the laminar separation bubble along the trailing edge and its subsequent vortex shedding shown in figure 4.2 (a), confirms that even at this Reynolds number and under these conditions the main noise generation mechanism is the vortex shedding, and the conditions for the secondary tones formation are not met.

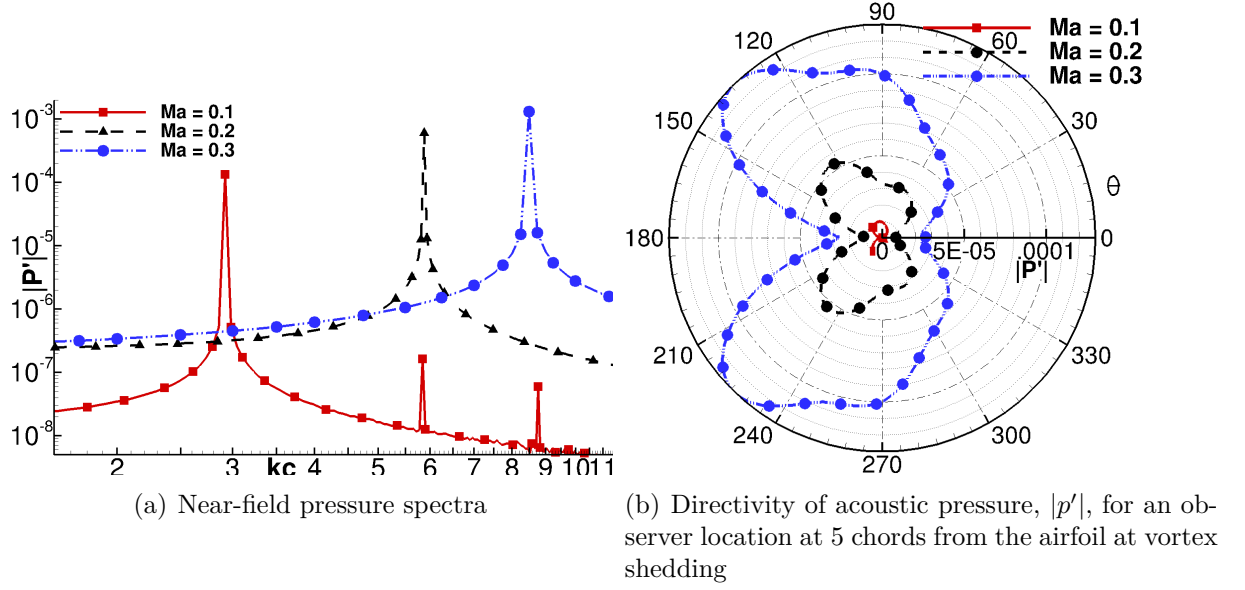


Figure 4.7: (a) Near-field pressure spectra, and (b) Directivity of acoustic pressure, $|p'|$, for an observer location at 5 chords from the airfoil at vortex shedding, of surface 1 AoA = 0 deg, $Re_c = 50000$ and $M_\infty = 0.1 - 0.3$.

Figure 4.8 (b) and (c) present the near-field pressure spectra obtained for surface 1 AoA = 0 deg, $Re_c = 100000$, $M_\infty = 0.2$, undisturbed and disturbed cases, respectively. The main non-dimensional frequency k_sc , the main non-dimensional acoustic amplitude $|p'_s|$ and the tone frequency spacing Δkc are shown in table 4.3 for the above cases. It turns out that for $M_\infty = 0.2$ undisturbed, the main non-dimensional frequency k_sc is higher but with a lower main non-dimensional acoustic amplitude $|p'_s|$. The secondary tones formation is obvious for both cases, with the difference that the latter case has more secondary tones with higher amplitude than the former one. When the hydrodynamic and the acoustic properties are connected, one can observe that a stronger and larger separation bubble along the trailing edge is related with an increasing in the main and secondary tones amplitude and more secondary tones in the acoustic pressure spectrum. It could be that these structures increase the boundary layer receptivity in relation to any kind of external perturbation. and, since only acoustics perturbations may propagate upstream from the wake and propagate along the boundary layer, the receptivity increasing amplifies these acoustic waves, increasing the noise scattered and creating the conditions for the development of more secondary tones.

Figure 4.8 (d) presents the near field pressure spectrum for surface 1 AoA = 0 deg, $Re_c = 100000$ and $M_\infty = 0.3$. Here, the secondary tones equidistant and centered on a main tonal peak are clearly observed together with the broad spectral hump. The spectrum shows a cluster of peaks with a frequency spacing of $\Delta kc = 0.68160$ and centered at main non-dimensional frequency $k_sc = 10.932$. As mentioned before, structures like separation

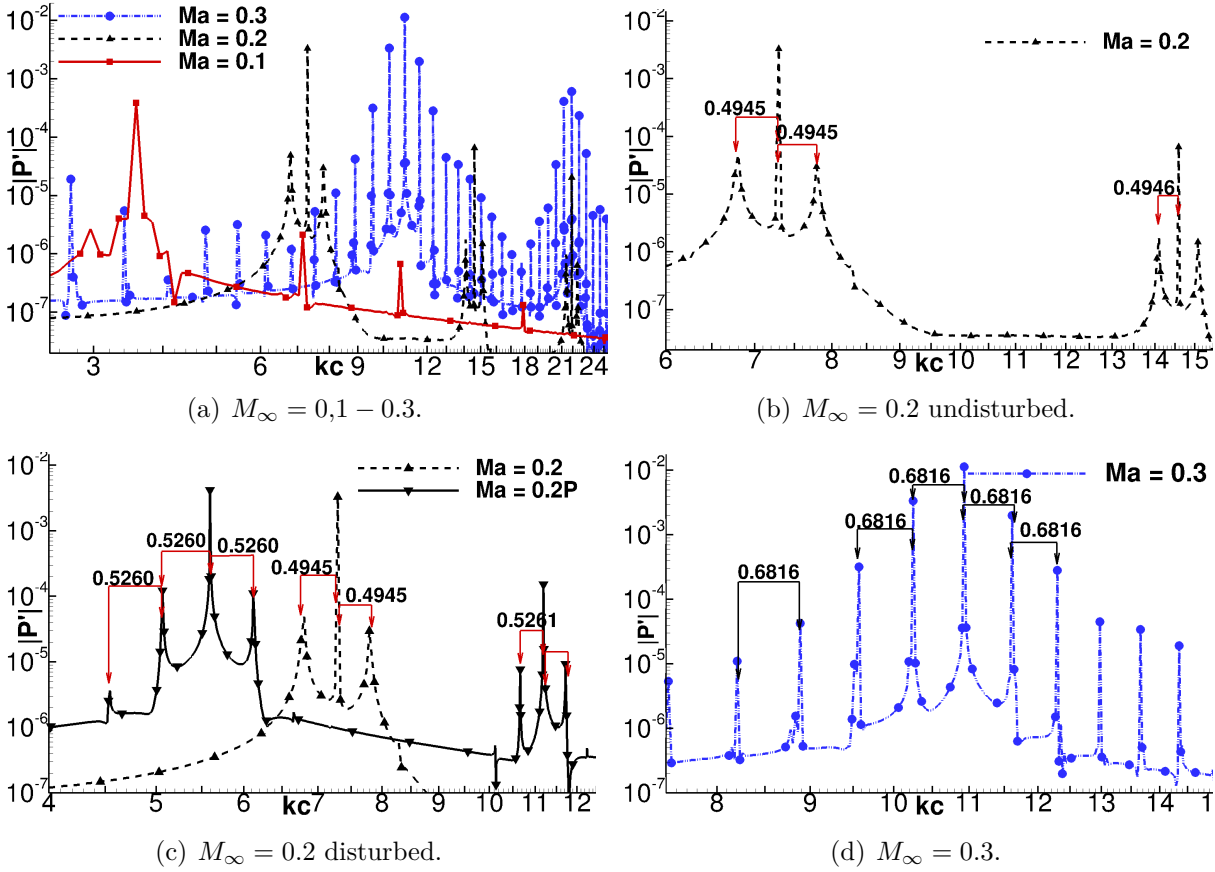


Figure 4.8: Near-field pressure spectra obtained for surface 1 with $\text{AoA} = 0$ deg. and $Re_c = 100000$.

bubbles and shear layer vortices increase the boundary layer receptivity, amplifying the noise scattered and creating the conditions for the secondary tones formation.

Table 4.2: Near-field spectra data for surface 1 $\text{AoA} = 0$ deg. and $Re_c = 50000$

Freestream Mach number	$M_\infty = 0.1$	$M_\infty = 0.2$	$M_\infty = 0.3$
Main non-dimensional frequency $k_s c$	2.920	6.067	8.493
Main non-dimensional acoustic amplitude $ p'_s $	1.33×10^{-4}	5.99×10^{-4}	1.30×10^{-3}

Figure 4.9 presents a comparison of (a) pressure fluctuations along airfoil surface and (b) directivities of acoustic pressure, for an observer location at 5 chords from the airfoil, for surface 1 $\text{AoA} = 0$ deg, $Re_c = 100000$. In figure 4.9 (a) one can observe that as freestream Mach number increases the amplitude of pressure fluctuations increases, being this behavior more noticeable near the trailing edge ($x/c = 0.85$ and further downstream). Additionally, a comparison for the two $M_\infty = 0.2$ cases (the undisturbed and disturbed) shows an overall pressure fluctuations increasing for the disturbed case, moreover, an increasing of almost 50% in pressure amplitude was found at the pressure peaks located at $x/c = 0.98$. In fig. 4.9 (b) one can see that not only the pressure amplitude increases in function of freestream Mach number, but also, the changing in directivity shape. For

Table 4.3: Near-field spectra data for surface 1 AoA = 0 deg. and $Re_c = 100000$

Freestream Mach number	$M_\infty = 0.1$	$M_\infty = 0.2$	$M_\infty = 0.2$ dist.	$M_\infty = 0.3$
Main non-dimensional frequency $k_s c$	3.577	7.295	5.594	10.932
Main non-dimensional acoustic amplitude $ p'_s $	3.86×10^{-4}	3.29×10^{-3}	4.17×10^{-3}	1.13×10^{-2}
Tone frequency spacing $\Delta k c$	—	0.49458	0.52607	0.68160

instance, because of the higher frequency, the directivity for $M_\infty = 0.3$ presents 4 lobes compared to $M_\infty = 0.1$ that has the shape of a classical dipole shape.

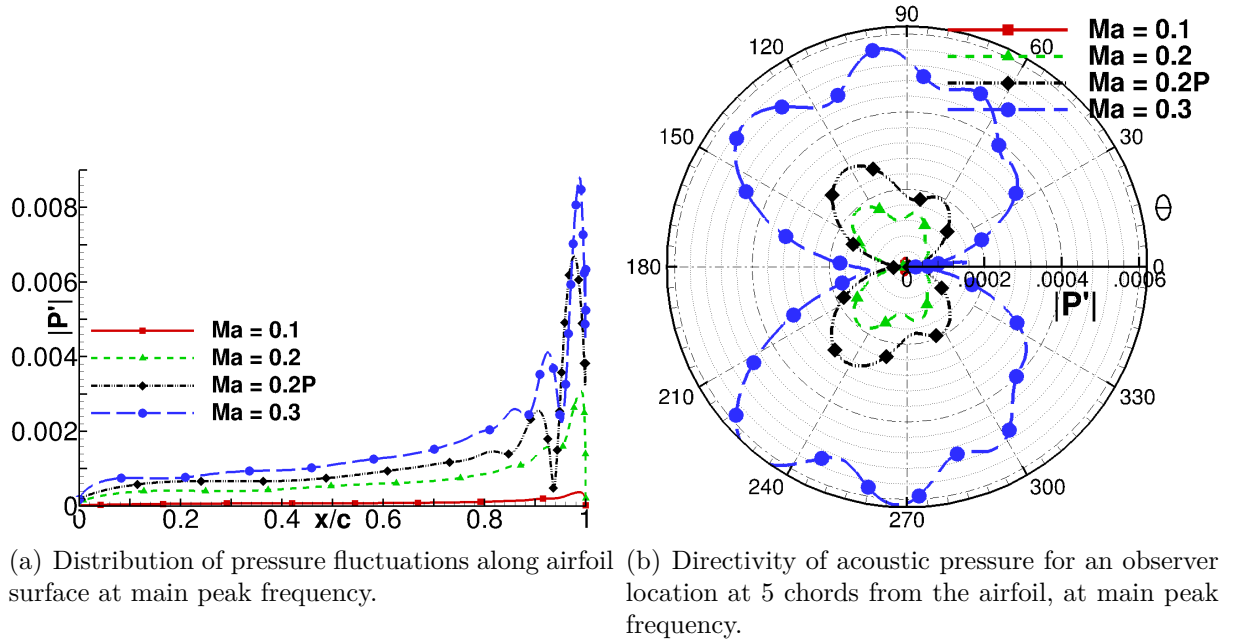


Figure 4.9: Comparison of (a) pressure fluctuations $|p'|$, along airfoil surface and (b) directivities of acoustic pressure, $|p'|$, for an observer location at 5 chords from the airfoil, for surface 1 AoA = 0 deg. and $Re_c = 100000$.

Figure 4.10 presents the spatial distribution of the quadrupole sources, \hat{T}_{11} , at main peak frequency, for surface 1 AoA = 0 deg. and $Re_c = 100000$. Once the flows are symmetric and non-symmetric for $M_\infty = 0.1$ and 0.3, respectively, the spatial distributions of quadrupole sources, which compose the incident acoustic fields, should reflect these differences as one can see in figs. 4.10 (a) and (b). When the disturbance is applied, this not only made the flow non-symmetric but also increased the magnitudes of quadrupole sources and moved it upstream along the lower surface and trailing edge.

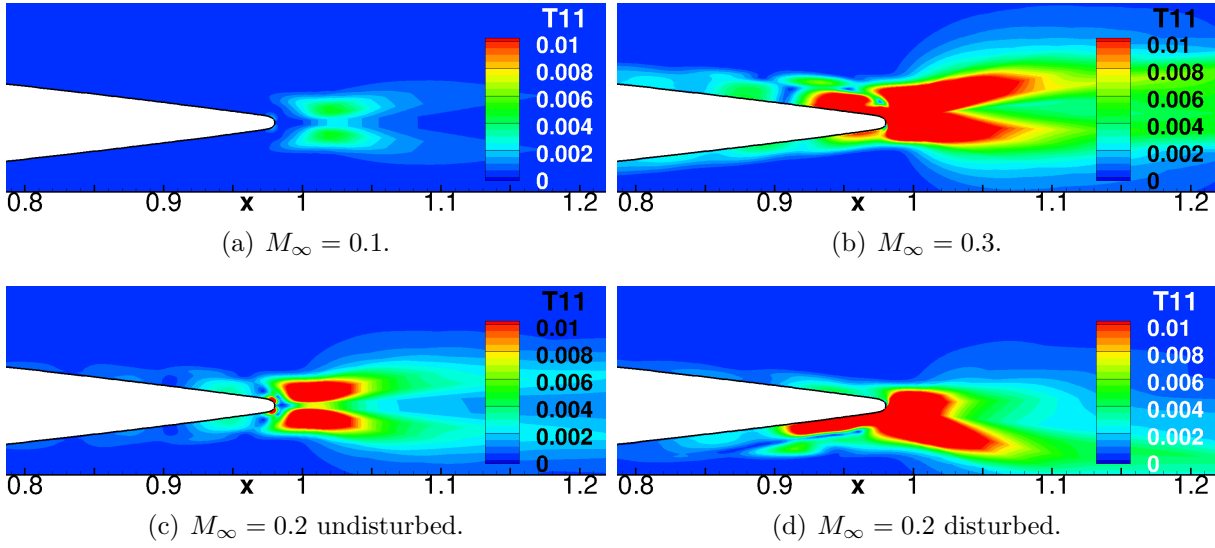


Figure 4.10: Spatial distribution of the quadrupole sources over the range of $\hat{T}_{11} = 0$ to 0.01, at main peak frequency, for surface 1 AoA = 0 deg. and $Re_c = 100000$.

4.3 Effects of Angle of Attack on Noise Generation

Figure 4.11 presents a sequence of instantaneous streamlines and vorticity for the case surface 1 AoA = 3 deg, $Re_c = 50000$ and $M_\infty = 0.1$. Unlike the zero incidence case, with AoA = 3 deg, the separation boundary layer occurs under this Reynolds number and for the three Mach number studied. The separation starts at $x/c = 0.4$ on suction side of the airfoil, then the separated shear layer rolls-up into laminar vortices and is shed at $x/c = 0.65$. But It turns out that the most of roll-up vortices proceed to merge with either one or two other vortices downstream. The vortex merging occurs at $x/c = 0.74$. This merging phenomenon between two vortices was found to occur periodically for all freestream Mach number. After the vortex merging, the resulting is a larger structure that convects downstream. A previous experimental study of Kirk (2014) found the same phenomena in a NACA0018 airfoil with $Re_c = 100000$ and at angle of attack of 5 and 8 degrees.

The same physical phenomena are found for when the Reynolds number is increased to $Re_c = 100000$, but unlike the above case, smaller and more quantity of shear layer vortices are convected downstream were observed, at some instants until six vortices were observed rolling downstream on suction side of the airfoil. Figures 4.12 shows a sequence of snapshots of flow streamlines and vorticity for the $M_\infty = 0.1$ case. Here the separation starts at $x/c = 0.40$, then, the laminar vortex shedding occurs at $x/c = 0.55$, later, the vortex merging occurs at $x/c = 0.80$ and ultimately these structures are convected at trailing edge.

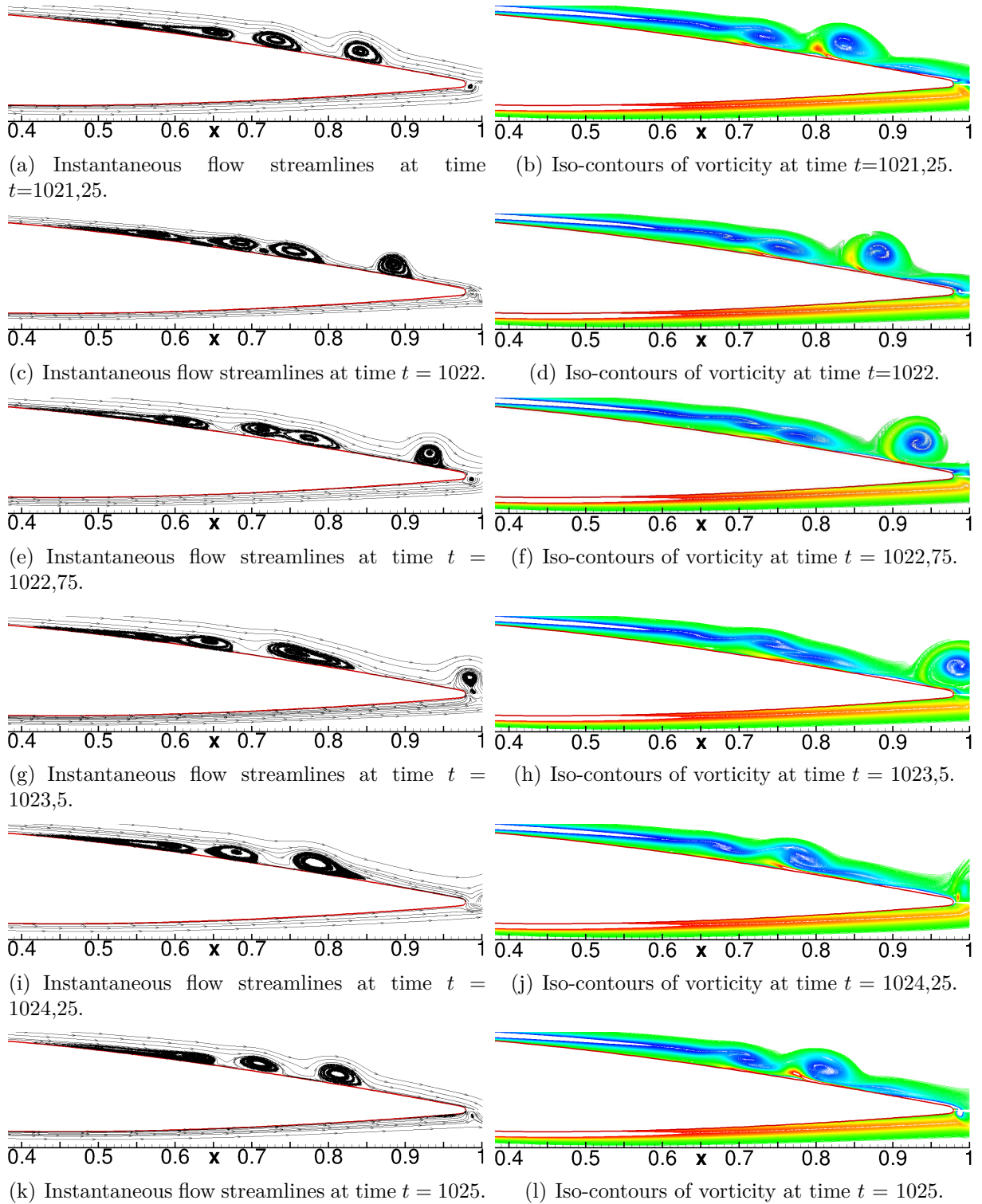


Figure 4.11: Snapshots of flow streamlines (left) and Iso-contours of instantaneous vorticity over the range $\omega = \pm 9$ (right) of surface 1 AoA = 3 deg, $Re_c = 50000$ and $M_\infty = 0.1$.

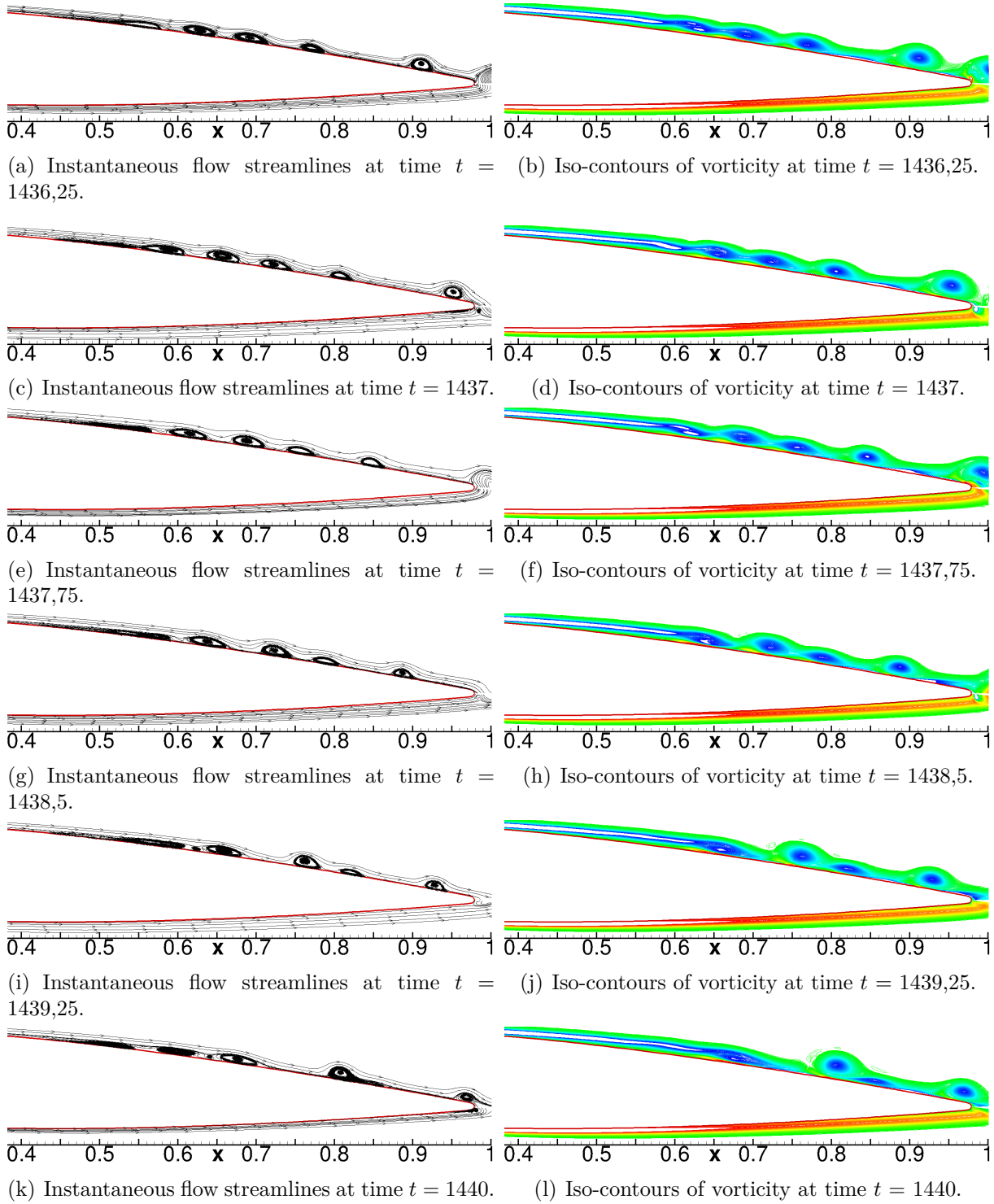


Figure 4.12: Snapshots of flow streamlines (left) and iso-contours of instantaneous vorticity over the range $\omega = \pm 12$ (right) of surface 1 AoA=3 deg. $Re_c = 100000$ and $M_\infty = 0.1$.

As expected, the increasing in angle of attack directly affects the radiated noise scattered from the airfoil trailing edge. Figures 4.13 and 4.14 depict the acoustic near-field pressure spectra for surface 1 AoA = 3 deg, $Re_c = 50000$ and $Re_c = 100000$, respectively. One can observe the secondary tones equidistant and centered on a main tonal peak together with the broad spectral hump for all the six cases analyzed. For the former Reynolds number, the higher the Mach number the greater the number of secondary tone centered on a main peak, and larger the tone frequency spacing Δkc (see table 4.4). Comparing data from table 4.2 and table 4.4, one can see clearly that an increasing in angle of attack, leads to an increasing in the main non-dimensional acoustic amplitude $|p'_s|$ and a decreasing in the main non-dimensional frequency k_sc .

The behavior for the $Re_c = 100000$ case seems to follow the same pattern except for the $M_\infty = 0.1$ case, where several secondary peaks were found, however they seems in disorder rather than equidistant and centered in a main peak, as it was found for the other two cases. From figs. 4.14 (c) and (d) one can observe that the higher the Reynolds the greater the quantity of secondary tones, however the tone frequency spacing Δkc is reduced. Figure 4.15 presents a comparison in terms of (a) near-field pressure spectra and (b) directivities of far-field noise, between the AoA = 0 and AoA = 3 degrees cases (tables 4.3 for and 4.5 show in detail the data from AoA = 0 and AoA = 3 degrees, respectively), where the following trends are found. One can observe that an increasing in angle of attack leads to a slight decreasing in the main non-dimensional acoustic amplitude $|p'_s|$, also, leads to a decreasing in the main non-dimensional frequency k_sc and a slight decreasing in total noise scattered into the far-field. But at the same time, this angle of attack increasing yields an increasing in the tone frequency spacing Δkc , and an increasing in the quantity of secondary tones.

Table 4.4: Near-field spectra data for surface 1 AoA = 3 deg. and $Re_c = 50000$

Mach No	$M_\infty = 0.1$	$M_\infty = 0.2$	$M_\infty = 0.3$
Main non-dimensional frequency k_sc	1.408	3.27	4.603
Main tone amplitude $ p'_s $	4.77×10^{-4}	2.32×10^{-3}	4.91×10^{-3}
Tone frequency spacing Δkc	0.33127	0.58803	0.90430

Table 4.5: Near-field spectra data for surface 1 AoA = 3 deg. and $Re_c = 100000$

Mach No	$M_\infty = 0.1$	$M_\infty = 0.2$	$M_\infty = 0.3$
Main non-dimensional frequency k_sc	2.579	4.29	6.06
Main non-dimensional acoustic amplitude $ p'_s $	3.72×10^{-4}	3.47×10^{-3}	8.87×10^{-3}
Tone frequency spacing Δkc	—	0.54331	0.8666

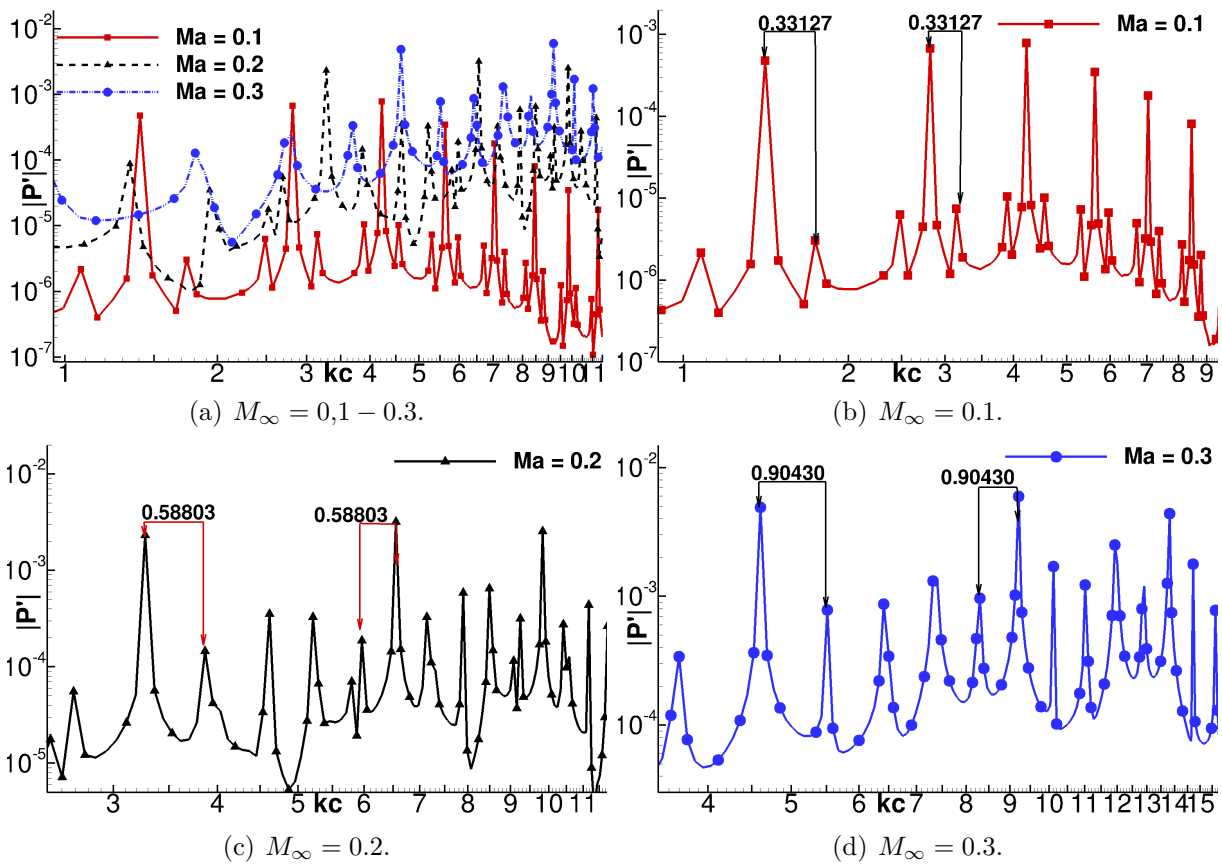


Figure 4.13: Near-field pressure spectra obtained for surface 1 $\text{AoA} = 3^\circ$ and $Re_c = 50000$.

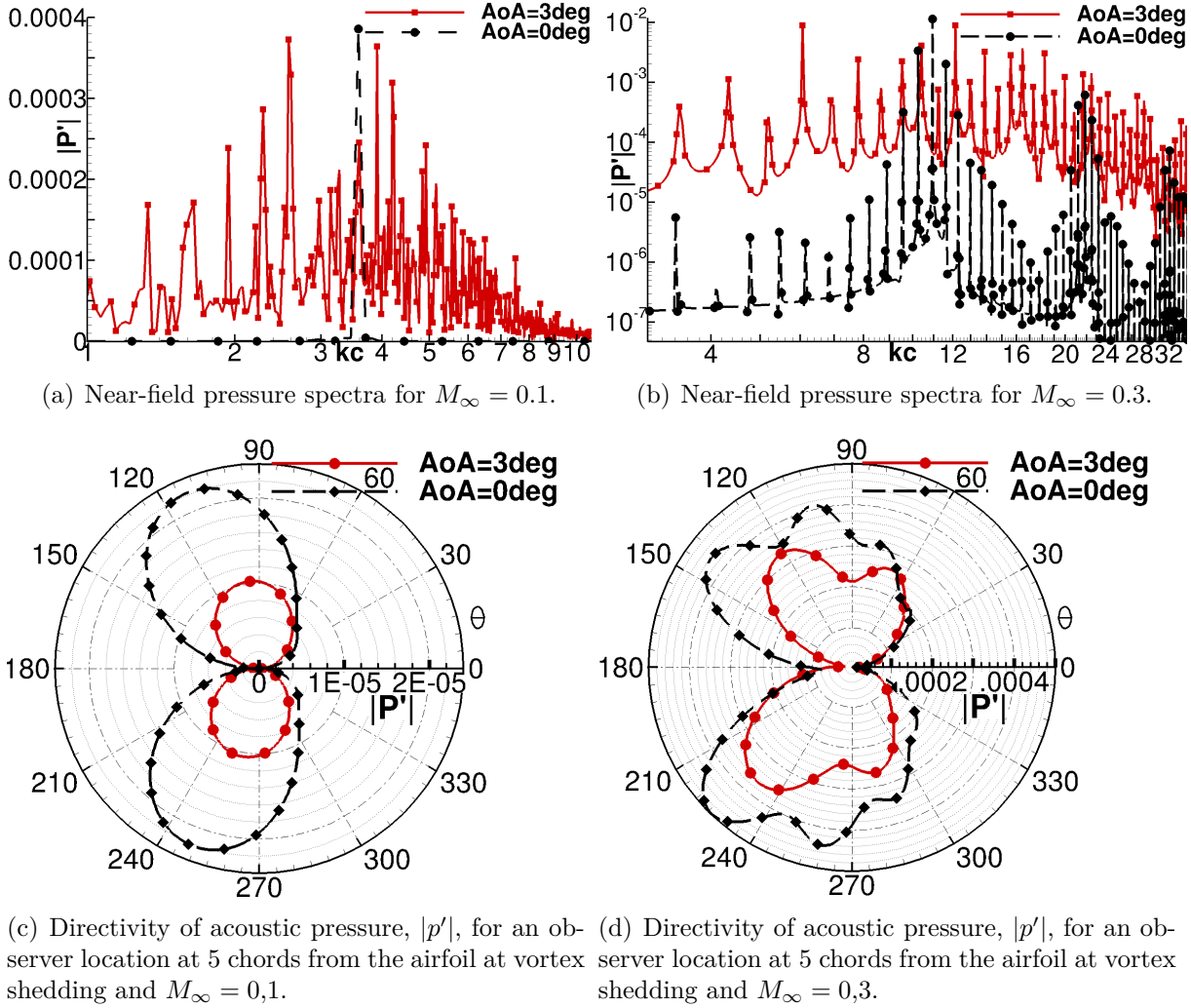


Figure 4.15: Effects of angle of attack on noise scattered for surface 1 $AoA = 0$ and $AoA = 3^\circ$, $Re_c = 100000$, $M_\infty = 0.1$ (left) and $M_\infty = 0.3$ (right).

4.4 Effects of Trailing Edge Bluntness on Noise Generation

To examine the changes caused by trailing edge bluntness on noise generation and propagation, hydrodynamic and acoustic properties are compared for two NACA 0012 airfoils with modified trailing edges. As previously explained, surface 1 has a thin trailing edge profile whereas, surface 2 has a thick trailing edge (see Fig. 1.3 for a visualization of the two airfoil trailing edge profiles and table 1.1 for detailed information of them). Figure 4.16 presents a comparison of the time averaged flow streamlines along the trailing edge airfoil for the two surfaces. For the thinner trailing edge, a larger and more elongated separation bubble is observed over the airfoil suction side while for the thicker trailing edge, a more compact separation bubble is observed only behind the trailing edge. When the Reynolds number is increased a shorter separation bubble is developed as one can see from figures 4.16 (c) and (d). It is worth mentioning that for the whole suite of simulations of surface 2 at zero incidence, no laminar vortices rolling downstream at the suction nor

pressure side are observed, unlike the thinner trailing edge airfoil. Furthermore, it turns out that under these conditions, the behavior resembles that of low Reynolds regime, where the vortex shedding is the principal mechanism of noise generation.

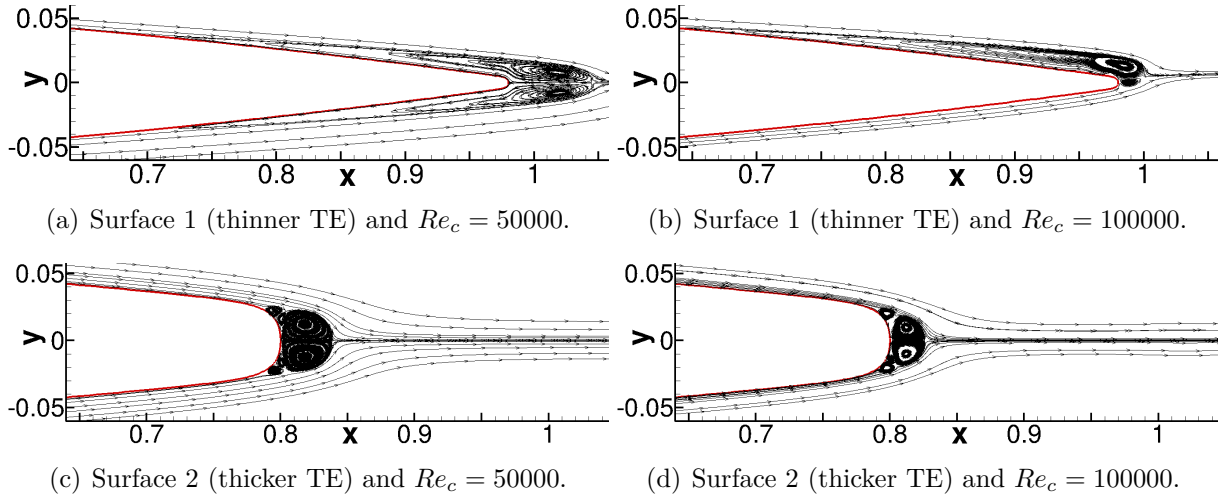


Figure 4.16: Mean flow streamlines along trailing edge for surface 1 (top) and surface 2 (bottom), and AoA = 0 deg, $Re_c = 50000$ (left), $Re_c = 100000$ (right), and $M_\infty = 0.3$.

However, when the angle of attack is increased to 3 deg. the hydrodynamic behavior of surface 2 changes, becoming more similar to the surface 1. Figure 4.17 depicts snapshots of flow streamlines (left) and vorticity (right) over the range $\omega = \pm 14$ of surface 2 AoA = 3 deg. $Re_c = 100000$ and $M_\infty = 0.1$. Under these conditions, the separation boundary layer occurs at $x/c = 0.50$ on suction side of airfoil, then, the separated shear layer rolls-up into laminar vortex, which is convected downstream, but unlike to surface 1, here no vortex merging is observed. Furthermore it is observed when results for $Re_c = 50000$ and $Re_c = 100000$ that the higher the Reynolds number, smaller and more quantity of laminar vortices along the suction side of airfoil. It is worth pointing out that laminar separation bubbles rolling downstream on suction side are observed for the whole suite of simulations of surface 2 with AoA = 3 deg.

Despite of having similar hydrodynamic properties in some cases, surface 2 presents a different behavior regarding the self-noise structure. Figure 4.18 shows the near-field pressure spectra for the 12 flow configurations analyzed for surface 2 at moderate Reynolds numbers. These spectra were measured at a quarter of chord perpendicular to the trailing edge. In figure 4.18 (a) and (b) the whole suite of zero incidence cases are plotted for $Re_c = 50000$ and $Re_c = 100000$, respectively. Clearly, for none of these cases secondary tones are observed, but only a main tonal peak where its amplitude increases as the freestream Mach number increases. Figure 4.18 (c) and (d) show the spectra for the whole suite of AoA = 3 deg. cases, and despite of having the laminar separation bubbles rolling-up downstream on suction side of airfoil, no secondary tone is found either for

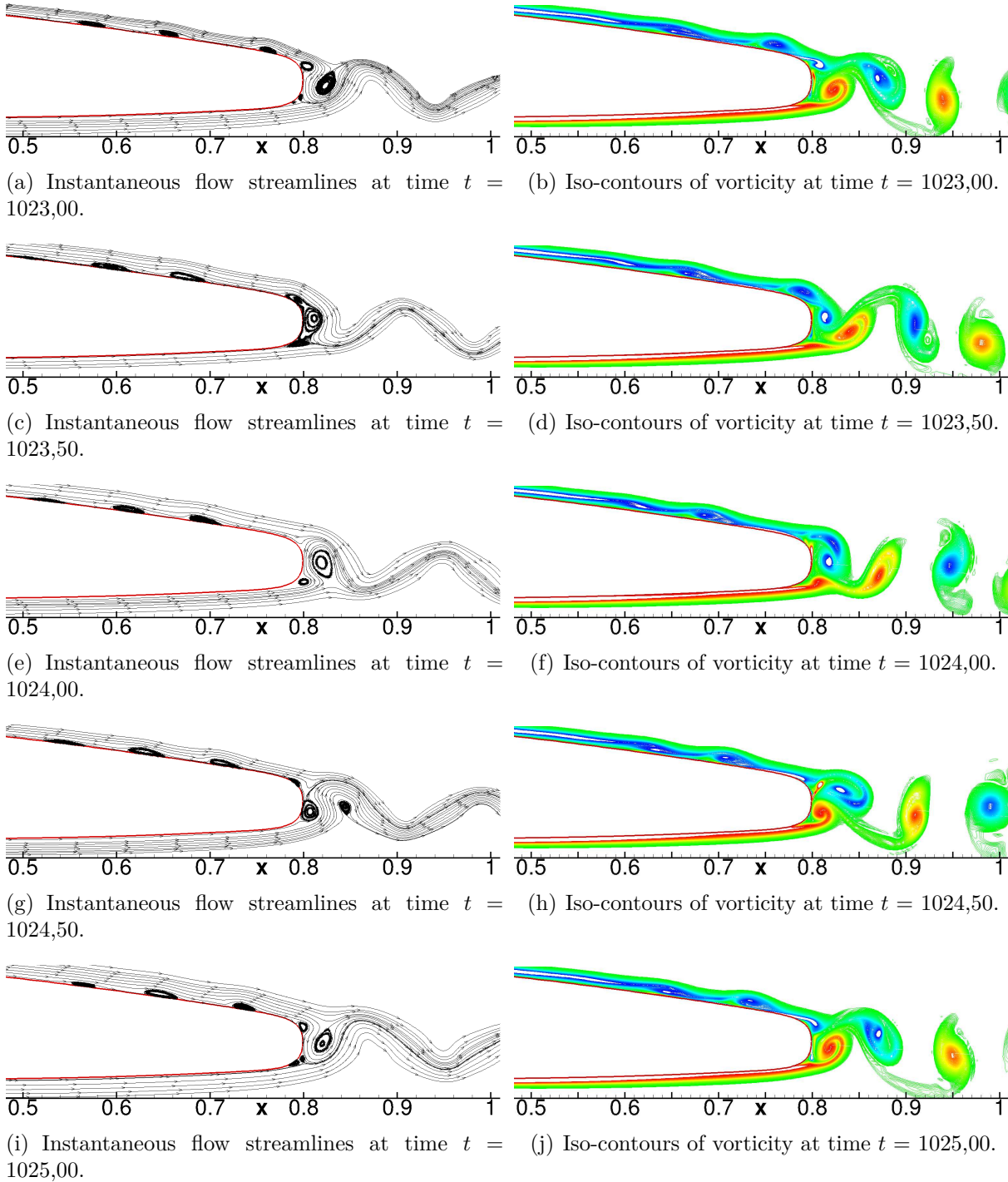


Figure 4.17: Snapshots of flow streamlines (left) and iso-contours of vorticity (right) over the range $\omega = \pm 14$ along trailing edge for surface 2 AoA = 3 deg, $Re_c = 100000$ and $M_\infty = 0.1$.

the most cases. Only the $\text{AoA} = 3^\circ$, $Re_c = 100000$ and $M_\infty = 0.1$ case presents the secondary tones equidistant and centered on a main tonal peak together with the broad spectral hump.

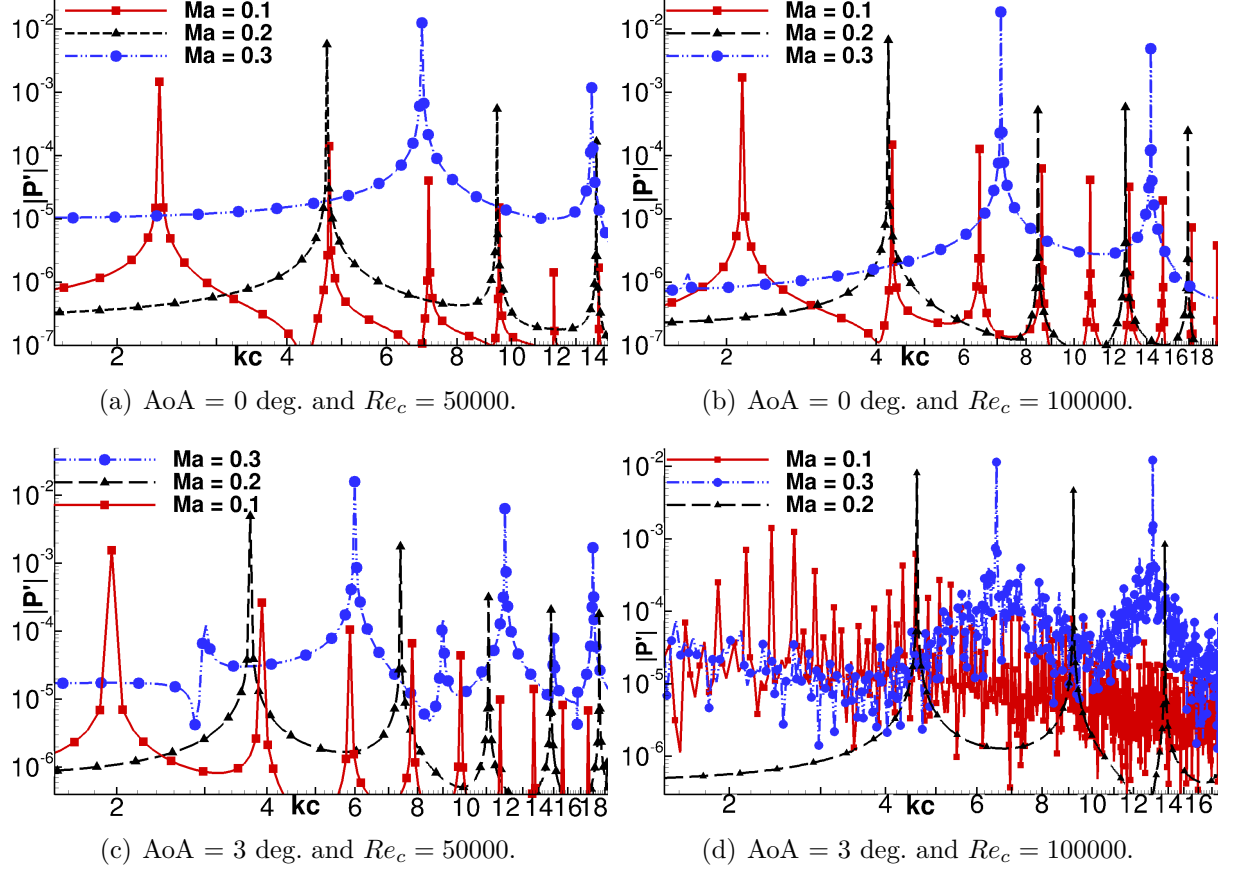


Figure 4.18: Near-field pressure spectra for surface 2.

Tables 4.6 and 4.7 detail the near-field spectra data for the zero incidence cases with $Re_c = 50000$ and $Re_c = 100000$, respectively. Similarly, tables 4.8 and 4.9 show the near-field spectra data for the $\text{AoA} = 3^\circ$ cases with $Re_c = 50000$ and $Re_c = 100000$, respectively. Comparing results of tables 4.6 and 4.7 with results of tables 4.2 and 4.3 that details the data for the same flow parameters for surface 1, one can see that for the thicker trailing edge surface, the main non-dimensional acoustic amplitude $|p'_s|$ is increased by an order of magnitude at least, and the main non-dimensional frequency k_sc is shifted to a lower one. These behavior as mentioned before, resembles the behavior of low Reynolds number. However a different behavior is observed for the $\text{AoA} = 3^\circ$ cases, comparing results of tables 4.8 and 4.9 with results of tables 4.4 and 4.5, it can be observed that, although there is an increasing in the main non-dimensional acoustic amplitude $|p'_s|$, the main non-dimensional frequency k_sc is increased too.

Table 4.6: Near-field spectra data for surface 2 AoA = 0 deg. and $Re_c = 50000$.

Mach No	$M_\infty = 0.1$	$M_\infty = 0.2$	$M_\infty = 0.3$
Main non-dimensional frequency $k_s c$	1.940	3.840	5.658
Main non-dimensional acoustic amplitude $ p'_s $	1.45×10^{-3}	5.73×10^{-3}	1.25×10^{-2}

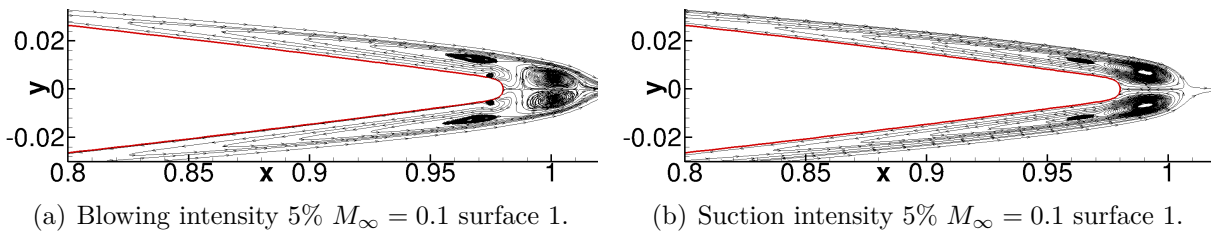
Table 4.7: Near-field spectra data for surface 2 AoA = 0 deg. and $Re_c = 100000$.

Mach No	$M_\infty = 0.1$	$M_\infty = 0.2$	$M_\infty = 0.3$
Main non-dimensional frequency $k_s c$	2.151	4.226	7.121
Main non-dimensional acoustic amplitude $ p'_s $	1.72×10^{-3}	6.70×10^{-3}	1.86×10^{-2}

4.5 Effects of Suction & Blowing at Trailing Edge on Noise Generation

Keeping the same trend used in chapter 3, with the aim of evaluate possibilities for noise reduction, as previously shown, steady suction and blowing are performed along the two trailing edge profiles analyzed (see 1.4 for a visualization of the regions where suction and blowing are applied). The previous findings has shown that vortex shedding is not the only noise mechanism for moderate Reynolds, so, it is expected that suction & blowing will impact the hydrodynamics mechanisms that produce not only the main tone, but also, the secondary ones. As explained in chapter 3 blowing and suction are employed with no time variations since these would introduce an additional noise source.

Figure 4.19 (a) and (b) show a comparison of the mean flow streamlines along the trailing edge for the cases with blowing intensity of 5% and suction intensity of 5%, respectively. Here one can observe, that blowing and suction cause disturbances that produce a laminar bubble of recirculation, with a larger recirculation bubble size for the blowing case and located right up and down the trailing edge.

Figure 4.19: Comparison of blowing and suction effects on mean flow streamlines at trailing edge region for AoA = 0 deg, $Re_c = 100000$ and $M_\infty = 0.1$.

Regarding the acoustics, figure 4.20 presents the acoustic pressure spectra measured at $1/4$ of chord perpendicular to the trailing edge for the blowing and suction cases. When the blowing and suction is applied, the main non-dimensional acoustic amplitude $|p'_s|$ (related to the main tonal peak) is slightly increased as well as the secondary tones;

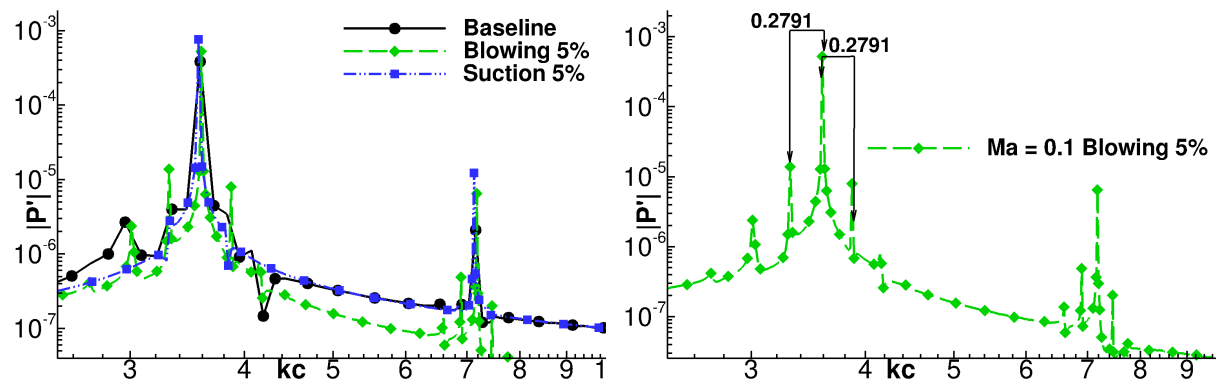
Table 4.8: Near-field spectra data for surface 2 AoA = 3 deg. and $Re_c = 50000$.

Mach No	$M_\infty = 0.1$	$M_\infty = 0.2$	$M_\infty = 0.3$
Main non-dimensional frequency $k_s c$	1.953	3,698	5.987
Main non-dimensional acoustic amplitude $ p'_s $	1.55×10^{-3}	4.97×10^{-3}	1.59×10^{-2}

Table 4.9: Near-field spectra data for surface 2 AoA = 3 deg. and $Re_c = 100000$.

Mach No	$M_\infty = 0.1$	$M_\infty = 0.2$	$M_\infty = 0.3$
Main non-dimensional frequency $k_s c$	2.156	4.59	6.48
Main non-dimensional acoustic amplitude $ p'_s $	7.04×10^{-4}	8.13×10^{-3}	1.15×10^{-2}
Tone frequency spacing $\Delta k c$	0.2599	–	–

becoming into a well-defined spectrum with secondary tones for the blowing case as one can observe in green dashed line in fig. 4.20 (a). Furthermore, the secondary tones are equidistant and centered on the main peak as shown in fig. 4.20 (b). It could be that the recirculation bubble that is observed in figure 4.19 (a) amplifies the boundary layer receptivity with respect to the external acoustic disturbances that travels upstream from the wake, creating the necessary conditions for the acoustic feedback loop occurs.



(a) Acoustic pressure spectra at $M_\infty = 0.1$, comparison with and without suction and blowing 5% (b) Acoustic pressure spectra at $M_\infty = 0.1$ with blowing 5%

Figure 4.20: Effects of suction and blowing on pressure spectra of surface 1 AoA = 0 deg. $Re_c = 100000$ and $M_\infty = 0.1$. Comparison of baseline case, with blowing 5% and suction 5% cases.

Figure 4.21 shows similar results in terms of pressure spectra for $M_\infty = 0.3$. One should remember that, for this case, the flow is non-symmetric and secondary tones as well as a broadband hump, are clearly seen. In Fig. 4.21 (a) spectra are shown in log \times log format and in Fig 4.21 (b) they are shown in linear \times log format for better visualization of the tonal peaks. From these figures, one can see that suction and blowing tend to reduce the frequencies and amplitudes of the main peaks, however, these disturbances cause the formation of stronger secondary peaks and suction, in particular, introduces a strong broadband content to the spectrum.

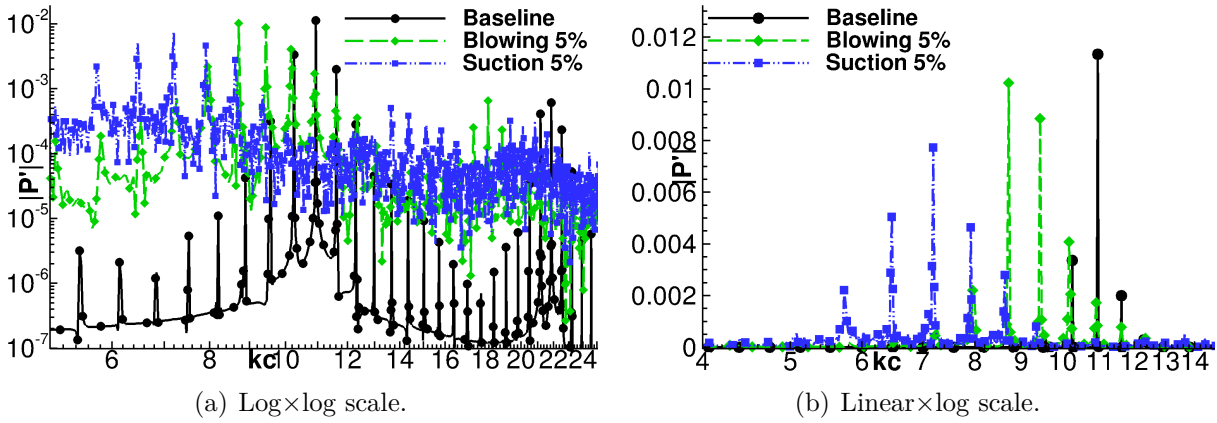


Figure 4.21: Acoustic pressure spectra of surface 1 $AoA = 0$ deg, $Re_c = 100000$ and $M_\infty = 0.3$, comparison of baseline case with suction and blowing 5% cases. (a) log \times log scale, (b) linear \times log scale.

Figure 4.22 (a) and (b) shows similar results in terms of pressure spectra for the $AoA = 3$ deg, $Re_c = 100000$ and $M_\infty = 0.3$ with blowing intensity 5% and suction 5%, respectively. In these figures, pressure spectra can be compared for the undisturbed case and also when blowing and suction of $5\%M_\infty$ are applied. The figure 4.22 (b) of pressure spectra is presented in log-linear format in order to provide a clearer visualization of the tonal peaks. From both figures, one can see that multiple tones are excited for the current configuration. When blowing is applied, the main tonal peaks are amplified. However, blowing considerably reduces the amplitudes of the secondary tones, as well as, the broadband noise. On the other hand, suction reduces the amplitudes of the main tones and increases those of the secondary ones.

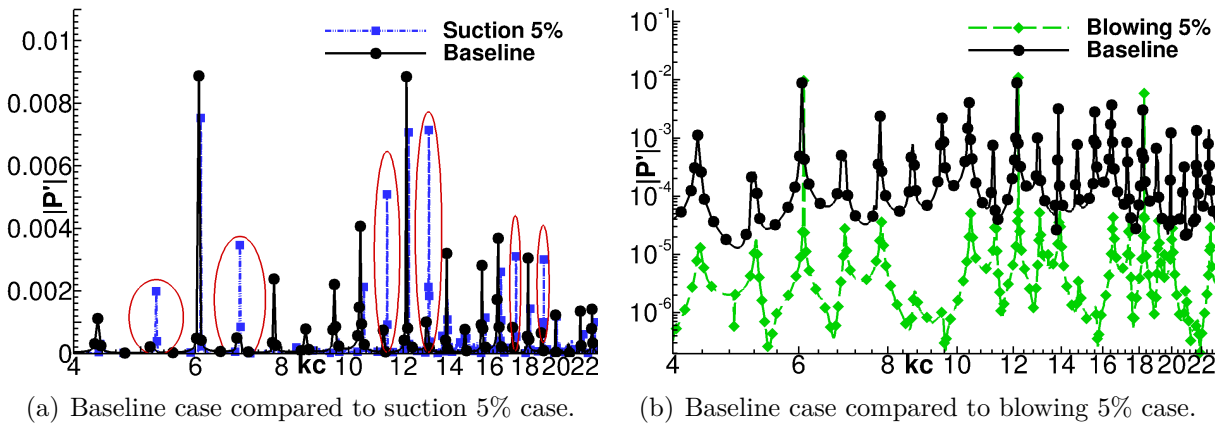


Figure 4.22: (a) Suction & (b) blowing effects on acoustic pressure spectra of surface 1 $AoA = 3$ deg, $Re_c = 100000$ and $M_\infty = 0.3$.

Regarding the thicker trailing edge surface, figure 4.23 (a) and (b) present a comparison of acoustic pressure spectra for the baseline cases (without blowing) and with blowing intensity 10%, for the zero incidence and $AoA = 3$ deg. cases, respectively. For the former case (no-incidence) the spectrum shows the regular tonal peaks associated with the vortex

shedding frequency, and similarly to the low Reynolds number case analyzed, blowing reduces the amplitudes of the main tonal peaks. The latter case with $\text{AoA} = 3^\circ$, the spectrum presents secondary tones equidistant and centered to the main tonal peak. Trailing edge blowing for this case, reduces the amplitude of main peaks and eliminate the secondary tones.

Figure 4.24 (a) and (b) show the mean flow streamlines for the baseline case and blowing $10\%M_\infty$ case, respectively, for the surface 2 with no-incidence, $Re_c = 100000$ and $M_\infty = 0.1$. One can visualize the recirculation region just behind the blunt trailing edge for the former case. No separation is observed for the latter case with blowing. As observed for the low Reynolds numbers flow studied in chapter 3, the spatial distribution of quadrupole sources is severely affected by blowing for surface 2. These results can be seen in Figs. 4.25 (a) and (b) which show that quadrupole sources vanish close to the trailing edge surface when blowing is applied.

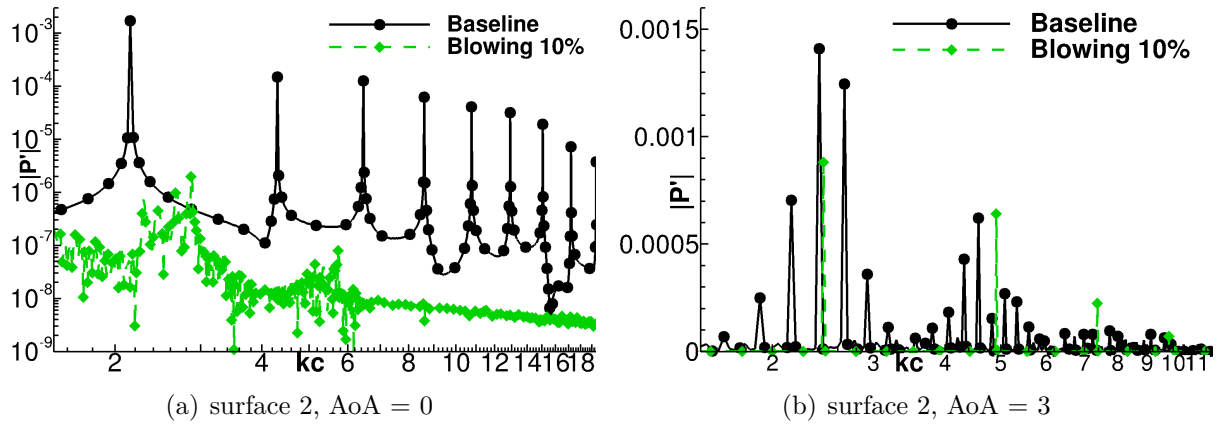


Figure 4.23: Blowing effects on pressure spectra of surface 2 for (a) $\text{AoA} = 0^\circ$. and (b) $\text{AoA} = 3^\circ$, and $Re_c = 100000$ and $M_\infty = 0.1$.

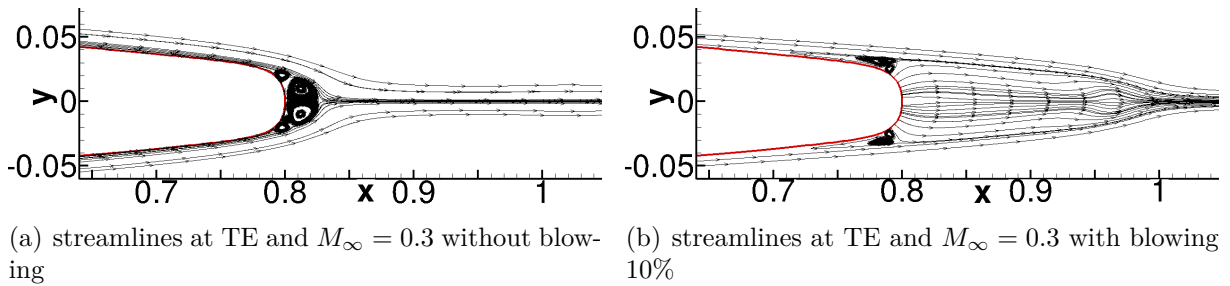


Figure 4.24: Blowing effects on mean flow streamlines at trailing edge region for surface 2, $\text{AoA} = 0^\circ$, $Re_c = 100000$ and $M_\infty = 0.3$.

Table 4.10 shows the effects of trailing edge bluntness, angle of attack, and suction & blowing at trailing edge on the overall sound pressure level (OASPL) at moderate Reynolds numbers. In this table, results are shown in terms of ΔOASPL compared to a baseline case, which appears as case 6. Here one can observe that whereas the effects

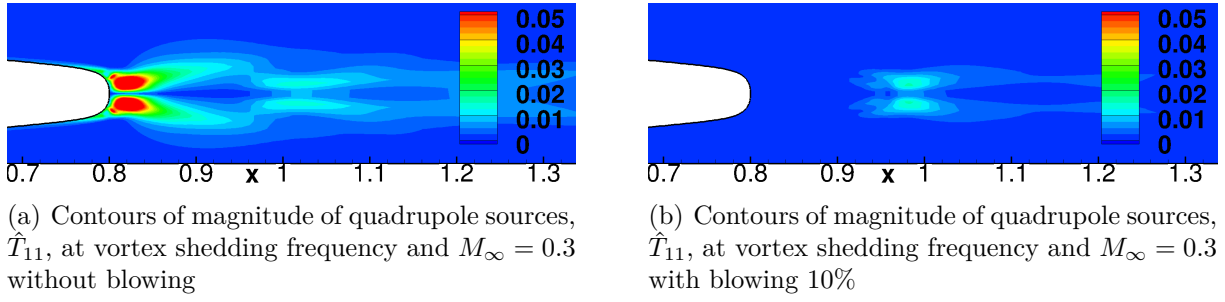


Figure 4.25: Spatial distribution of the quadrupole sources over the range of $\hat{T}_{11}=0$ to 0.05, at main peak frequency, for surface 2 AoA = 0 deg. $Re_c = 100000$ and $M_\infty = 0.3$ and (a) baseline case and (b) blowing 10% case.

of angle of attack present a well-defined behavior of increasing the total noise produced for both surfaces (compare case 1 with 6, and case 4 with 9), the effects of trailing edge bluntness present a different behavior depending on the angle of attack. For instance, for no-incidence cases, one can observe that surface 2 generates more total noise than surface 1 (compare case 1 with 4). However, when the angle of attack increases to 3 deg., surface 2 produces less total noise than surface 1 (compare case 6 with 9). Blowing presents a well-defined behavior of reducing noise for surface 2. Comparing cases 4 with 5, and 9 with 10, one can observe that noise is significantly reduced when blowing at trailing edge is applied. Nevertheless, suction & blowing have an effect that depends on the angle of attack for surface 1. For no-incidence cases, suction and blowing increase the total noise, but when the angle of attack increases to 3 deg, suction and blowing decrease the total noise.

Table 4.10: Overall sound pressure level for moderate Reynolds number cases.

Case	Airfoil	AoA	Re_c	M_∞	% Suction	% Blowing	$\Delta OASPL$
1	Surface 1	0 deg.	100000	0.3	–	–	–16.42
2	Surface 1	0 deg.	100000	0.3	5%	–	+4.76
3	Surface 1	0 deg.	100000	0.3	–	5%	+3.84
4	Surface 2	0 deg.	100000	0.3	–	–	–3.00
5	Surface 2	0 deg.	100000	0.3	–	10%	–10.54
6	Surface 1	3 deg.	100000	0.3	–	–	0.00
7	Surface 1	3 deg.	100000	0.3	5%	–	–4.10
8	Surface 1	3 deg.	100000	0.3	–	5%	–18.88
9	Surface 2	3 deg.	100000	0.3	–	–	–2.70
10	Surface 2	3 deg.	100000	0.3	–	10%	–6.13

5 CONCLUSIONS

5.1 Summary

Direct numerical simulations are conducted for compressible flows past a NACA 0012 airfoil with different blunt trailing edges. A study of tonal noise generation is performed for low and moderate Reynolds numbers including an assessment the influence of compressibility, angle of attack and Reynolds number as well as trailing edge suction and blowing.

Numerical results for the low Reynolds number flow studied show that for increased Mach number, the dominant tonal peak increases in amplitude and shifts to higher frequencies. For increased trailing edge bluntness, the dominant tonal peak increases in amplitude and shifts to lower frequencies. Furthermore, it is found that, a blunter trailing edge surface emits more noise than a thinner one due to an increase in the magnitudes of quadrupole sources near the trailing edge region. It is also found that the peak values of the quadrupole sources get closer to the airfoil surface for blunter trailing edges, which also increases noise scattering.

Results for the moderate Reynolds number flow analyzed show that the airfoil may emit multiple “narrow-band” tones superimposed on a broadband hump, depending on the flow configuration. Compressibility effects play a major role in the tonal noise generation process when the airfoil with the thinner trailing edge is at zero angle of attack. For $M_\infty = 0.1$, the flow is symmetric and the presence of secondary tones due to an acoustic feedback loop is questionable. When the freestream Mach number is increased to $M_\infty = 0.3$, the flow becomes non-symmetric and secondary tones are clearly visible superimposed on a broadband hump. For $M_\infty = 0.1$, suction and blowing increase far field noise at the main frequency and secondary tones appear when blowing is applied. For $M_\infty = 0.3$, suction and blowing reduce the amplitudes of the tonal peaks which occur at lower frequencies. For the blunter trailing edge at $AoA = 0$ deg, the tonal noise mechanism is similar to that of the low Reynolds number flow and a single tone is excited along with its harmonics. Blowing reduces the acoustic scattering in a similar fashion as for the low Reynolds number case.

When the airfoil with a thinner trailing edge is at an angle of incidence, it exhibits a spectrum with secondary tones and the acoustic feedback loop is present. Compressibility effects do not play a major role here. For this case, the secondary tones disappear when blowing is applied but the main tones have their magnitudes amplified. Suction, on the other hand, reduced the magnitude of the main tones while increasing that of the sec-

ondary ones. Compressibility effects become important for the blunter trailing edge when the airfoil is at a non-zero angle of incidence. Differently from previous cases analyzed, here, secondary tones are observed for $M_\infty = 0.1$ and blowing eliminates these secondary tones and reduces the magnitude of the main tone. For $M_\infty = 0.2$, the spectrum resembles that of a low Reynolds number flow and blowing eliminates these tones. For $M_\infty = 0.3$ secondary tones, equidistant and centered on a main peak are observed, but unlike the $M_\infty = 0.1$ case, the secondary tones have a lower pressure amplitude.

Figure 5.1 gathers the results for the suite of studied cases. Here, the dominant tonal peak amplitude of each case is plotted as a function of Helmholtz number $kc=2\pi fc$ for the three different Mach numbers. This figure presents an overall picture where the effects of compressibility, trailing edge bluntness, angle of attack, and Reynolds number on the dominant tonal peak amplitude and frequency can be observed. Each line has 3 points which represent the three different Mach numbers used ($M_\infty = 0.1, 0.2$ and 0.3 from left to right) for every case analyzed. Continuous lines and dashed lines represent results for the thinner and thicker trailing edge, respectively. As expected, results show that, the higher the Mach and Reynolds numbers, the higher the tonal peak amplitude and frequency. The previous observation fails in the comparison of the results for $M_\infty = 0.1$, for the moderate Reynolds numbers, for the thinner trailing edge at angle of incidence. Also, one can observe that the higher the angle of attack, the higher the tonal peak amplitude but this leads a to a lower tonal peak frequency. Finally, as shown previously, a blunter trailing edge surface produces a higher tonal peak amplitude with a lower frequency.

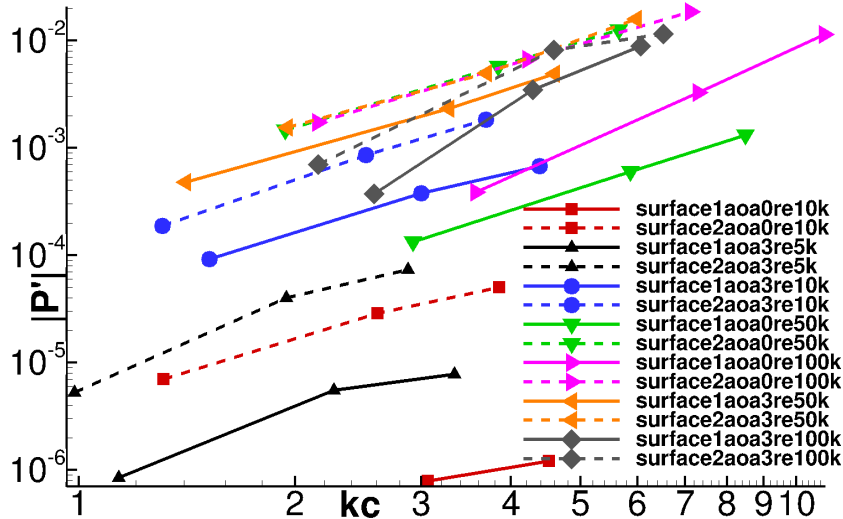


Figure 5.1: Tonal peak amplitude behavior as a function of Helmholtz number $kc=2\pi fc$ for the suite of studied cases.

Figure 5.2 presents a summary for the entire suite of cases studied, showing the cases where the secondary tones are found. Here, one can observe that not only the Reynolds

numbers but also, compressibility and angle of attack play a main role in the appearance of secondary tones. For Reynolds number of $Re_c = 50000$, only surface 1 with angle of attack 3 deg, presents secondary tones in its spectra; meanwhile, for $Re_c = 100000$, all cases of surface 1 present secondary tones, except that with no-incidence and Mach number $M_\infty = 0.1$. For surface 2, only cases with $Re_c = 100000$ and angle of attack 3 deg, present secondary tones, except the case with $M_\infty = 0.2$.

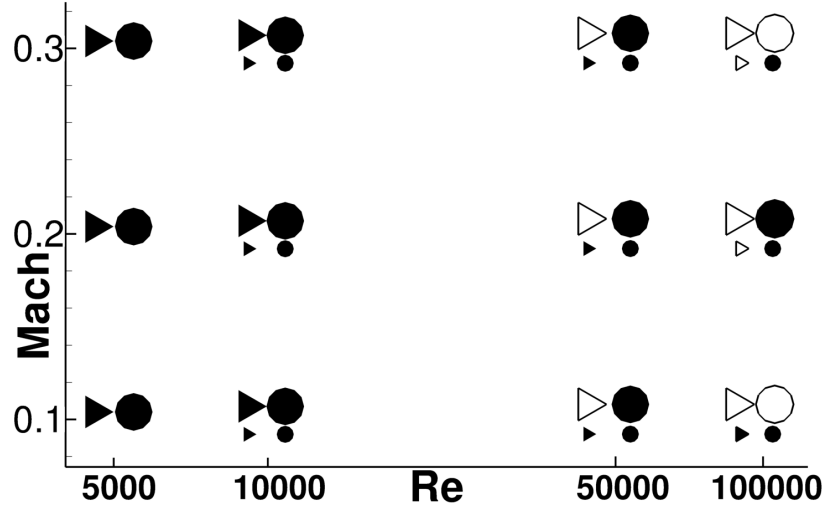


Figure 5.2: Cases where secondary tones are found. Filled triangle symbol ▶ means surface 1 with no secondary tones, empty triangle symbol ▷ means surface 1 with secondary tones, filled circle symbol ● means surface 2 with no secondary tones, empty circle symbol ○ means surface 2 with secondary tones. Large symbols represent cases with angle of attack 3 deg, and small symbols represent cases with angle of attack 0 deg.

Regarding the Appendix A, a continuous and a discrete forcing approach were implemented in the immersed boundary method (IBM) and the suitability of these methods combined with a high-order finite difference scheme has been examined on several acoustic scattering and unsteady flow problems including shock waves. A suite of two-dimensional numerical simulations of canonical cases were conducted with the aim of analysing the error behavior associated with the IBM, through wave reflection, wave diffraction, shock-wave diffraction, and shock-boundary layer interaction phenomena.

In general, it was found that the discrete forcing approach presents a better performance in terms of computational cost. Moreover, this method presents more accurate results compared against the continuous forcing approach. In the continuous forcing approach results shown, the largest error is related to the wave reflection phenomenon. Furthermore, the size of the region where the continuous forcing term is applied plays a major role in the solutions.

5.2 Future Work

There is potential for further investigation in several topics appearing in the present work. The further work could increase the understanding of physical phenomena involved in the airfoil self-noise generation, as well as, an improvement in the novel numerical methods presented in appendix A.

It was found the existence of secondary tones superimposed on a broad spectral hump centered on main frequency, confirming the appearance of the so-called “ladder-like structure”, however, despite of great efforts that have been carried out to improve the understanding of the airfoil tonal noise phenomenon, a comprehensive and widely accepted description of the physical mechanisms causing the rise of secondary tones is needed. Although the “acoustic feedback loop” has been suggested for several authors as the main driver mechanism for these tones, its existence is questionable, and each author suggests its own description. To address this issue a stability analysis over a wide range of cases is suggested as an alternative for future work.

Although the airfoil self-noise generation phenomenon can be considered as a two-dimensional process as shown by (PATERSON *et. al*; PLOGMANN *et. al*, 1973; 2013), this is specially valid for low to moderate Reynolds numbers flows. However, a three dimensional numerical study is suggested to examine the physics involved in noise generation for high Reynolds numbers flows.

Finally, new implementations can be performed in the “Pistl” methodology, where multi-body and moving bodies capabilities can be developed. Currently, the present author along with Prof. Dr. William Wolf and Dr. Britton Olson are currently working in the developing and implementation of several novel features for the continuous forcing approach and discrete forcing approach of the immersed boundary method, with the aim of increasing the precision and reducing the computational cost of the method.

Rerferences

ARBEY, H. and BATAILLE, J. Noise generated by airfoil profiles placed in a uniform laminar flow. **Journal of Fluid Mechanics**, vol. 134, 33–47, 9 1983.

ARIAS-RAMIREZ, W. and WOLF, W. The effects of suction and blowing on tonal noise generation by blunt trailing edges. In **Proceedings of the 21st AIAA/CEAS Aeroacoustics Conference**. Dallas, Texas, 2015a.

URL: <http://dx.doi.org/10.2514/6.2015-2364>

ARIAS-RAMIREZ, W. and WOLF, W.R. Effects of trailing edge bluntness on airfoil tonal noise at low reynolds numbers. **Journal of the Brazilian Society of Mechanical Sciences and Engineering**, pp. 1–12, 2015b.

URL: <http://dx.doi.org/10.1007/s40430-015-0308-6>

BEAM, R. and WARMING, R. An implicit factored scheme for the compressible navier-stokes equations. **AIAA Journal**, vol. 16, n. 4, 393–402, Apr 1978.

BHASKARAN, R. and LELE, S.K. Large eddy simulation of free-stream turbulence effects on heat transfer to a high-pressure turbine cascade. **Journal of Turbulence**, vol. 11, 2010.

BROOKFIELD, J.M. and WAITZ, I.A. Trailing-edge blowing for reduction of turbomachinery fan noise. **Journal of Propulsion and Power**, vol. 16, n. 1, 2000.

BROOKS, T.F.; POPE, D.S. and MARCOLINI, M.A. Airfoil self-noise and prediction. Technical report, NASA, 1989.

CHONG, T.P. and JOSEPH, P. An experimental study of tonal noise mechanism of laminar airfoils. In **15th AIAA/CEAS Aeroacoustics Conference (30th AIAA Aeroacoustics Conference)**, pp. 1–9. May 2009.

CLARK, L.T. The radiation of sound from an airfoil immersed in a laminar flow. **Journal of Engineering for Gas Turbines and Power**, vol. 93, n. 4, 366–376, Oct 1971.

CORCORAN, T.E., **Control of the wake from a simulated blade by trailing-edge blowing**, Master Thesis, Lehigh University, 1992.

CURLE, N. The influence of solid boundaries upon aerodynamic sound. **Proceedings of the Royal Society of London A: Mathematical, Physical and Engineering Sciences**, vol. 231, n. 1187, 505–514, 1955.

DESQUESNES, G.; TERRACOL, M. and SAGAUT, P. Numerical investigation of the tone noise mechanism over laminar airfoils. **Journal of Fluid Mechanics**, vol. 591, 155–182, 11 2007.

DOBRZYNSKI, W. Almost 40 years of airframe noise research: What did we achieve? **Journal of Aircraft**, vol. 47, n. 2, 353–367, Mar 2010.

ENGHARDT, L.; KAUSCHE, P.; MOREAU, A. and CAROLUS, T.H. Active control of fan tones by means of trailing edge blowing. In **Proceedings of the 21st AIAA/CEAS Aeroacoustics Conference**. Dallas, Texas, 2015.

URL: <http://dx.doi.org/10.2514/6.2015-2828>

FADLUN, E.; VERZICCO, R.; ORLANDI, P. and MOHD-YUSOF, J. Combined immersed-boundary finite-difference methods for three-dimensional complex flow simulations. **Journal of Computational Physics**, vol. 161, n. 1, 35 – 60, 2000.

FFOWCS WILLIAMS, J.E. and HAWKINGS, D.L. Sound generation by turbulence and surfaces in arbitrary motion. **Philosophical Transactions of the Royal Society of London. Series A, Mathematical and Physical Sciences**, vol. 264, n. 1151, pp. 321–342, 1969.

FINK, M.; SCHLINKER, R. and AMIET, R. Prediction of rotating-blade vortex noise from noise of non-rotating blades. Technical report, NASA, 1976.

FINK, M.R. Prediction of airfoil tone frequencies. **Journal of Aircraft**, vol. 12, n. 2, 118–120, Feb 1975.

GOLDSTEIN, D.; HANDLER, R. and SIROVICH, L. Modeling a no-slip flow boundary with an external force field. **Journal of Computational Physics**, vol. 105, n. 2, 354 – 366, 1993.

HERSH, A. and HAYDEN, R. Aerodynamics sound radiation from lifting surfaces with and without leading edge serrations. Technical report, NASA, 1971.

HUTCHESON, F. and BROOKS, T. Effects of angle of attack and velocity on trailing edge noise. In **42nd AIAA Aerospace Sciences Meeting and Exhibit**, Aerospace Sciences Meetings, pp. 1–18. Jan 2004.

J., M.Y. Combined immersed boundary b-spline methods for simulation of flow in complex geometries. **Annual Research Briefs, Center for Turbulence Research**, pp. 317–28, 1997.

JONES, L. and SANDBERG, R. Numerical investigation of tonal airfoil self-noise generated by an acoustic feedback-loop. In **Proceedings of the 16th AIAA/CEAS Aeroacoustics Conference**. 2010.

KIRK, T.M., **The later stage of transition over a NACA0018 airfoil at low Reynolds number**, Master Thesis, University of Waterloo, 2014.

KUROTAKI, T.; SUMI, T.; ATOBE, T. and HIYAMAE, J. Numerical simulation around naca0015 with tonal noise generation. In **Proceedings of the 46th AIAA Aerospace Sciences Meeting and Exhibit**, pp. 1–16. Reno, Nevada, 2008. Paper no2008-672.

LELE, S.K. Compact finite difference schemes with spectral-like resolution. **Journal of Computational Physics**, vol. 103, n. 1, 16–42, 1992.

LELE, S.K. and NICHOLS, J.W. A second golden age of aeroacoustics? **Philosophical Transactions of the Royal Society A: Mathematical, Physical and Engineering Sciences**, vol. 372, n. 2022, 2014.

LOCKARD, D. An efficient, two-dimensional implementation of the fflowcs william and hawkins equation. **Journal of Sound and Vibration**, vol. 229, n. 4, 897–911, 2000.

LOCKARD, D. A comparison of flowcs williams-hawkings solvers for airframe noise applications. In **Proceedings of the 8th AIAA/CEAS Aeroacoustics Conference**. 2002.

URL: <http://dx.doi.org/10.2514/6.2002-2580>

LOCKARD, D.P. and LILLEY, G. The airframe noise reduction challenge. Technical report, NASA, 2004.

LONGHOUSE, R. Vortex shedding noise of low tip speed, axial flow fans. **Journal of Sound and Vibration**, vol. 53, n. 1, 25 – 46, 1977.

LYRINTZIS, A. Surface integral methods in computational aeroacoustics—from the (cfd) near-field to the (acoustic) far-field. **International Journal of Aeroacoustics**, vol. 2, n. 2, 95–128, 2003.

URL: <http://dx.doi.org/10.1260/147547203322775498>

MITTAL, R.; DONG, H.; BOZKURTTAS, M.; NAJJAR, F.; VARGAS, A. and VON LOEBBECKE, A. A versatile sharp interface immersed boundary method for incompressible flows with complex boundaries. **Journal of Computational Physics**, vol. 227, n. 10, 4825 – 4852, 2008.

MITTAL, R. and IACCARINO, G. Immersed boundary methods. **Annual Review of Fluid Mechanics**, vol. 37, n. 1, 239–261, 2005.

NAGARAJAN, S., **Leading-edge effects in bypass transition**, PhD Thesis, Stanford University, 2004.

NAGARAJAN, S.; LELE, S.K. and FERZIGER, J.H. A robust high-order compact method for large eddy simulation. **Journal of Computational Physics**, vol. 191, n. 2, 392–419, 2003.

NASH, E.; LOWSON, M. and MCALPINE, A. Boundary-layer instability noise on aerofoils. **Journal of Fluid Mechanics**, vol. 382, 27–61, 3 1999.

NAUMANN, R.G., **Control of the wake from a simulated blade by trailing-edge blowing**, Master Thesis, Lehigh University, 1992.

OERLEMANS, S. and MÉNDEZ, B. Acoustic array measurements on a full scale wind turbine. In **Proceedings of the 11th AIAA/CEAS Aeroacoustics Conference**. Monterey, California, 2005.

OLSON, B.J., **Large-Eddy Simulation of Multi-Material Mixing and Over-Expanded Nozzle Flow**, PhD Thesis, Stanford University, 2012.

PATERSON, R.; VOGT, P.; FINK, M. and MUNCH, C. Vortex noise of isolated airfoils. **Journal of Aircraft**, vol. 10, 296–302, 1973.

PESKIN, C.S. Flow patterns around heart valves: A numerical method. **Journal of Computational Physics**, vol. 10, n. 2, 252 – 271, 1972.

PLOGMANN, B.; HERRIG, A. and WÜRZ, W. Experimental investigations of a trailing edge noise feedback mechanism on a naca 0012 airfoil. **Experiments in Fluids**, vol. 54, n. 5, 1480, 2013.

URL: <http://dx.doi.org/10.1007/s00348-013-1480-z>

SEO, J.H. and MITTAL, R. A high-order immersed boundary method for acoustic wave scattering and low-mach number flow-induced sound in complex geometries. **Journal of Computational Physics**, vol. 230, n. 4, 1000 – 1019, 2011.

SMITH, D.; PAXSON, R.; TALMADGE, R. and HOTZO, E. Measurements of the radiated noise from sailplanes. Technical report, US Air Force Flight Dynamics Laboratory, 1970.

TAM, C. and JU, H. Airfoil tones at moderate reynolds number: A computational study. In **Proceedings of the 17th AIAA/CEAS Aeroacoustics Conference (32nd AIAA Aeroacoustics Conference)**, pp. 1–30. Portland, Oregon, 2011.

TAM, C.K.W. Discrete tones of isolated airfoils. **The Journal of the Acoustical Society of America**, vol. 55, n. 6, 1173–1177, 1974.

WILLIAM, J.F. and HALL, L. Aerodynamcis sound generation by turbulent flow in the vicinity of a scattering half plane. **Journal of Fluids Mechanics**, vol. 40, 1970.

WOLF, W., **Airfoil Aeroacoustics, LES and Acoustic Analogy Prediction**, PhD Thesis, Stanford University, 2011.

WOLF, W.R.; AZEVEDO, J.L.F. and LELE, S.K. Convective effects and the role of quadrupole sources for aerofoil aeroacoustics. **Journal of Fluid Mechanics**, vol. 708, 502–538, 10 2012a.

WOLF, W.R.; AZEVEDO, J.L.F. and LELE, S.K. Effects of mean flow convection, quadrupole sources and vortex shedding on airfoil overall sound pressure level. **Journal of Sound and Vibration**, vol. 332, 6905–6912, 2013.

WOLF, W.R. and LELE, S. Acoustic analogy formulations accelerated by fast multipole method for two-dimensional. **AIAA Journal**, vol. 48, 2274–2285, 2010.

WOLF, W.R.; LELE, S.K.; JOTHIPRASARD, G. and CHEUNG, L. Investigation of noise generated by a du96 airfoil. In **18th AIAA/CEAS Aeroacoustics Conference (33th AIAA Aeroacoustics Conference)**, pp. 1–15. June 2012b.

APPENDIX A – COMPRESSIBLE FLOW SIMULATIONS OF WAVE SCATTERING PROBLEMS USING THE IMMERSED BOUNDARY METHOD

A.1 Note of Clarification

This appendix presents the activities performed and the scientific results obtained during the 6 month internship performed at Lawrence Livermore National Laboratory by the present author. This research was funded by the São Paulo State Research Foundation (FAPESP) from March/2015 to August/2015. The present author spent 6 months in the Weapon and Complex Integration (WCI) team under the supervision of Dr. Britton J. Olson.

The overseas internship research contributed to the investigation of aeroacoustic problems including airfoil noise through performing compressible simulations of unsteady flows including acoustic waves and shock waves. The present author worked on the development of a novel immersed boundary methodology combined with a high-order finite difference scheme that allows the study of flows past complex geometries. During the internship, novel numerical tools were developed and implemented by the present author and, finally, coupled to the Miranda code developed at Lawrence Livermore National Laboratory, LLNL.

The outcomes were presented in the 68th Annual Meeting of the American Physical Society - Division of Fluid Dynamics and are under review for presentation in the 2016 AIAA Aeroacoustics Conference. It is also important to mention that the research collaboration between the groups at UNICAMP and LLNL will continue and that this research is ongoing.

In the following sections, a brief introduction and theoretical background of the numerical methods are shown. Next, we present the methodology to carry out the numerical simulations and, finally, some numerical results for a suite of cases involving wave diffraction phenomenon including shock waves and acoustic waves.

A.2 Introduction

Flow-induced sound plays a main role in engineering applications such as transportation system and turbomachinery. The capability to understand the generation and propagation mechanisms of sound generation is essential to design quieter devices/machines. However, realistic aeroacoustic problems are associated with very complex geometries and accurate prediction of sound generation and propagation in such complex configurations is a challenging and expensive task. Simulations of sound wave generation/propagation requires high-performance computers and high-order non-dissipative, non-dispersive numerical methods which are appropriate to capture the physics of aeroacoustics and turbulence. Most of these methods are formulated on structured grids which are difficult and expensive to generate for complex geometries.

One of the numerical methods that overcome the above issues is called Immersed Boundary Method (IBM). The conventional CFD simulation approach uses computational meshes that conform to the body. Conforming structured grids take the shape of the geometry of interest and wall boundary conditions can be implemented in a straightforward fashion. The IBM represents another approach that, instead of using the conventional conforming grid, uses a simple Cartesian mesh which embeds the geometry of interest. However, since the grid does not conform to the geometry, the governing equations need to be modified in the vicinity of the body and those modifications are the baseline of the IBM.

In the present work, we apply the IBM to solve problems including acoustic wave reflection and diffraction, shock-wave reflection and shock-boundary layer interaction. Different IBM formulations are employed to solve the problems of interest and results are compared showing an error analysis for the different formulations. To perform the numerical simulations, we employ the Miranda code developed at Lawrence Livermore National Laboratory. The numerical tool solves the fully compressible Navier-Stokes equations in Cartesian coordinates and it combines the IBM with a tenth-order compact scheme for spatial discretization and a fourth-order Runge-Kutta scheme for time integration.

A.3 Theoretical Background

Consider employing a non-conforming Cartesian mesh for a simulation, as shown in Fig. A.1. In this approach, the Immersed Boundary (IB) will be represented by a surface grid. Thus, the solid boundary would cut through this Cartesian volume grid and because

the grid does not conform to the solid boundary, incorporating the boundary conditions would require:

- Establishing whether the grid points are inside or outside the body. In the present work, we develop a numerical tool based on the Point-in-Polyhedron (PiP) algorithm called Point in STL - “PiSTL”.
- Modifying the equations in the vicinity of the surface. These modifications represent the key factor in developing an IBM formulation and the form in which they are implemented into the Navier-Stokes equations differentiates one IBM formulation from another.

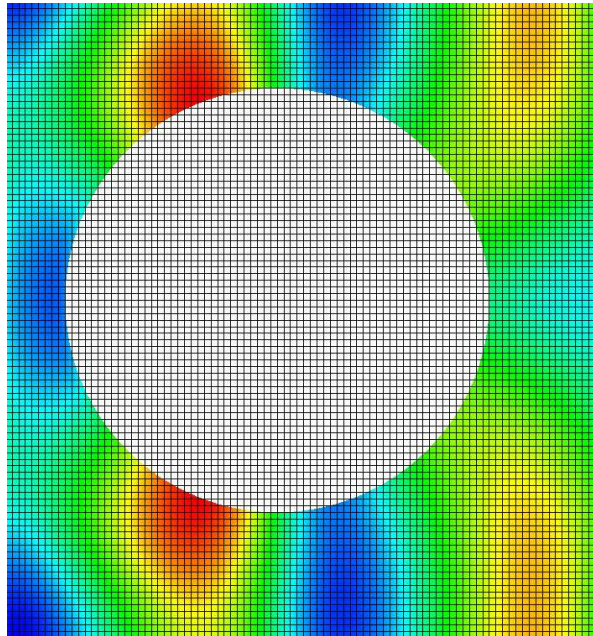


Figure A.1: Schematic of a cylinder immersed in a Cartesian grid.

A.3.1 Point in STL - “PiSTL”

In computational geometry, the Point-in-Polyhedron (PiP) problem asks whether a given point in space lies inside or outside a polyhedron. The STL format is chosen as the geometry input, since this format allows one to build almost any kind of three-dimensional body. The algorithm and the numerical tool are based in three principles: a “Bounding Box Filtering”, the “Ray Casting Methodology” and the “Point in Triangle Test (Barycentric Method)”.

After reading the geometry in STL format and converting it into faces, normal vectors and coordinates, the PiSTL code first computes a bounding box based on the minima

and maxima X,Y,Z coordinates of the body shape. The grid points outside this box are discarded and just the grid points inside it are considered in the next steps. Next, the Ray Casting Methodology is applied and this methodology is based on how many times a vertical ray departing from the Z coordinate of interest “pierces” the geometry. Whether the piercing amount is even or odd means the point of interest lies outside or inside the geometry, respectively. To compute the piercing, the Point in Triangle test is used through coordinate transformations. The test shows whether a point is inside a triangle or not. Figure A.2 shows results obtained by the PiSTL code developed by the present author for different geometries where the contour values split the inside and outside region.

A.3.2 Immersed Boundary Method

The IBM modifications take the form of a source term (or forcing function) in the Navier-Stokes equations that reproduce the effects of a solid boundary (slip and no-slip condition). Consider the simulation of a viscous compressible flow past a body, which is governed by the Navier-Stokes equations:

$$\frac{\partial \rho}{\partial t} + \frac{\partial(\rho u_i)}{\partial x_i} = 0 \quad (\text{A.1})$$

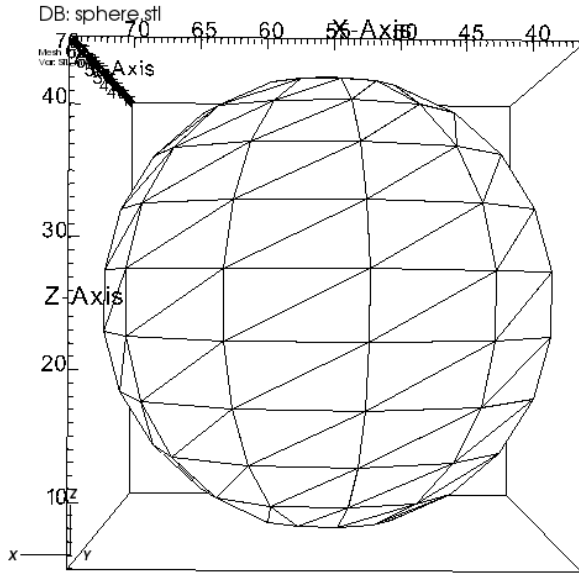
$$\frac{\partial(\rho u_i)}{\partial t} + \frac{\partial[\rho u_i u_j]}{\partial x_j} + \frac{\partial p}{\partial x_i} - \frac{\partial \tau_{ij}}{\partial x_j} = 0 \quad (\text{A.2})$$

$$\frac{\partial(e)}{\partial t} + (e + p) \frac{\partial u_i}{\partial x_i} = \frac{\partial(\tau_{ij} u_j)}{\partial x_i} + \frac{\partial(\dot{q}_i)}{\partial x_i} \quad (\text{A.3})$$

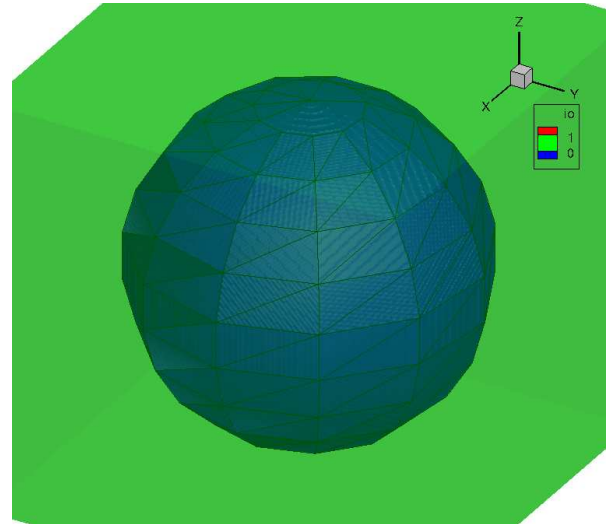
$$u_i = u_\Gamma \quad (\text{A.4})$$

where u_i represents the components of the fluid velocity vector in the i direction, p is the pressure, ρ is the density and τ_{ij} is the viscous stress tensor. The solid body occupies the domain Ω_b with boundary denoted by Γ_b , and the surrounding fluid domain is denoted by Ω_f (MITTAL AND IACCARINO, 2005).

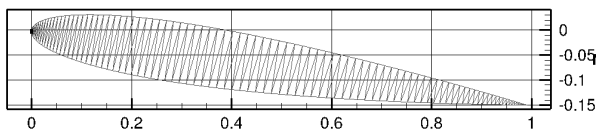
Conventional methods proceed by developing a discretization of Eqs. (A.1) and (A.2) on a body-conforming grid where the boundary conditions, Eq. (A.4), are directly enforced. In the IBM, the boundary condition will be imposed indirectly through the modification of Eqs. (A.1), (A.2) and (A.3). The introduction of a forcing function into the governing equations can be implemented in two different ways: Continuous Forcing Approach and Discrete Forcing Approach (MITTAL AND IACCARINO, 2005).



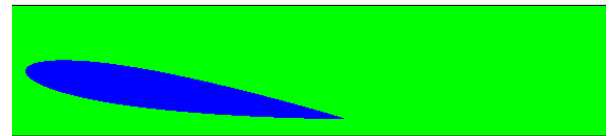
(a) Sphere.STL.



(b) PiSTL result over a sphere.



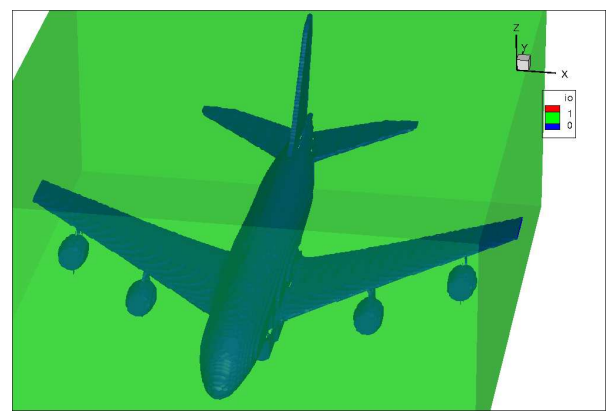
(c) NACA0012.STL airfoil.



(d) PiSTL result over NACA0012 airfoil.



(e) Airbus A380.STL.



(f) PiSTL result over Airbus A380.

Figure A.2: “PiSTL” results.

Continuous Forcing Approach

In this approach, the forcing function, denoted by f_b , is included into the continuous governing equation (Eq. (A.2)), leading to the following equations:

$$\frac{\partial \rho}{\partial t} + \frac{\partial(\rho u_i)}{\partial x_i} = 0 \quad (\text{A.5})$$

$$\frac{\partial(\rho u_i)}{\partial t} + \frac{\partial[\rho u_i u_j]}{\partial x_j} + \frac{\partial p}{\partial x_i} - \frac{\partial \tau_{ij}}{\partial x_j} = f_b \quad (\text{A.6})$$

$$u_i = u_\Gamma \quad \text{on } \Gamma_b. \quad (\text{A.7a})$$

The equations above are then solved in the entire domain ($\Omega_b + \Omega_f$). Note that $f_b = (f_m + f_p)$, where f_m and f_p are the forcing functions applied to the momentum and pressure, respectively. This equation is subsequently discretized on a Cartesian grid (MITTAL AND IACCARINO, 2005).

Peskin (PESKIN, 1972) introduced in 1972 the concept of immersed boundary methods. He used this method to compute flow patterns around heart valves and, since then, two main categories of immersed boundary methods have been developed with this approach, elastic and rigid boundaries. Peskin's method for an elastic boundary is a mixed Euler-Lagrangian finite-difference method for computing the flow interaction with a flexible immersed boundary. In this method the Navier-Stoke equations are solved on a stationary Cartesian grid and the IBM is represented by a set of massless elastic fibers whose location are tracked in a Lagrangian fashion by a collection of massless points that move with the local fluid velocity.

$$\frac{\partial \mathbf{X}}{\partial t}(s, t) = \mathbf{u}(\mathbf{X}(s, t)) \quad (\text{A.8})$$

Here, the boundary configuration is described by the curve $\mathbf{X}(s, t)$, where s is a parameter chosen in such a way that a given value of s represents a given physical point of the boundary for all times t . Peskin defines the force density $\mathbf{f}(x, t)$ by a δ -function layer that represents the force applied by the immersed boundary to the fluid. The problem in this definition is that the location of the fibers does not generally coincide with the nodal points of the Cartesian grid. Therefore, the forcing is distributed over a band of cells around each Lagrangian point (see Fig. A.3 (a)), and this distributed force will be used in the momentum equations of the surrounding nodes. By replacing the sharp δ -function with a smooth distribution function, denoted by d , this new forcing function will be more

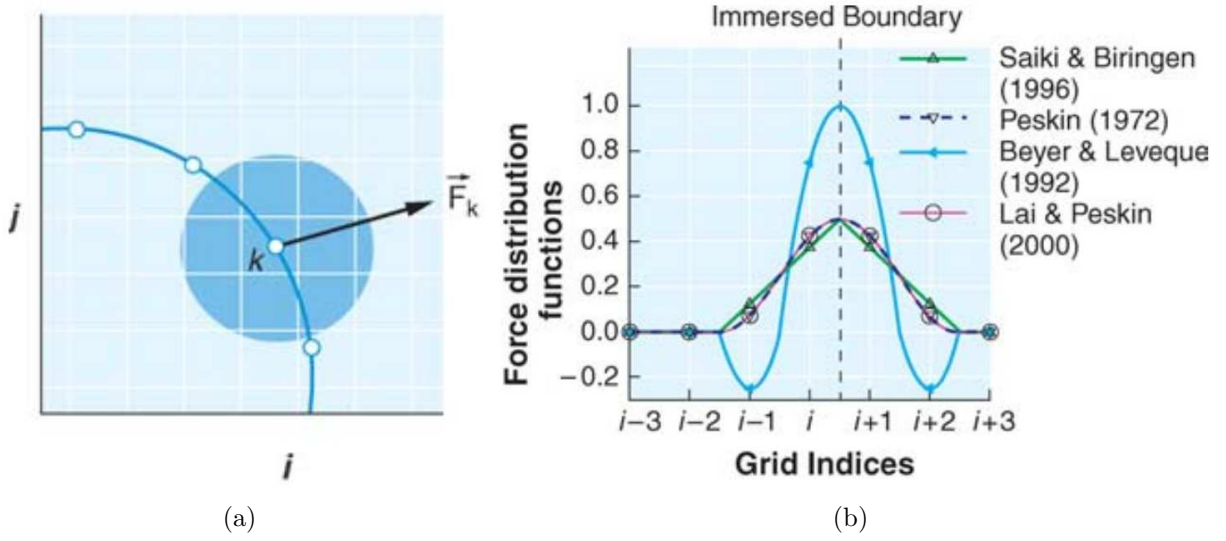


Figure A.3: (a) Transfer of forcing \mathbf{F} from Lagrangian boundary point to surrounding fluid nodes. (b) Distribution functions employed in various studies, (MITTAL AND IACCARINO, 2005).

suitable for use on a discrete mesh. Due to the fibers, the forcing at any grid point \mathbf{x} is then given by

$$\mathbf{f}_b(\mathbf{x}, t) = \int_{\Gamma_b} \mathbf{F}(s, t) \delta(\mathbf{x} - \mathbf{X}(s, t)) ds \quad (\text{A.9})$$

There are more approaches for the distribution function developed over the years and some of them are shown in Fig. A.3 (b). Goldstein developed a virtual boundary approach (GOLDSTEIN *et. al*, 1993). The main idea of the virtual boundary method is to treat the body surface as a boundary embedded in the fluid. This boundary applies a force in the fluid so that the fluid will be at rest on the surface (no-slip condition). Let us denote the boundary Γ_b by $\{\mathbf{X}^e(s) : 0 \leq s \leq L_b\}$. The force $\mathbf{F}(s, t)$ on the boundary is determined by the requirement that the fluid velocity $\mathbf{u}(\mathbf{x}, t)$ should satisfy the no-slip condition on the boundary (MITTAL AND IACCARINO, 2005).

$$\frac{\partial \rho}{\partial t} + \frac{\partial(\rho u_i)}{\partial x_i} = 0 \quad (\text{A.10})$$

$$\frac{\partial(\rho u_i)}{\partial t} + \frac{\partial[\rho u_i u_j]}{\partial x_j} + \frac{\partial p}{\partial x_i} - \frac{\partial \tau_{ij}}{\partial x_j} = \int_{\Gamma_b} \mathbf{F}(s, t) \delta(\mathbf{x} - \mathbf{X}^e(s)) ds \quad (\text{A.11})$$

$$u_i = u_\Gamma \quad \text{on } \Gamma_b \text{ and} \quad (\text{A.12a})$$

$$0 = \mathbf{u}(\mathbf{X}^e(s, t)) = \int_{\Omega} \mathbf{u}(\mathbf{x}, t) \delta(\mathbf{x} - \mathbf{X}^e(s)) d\mathbf{x} \quad (\text{A.13})$$

Since the body force is not known *a priori*, it must be calculated in some feedback way in which the velocity on the boundary is used to determine the desired force. In the virtual

boundary formulation, the force is expressed as

$$\mathbf{F}(s, t) = \alpha \int_{\Omega} \mathbf{u}(s, t) d\tau + \beta \mathbf{u}(s, t) \quad (\text{A.14})$$

where the coefficients α and β are selected to best enforce the boundary condition at the immersed solid boundary. The original intent behind Equation A.14 is to provide a feedback control of the velocity near the surface, but from a physical point of view, it can also represent a damped oscillator. In general, results are promising at low Reynolds numbers but accurately enforcing the boundary conditions require large values of α and β , which can lead to stability problems, especially for highly unsteady turbulent flows (MITTAL AND IACCARINO, 2005).

Discrete Forcing Approach

The Discrete Forcing approach can be formulated to impose the boundary condition on the immersed boundary through indirect means or, it can directly impose the boundary conditions on the IB (MITTAL *et. al.*, 2008). For a simple, analytically integrable, one-dimensional linear model problem, it is possible to formally derive a forcing term that enforces a specific condition on a boundary inside the computational domain. The same is not usually feasible for the Navier-Stokes equations because the equations cannot be integrated analytically to determine the forcing function. Consequently, all the approaches in the previous section employ simplified models of the required forcing. To avoid this issue, Mohd-Yosuf (1997) (J., 1997) and Verzicco *et al.* (2000) (FADLUN *et. al.*, 2000) developed a method that extracts the forcing directly from the numerical solution for which an *a priori* estimate can be determined (SEO AND MITTAL, 2011).

The major advantage of the discrete forcing concept is the absence of user-specified parameters in the forcing and the elimination of the associated stability constraints. However, in the indirect approach, the forcing still extends into the fluid region due to the use of a distribution function and the details of the implementation depend strongly on the numerical algorithm used to discretize the governing equations (SEO AND MITTAL, 2011).

Although the application of IBMs to low and moderate Reynolds number flows has been successful, their extension to higher Reynolds numbers is challenging due to the need to accurately resolve the boundary layers on (immersed) surfaces not aligned with the grid lines. In such cases, the local accuracy of the solution assumes greater importance, and the spreading of the effect of the IB introduced by the smooth force distribution function is less desirable. For this reason, the direct approach can be considered where the immersed

boundary is retained as a sharp interface with no spreading and where greater emphasis is put on the local accuracy near the IB. This can usually be accomplished by modifying the computational stencil near the immersed boundary to directly impose the boundary condition on the IB (SEO AND MITTAL, 2011).

In the direct method, the boundary condition on the IB is enforced through the use of “ghost cells”. In this method, at the pre-processing stage, before integrating the governing equations, all cells whose centroids are located inside the solid body are identified and tagged as “body” cells and the other points outside the body are “fluid” cells. Any body-cell which has at least one fluid-cell neighbor is tagged as a “ghost-cell” (see fig. A.4). Then, a “normal probe” is extended from the ghost point to intersect the immersed boundary (at a body denoted as the “body intercept”). The probe is extended into the fluid to the “image point” such that the body-intercept lies midway between the image and the ghost points. An interpolation is used along the normal probe to compute the value at the ghost-cell based on the boundary-intercept value and the value estimated at the image-point. The value at the image-point itself is computed through an interpolation from the surrounding fluid nodes (a linear interpolation is acceptable for laminar flows, however, for high Reynolds number cases, it could lead to erroneous predictions; for such cases, high-order interpolation should be used). Irrespective of the particular interpolation scheme used, the value of the variable at the ghost-cell node is specified as the negative image-point value. The above procedure can now be solved simultaneously with the discretized Navier-Stokes equations for the fluids nodes.

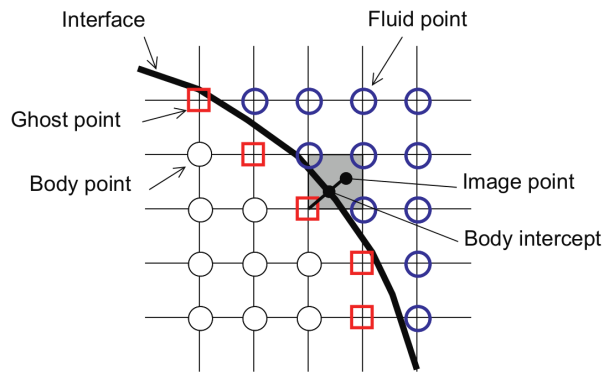


Figure A.4: Schematic of ghost cell method (SEO AND MITTAL, 2011).

A.3.3 The Miranda code

The Miranda code is a radiation hydrodynamics code developed at Lawrence Livermore National Laboratory. It was designed for large-eddy simulations of multi-component flows

with turbulent mixing. Additional physics packages include magneto-hydrodynamics, self-gravity and thermonuclear fusion. The hydrodynamics package solves the fully compressible Navier-Stokes equations in Cartesian coordinates and it is based on a tenth-order compact (spectral-like) scheme in all directions to compute global derivatives, combined with a fourth-order Runge-Kutta time marching method. Details of the Miranda solver and the numerical methods therein, are given by (OLSON, 2012). This numerical tool has been successfully used in numerous studies.

A.4 Methodology

In the present work, since both the continuous and the discrete forcing approaches are implemented in the immersed boundary method, the suitability of these formulations combined with a high-order finite difference method is examined on several acoustic scattering problems and unsteady flows including discontinuities such as shock waves. A suite of two-dimensional numerical simulations of canonical cases are conducted with the aim of analyzing the error behavior associated with the IBM. This analysis will be conducted for simulations including wave reflection, wave diffraction, shock-wave diffraction, and the shock-boundary layer interaction phenomena. The compressible Navier-Stokes equations are solved and numerical results for different flow simulations including several IBM parameters are compared against conventional simulations and analytical results, whenever possible.

A.5 Results

We apply the Immersed Boundary Method to investigate physical mechanisms involved in problems of airfoil noise. These physical mechanisms include wave reflection and diffraction and, for high Mach numbers, may involve the formation of shock waves. In this section, we assess the behavior of the continuous and discrete Immersed Boundary Method coupled to the Miranda code through performing simulations of several canonical cases. The present studies are of paramount importance for the understanding of the current numerical capabilities and they will shed light into the ability to resolve the physics of airfoil noise generation and propagation.

A.5.1 Plane-wave hitting a hard wall

We studied the acoustic wave reflection through a 1-dimensional plane-wave hitting a hard wall (see Fig. A.5 (a)). A cosine plane-wave perturbation (see Eq. A.15 (a) and (b)) is set to travel through the computational domain, hit a hard wall and return; to assess the performance of the IBM, the perturbation pressure is measured at a point along time and compared before and after hitting the wall (see Fig. A.5 (b)). Here, three different pulse wavelengths, λ , are used to parameterize the error. The wavelength λ is computed based on a parameter that measures the number of grid points per wavelength (PPW) and, thereby, the wavelength λ is established as Eq. A.6 (e). A comparison of the continuous and discrete IBM is performed and in the continuous forcing approach the region (thickness) where the forcing term is applied is varied to obtain the error trends.

$$\rho = A \times \mathbf{f}(t) \quad (\text{A.15a})$$

$$\mathbf{f}(t) = \sin(\omega t) \quad (\text{A.15b})$$

$$A = \rho_0 \times 0.001 \quad \rho_0 \text{ is the sea-level air density} \quad (\text{A.15c})$$

$$\omega = \frac{2\pi c_0}{\lambda} \quad c_0 \text{ is the speed of sound} \quad (\text{A.15d})$$

$$\lambda = ppw \times dx \quad (\text{A.15e})$$

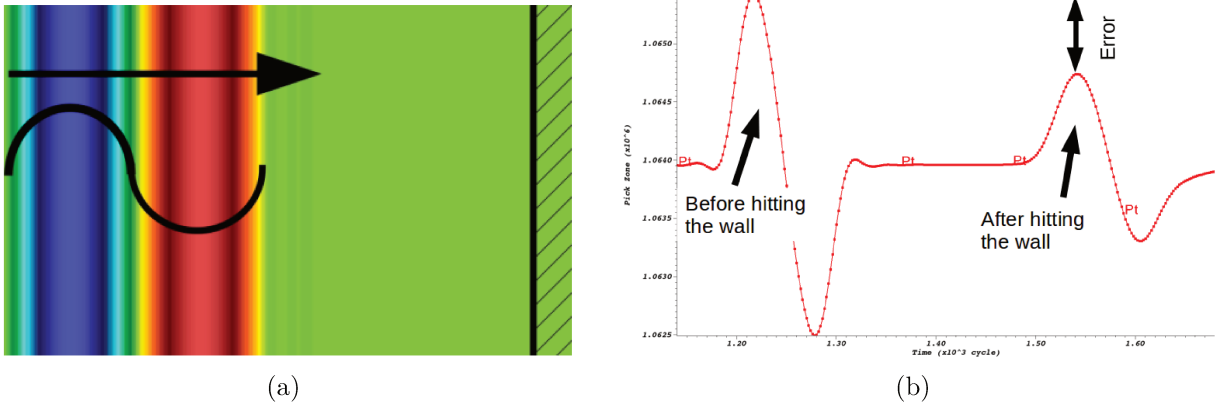


Figure A.5: (a) Schematic representation of the acoustic wave reflection. (b) pressure vs. time plot.

Figure A.6 shows the acoustic wave reflection results for a pulse of wavelength of $\lambda = 0.04\text{cm}$ or 16 points per wavelength, (PPW), in a mesh with $dx=0.0025$. First, as one can observe in the continuous forcing approach IBM results (see Figs. A.6 (a)), the thickness is the length where the forcing function is applied in the fluid region. Thus, as

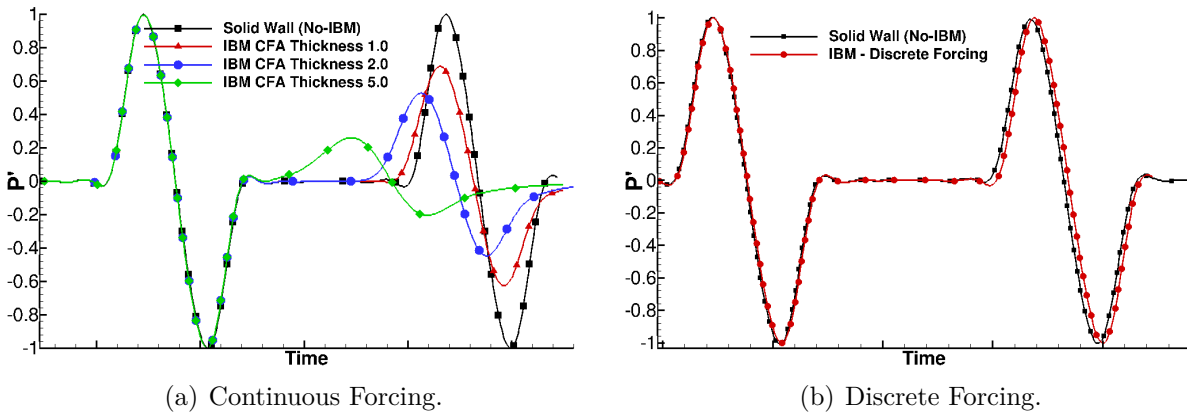


Figure A.6: Acoustic wave reflection results for (a) continuous forcing approach with different thickness (b) discrete forcing approach IBM, for a pulse of PPW=16, $\lambda=0.04\text{cm}$.

the thickness is increased, the difference between the pressure amplitude before and after hitting the hard wall also increases. Figure A.6 (b) shows the discrete forcing approach IBM result and, as it can be seen, the pressure amplitude difference before and after hitting the hard wall is not perceptible (less than 0.01%).

Figure A.7 presents the relative error behavior for acoustic wave reflection results for the 12 cases studied. The relative error is computed taking the difference between the pressure amplitude before and after the wave hit the hard wall, divided by the pressure amplitude of the pulse before hitting the wall. In this figure, two trends can be observed; firstly, as IBM-thickness increases, the relative error also increases, and secondly, as the wavelength is increased, the relative error is reduced. In other words, higher frequencies induce higher relative errors, especially in the continuous forcing approach.

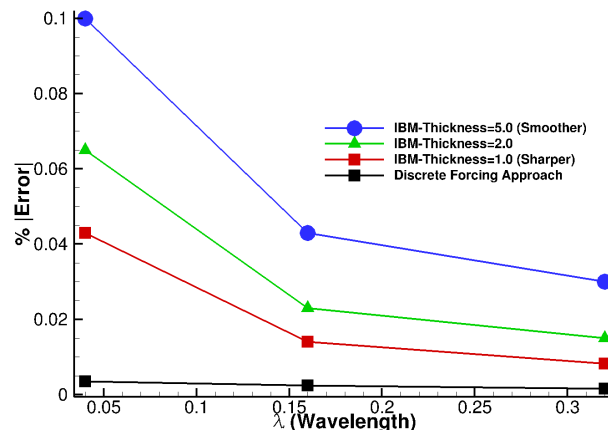


Figure A.7: Relative error behavior for acoustic wave reflection results.

A.5.2 Shock-wave hitting a hard wall (shock-tube)

Since one of the objectives is to perform simulations of flows including shock waves, we study the performance of the two implemented IBM approaches under flow regimes with Mach numbers equal to 1.1, 1.5 and 2.0. Here, shock wave conditions are set as an input (see fig. A.8 (a)). Then, the shock wave is set to travel through the computational domain, hit a hard wall and return. To asses the performance of the IBM, the pressure is measured for a time instant (see fig. A.8 (b)) and compared against results of simulations without the IBM.

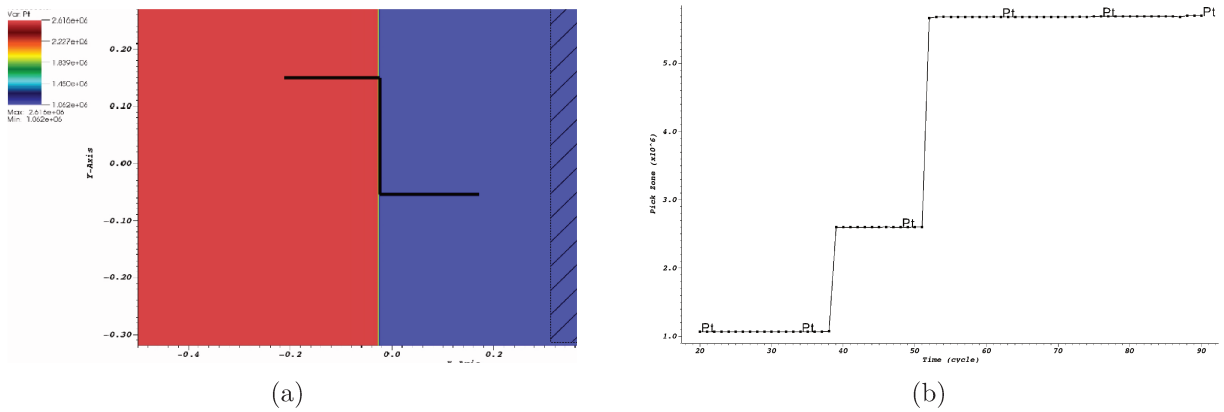


Figure A.8: (a) Schematic representation of 1-D shock wave. (b) pressure vs. time plot.

Figure A.9 shows a comparison between the results for the continuous forcing approach. These results show two different classes of errors. Firstly, the final value of pressure (the pressure after the shock hits the wall and returns) obtained with the continuous forcing approach is lower than the case without the IBM. Furthermore, as the IBM thickness increases, the final value of pressure decreases. Secondly, as one can observe in Fig A.9 (b), instead of having a straight line with a discontinuity (as the black line), one can see a continuous curve in the IBM results showing a time delay to reach the final value of pressure. One can see that as the IBM thickness increases, the delay time also increases.

Figure A.10 shows a comparison of a test case using the discrete forcing approach (blue line) against the case without applying the IBM. With the discrete approach the time delay is not present. Furthermore, the final pressure obtained with the discrete IBM is closer to the case without it, comparing against the continuous IBM. These findings can be seen clearly in Fig. A.11. Figure A.11 (a) shows the relative error of the final pressure obtained using the two types of IBM. The relative error is computed taking the difference between the pressure obtained with the IBM and without it, and dividing by the pressure of the simulation without the IBM. As one can observe in this figure, the error increases as the IBM thickness increases for the continuous IBM and, similarly to

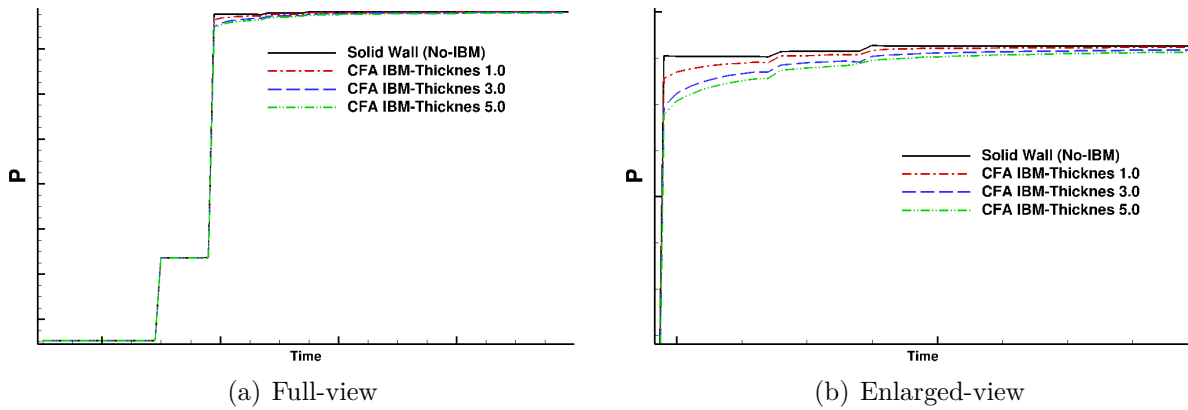


Figure A.9: Shock wave reflection results for Mach number $M_{shock} = 2.0$ using the continuous forcing approach. Each line represents a different case studied: the black and solid-line: hard wall without IBM, Red and dash-dot-line: hard wall with IBM-thickness of 1, blue and long-dash-line: hard wall with IBM-thickness of 3, green and dash-dot-dot-line: hard wall with IBM-thickness of 5.

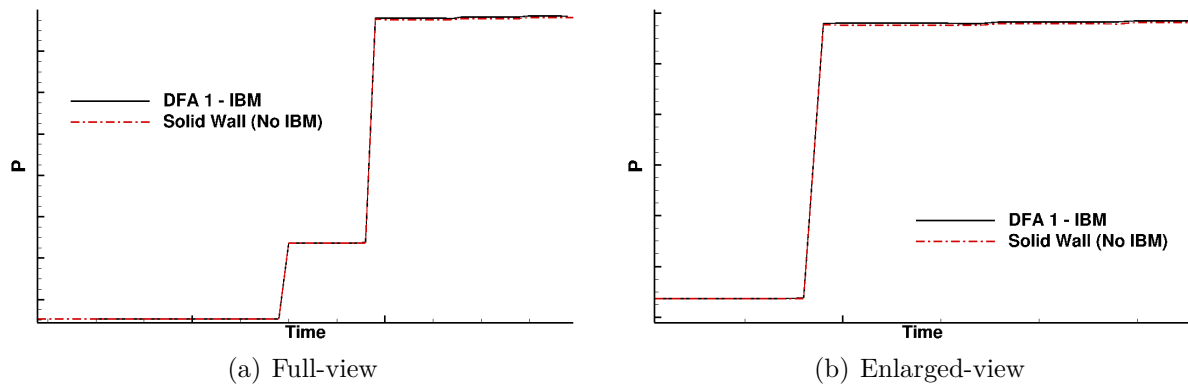


Figure A.10: Shock wave reflection results for Mach number $M_{shock} = 2.0$ using the discrete forcing approach. The black and solid-line represents the case of a hard wall without IBM and the red dash-dot-line represents the case with the discrete IBM.

the previous case, it turns out that the discrete forcing approach has a lower error than the continuous forcing approach. Figure A.11 (b) presents a quantification of the time delay found in the results using the continuous approach. The time delay is defined as the time that the pressure takes to achieve 99% of the final pressure. The figure shows that as the IBM-thickness increases, the time delay also increases and, as the Mach number increases, the time increases as well.

A.5.3 Acoustic Scattering on a Cylinder

A canonical case of acoustic scattering is used to analyze the behavior of the two IBM formulations. This case is important in the context of airfoil noise since acoustic

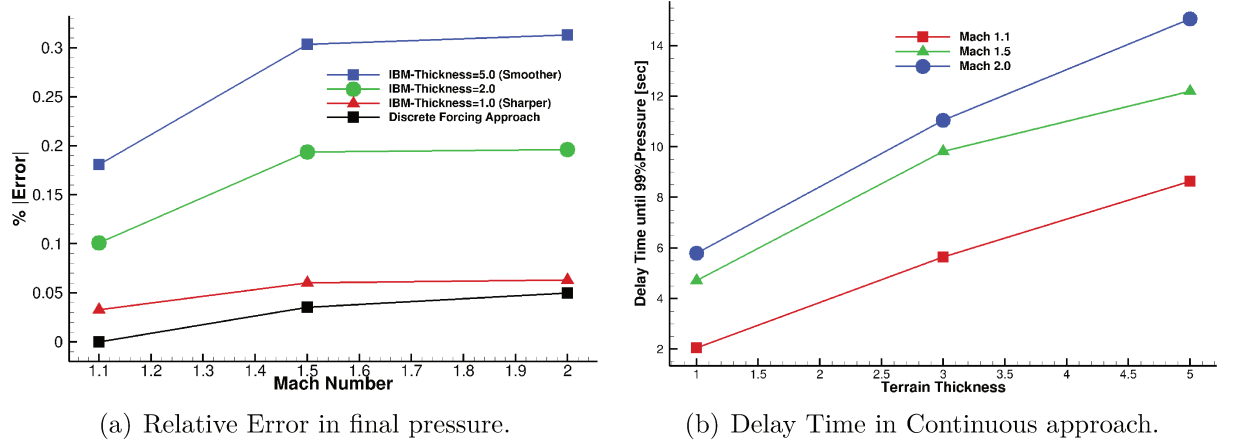


Figure A.11: Error behaviour in shock wave reflection results.

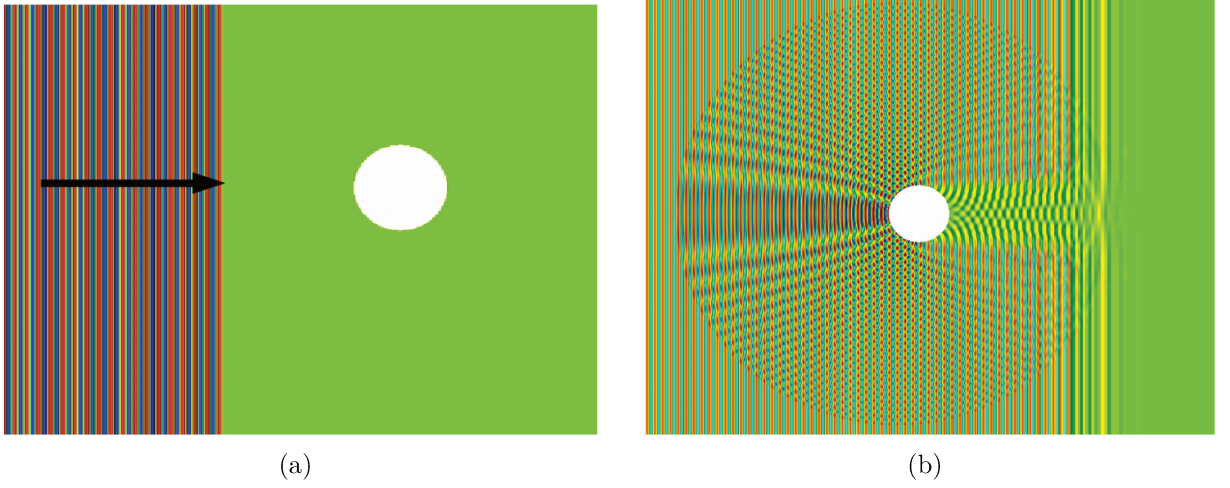


Figure A.12: Schematic representation of acoustic scattering on a cylinder.

waves suffer diffraction along the trailing edge. A continuous planewave with constant amplitude is set to travel and hit a solid cylinder (see fig. A.12 (a) and (b)). In consequence, wave reflection and diffraction phenomena are developed. To quantify the error for this configuration, several cases are performed varying the planewave wavelength and the cylinder radius. Here, five different pulse wavelengths λ are used to parameterize the error. The wavelength λ is computed based on a parameter that measures the number of grid points per wavelength (PPW) and, thereby, the wavelength λ is established as Eq. A.15 (e). Five different radii are used for the cylinder. Taking into account the above, 25 cases are investigated as shown in figure A.13. A non-dimensional parameter is established as R_{cyl}/λ , to which the Helmholtz number is related.

To assess the numerical results, the acoustic pressure is measured at a distance of $2 \times R_{cyl}$ in 360 points at a specific frequency mode, and compared against analytical results. Figure A.14 shows a comparison of numerical results against the analytical solution for different

wavelengths and cylinder radii. Good agreement is observed for higher wavelengths (lower frequencies) and lower values of R_{cyl}/λ as presented in figures A.14 (a), (b). However, it is found that the wave reflection causes the highest error in the numerical results in simulations with low wavelengths (high frequencies) and higher values of R_{cyl}/λ , as one can observe in Figs. A.14 (c) and (d). In these figures, the effect of backscattering in the frontal lobe is underpredicted in magnitude when compared to the analytical results.

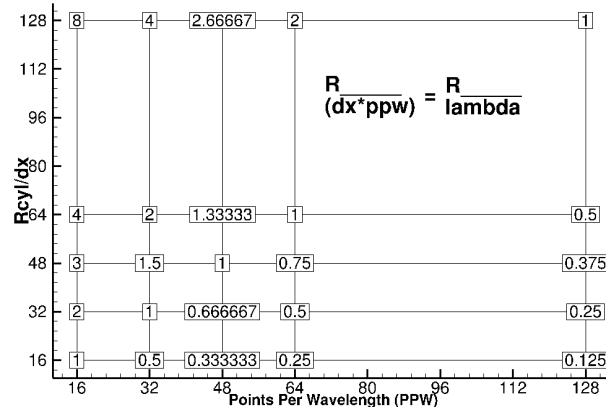


Figure A.13: cases analysed.

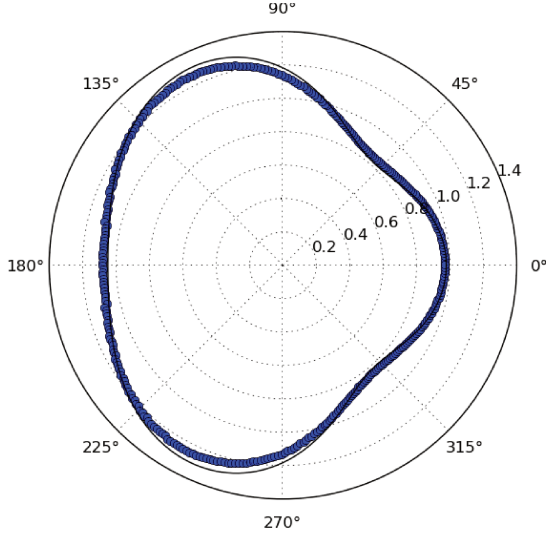
Figure A.15, shows the $L2 - norm$ error behavior of the continuous forcing approach results using an $IBM - thickness = 2.0$. It is found that the $L2 - norm$ (and the $L_\infty - norm$) error is proportional to R_{cyl}/λ . Furthermore, for the same non-dimensional parameter R_{cyl}/λ , the $L2 - norm$ error is inversely proportional to the quantity of points per radius $\frac{R}{\Delta x}$.

- $\frac{R}{\lambda} \sim Error - L2Norm$
- For same $\frac{R}{\lambda} \implies \frac{R}{\Delta x} \sim \frac{1}{Error - L2Norm}$

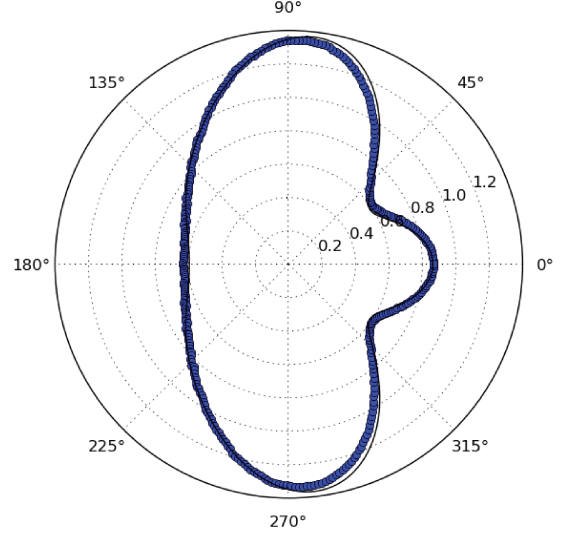
Figure A.16 presents a comparison of results between the continuous approach (using $IBM-thickness = 1.0$ and 2.0), the discrete approach and the analytical solution for a particular case ($R_{cyl} = 0.32, PPW = 32$). It can be observed that, as the $IBM-thickness$ decreases, the numerical results get closer to the analytical solution. However, the discrete approach presents a better performance in terms of the numerical error than the continuous approach.

A.5.4 Transonic Flow

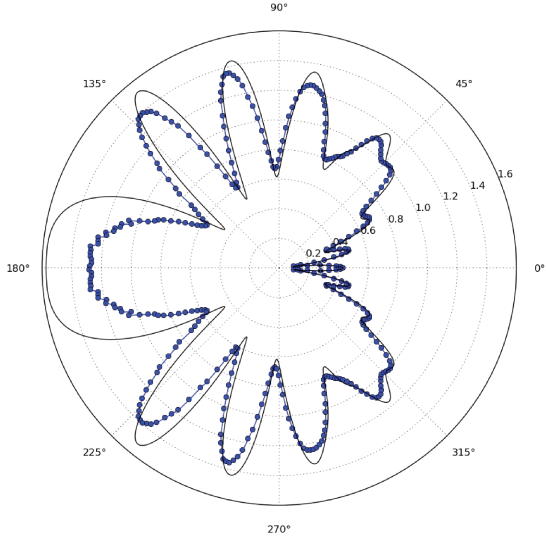
Here, we investigate the performance of the two implemented formulations of the IBM for the solution of more complex problems involving the formation of shock-waves and



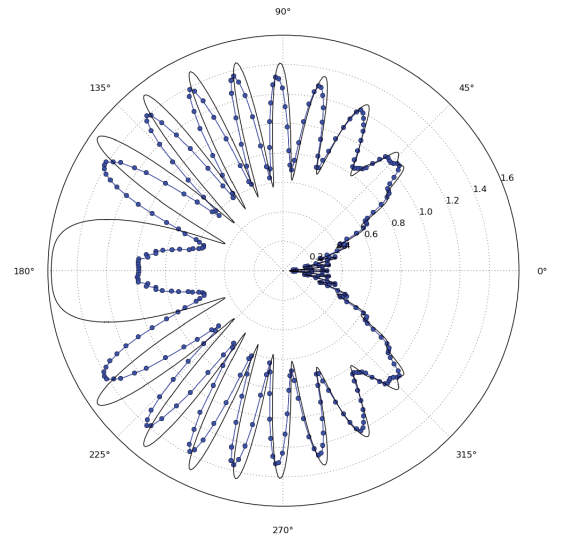
(a) $R_{cyl} = 0.04, PPW = 128, \frac{R_{cyl}}{\lambda} = 0.125$.



(b) $R_{cyl} = 0.08, PPW = 128, \frac{R_{cyl}}{\lambda} = 0.25$.



(c) $R_{cyl} = 0.16, PPW = 32, \frac{R_{cyl}}{\lambda} = 2.0$.



(d) $R_{cyl} = 0.32, PPW = 32, \frac{R_{cyl}}{\lambda} = 4.0$.

Figure A.14: Directivity plot comparison for continuous forcing approach. The black line represents the analytical results and the blue points represent the numerical results.

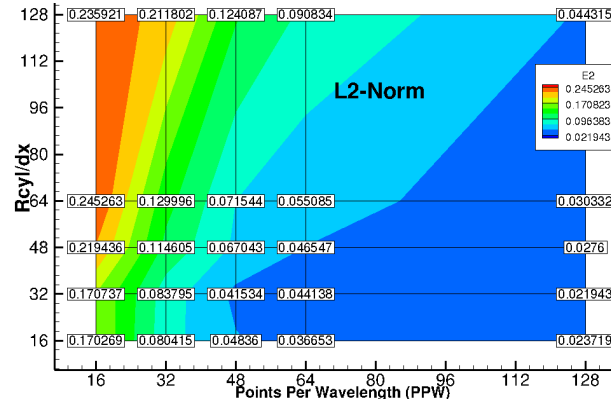


Figure A.15: Error L2Norm contour plot of all cases studied.

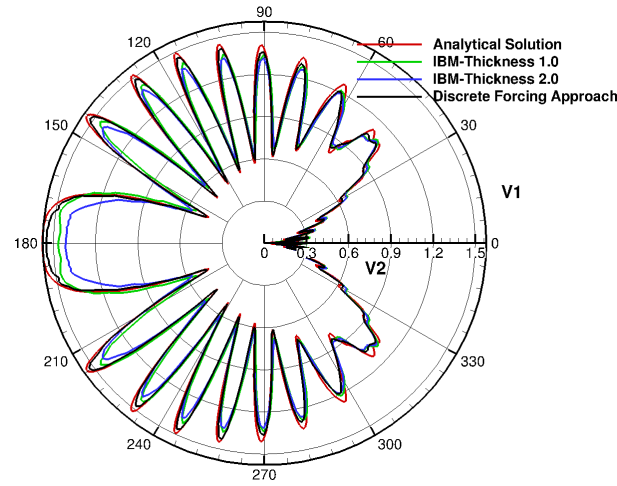


Figure A.16: Comparison of results between the continuous approach (using IBM-thickness = 1.0 and 2.0), the discrete approach and the analytical solution.

their interaction with boundary layers. Transonic flows past different airfoil shapes are shown in Fig. A.17. Here, both a NACA 0012 airfoil and a wedge are simulated. The IBM captures the shock waves and acoustic waves in the downstream region of the flows as well as the vortical structures.

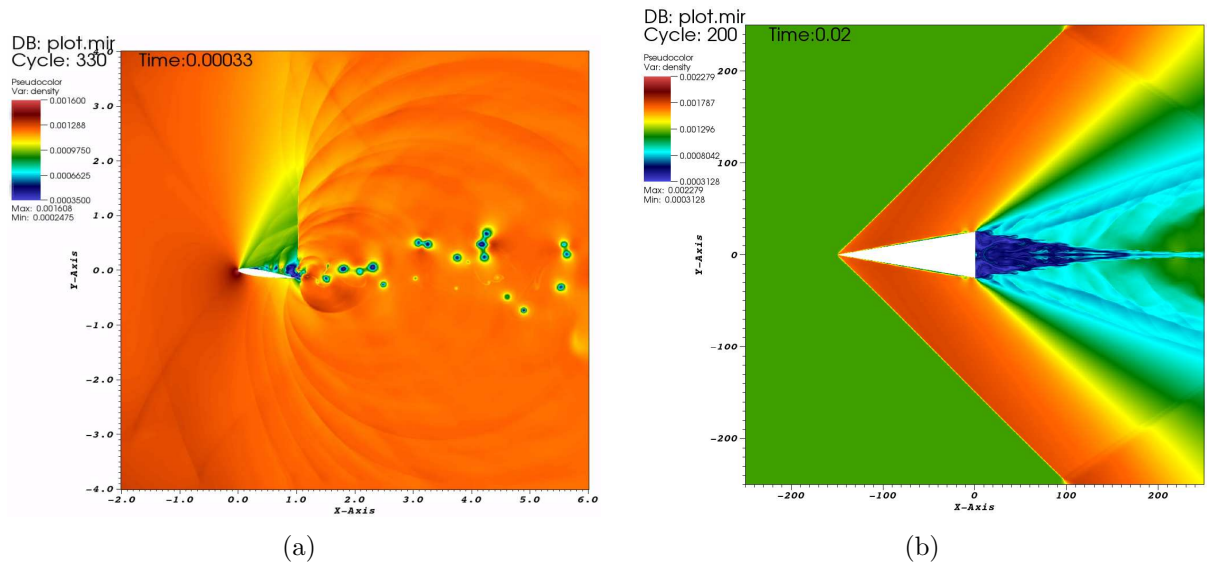


Figure A.17: Transonic flow past different airfoil shapes.